Title
Cavity quantum electrodynamics with tweezer-trapped single atoms

Author
Deist, Emma Grace

Publication Date
2022

Cavity quantum electrodynamics with tweezer-trapped single atoms

by

Emma Grace Deist

A dissertation submitted in partial satisfaction of the

requirements for the degree of

Doctor of Philosophy

in

Physics

in the

Graduate Division

of the

University of California, Berkeley

Committee in charge:

Professor Dan M. Stamper-Kurn, Chair
Professor Ehud Altman
Professor K. Birgitta Whaley

Fall 2022

Cavity quantum electrodynamics with tweezer-trapped single atoms

Abstract

Cavity quantum electrodynamics with tweezer-trapped single atoms

by

Emma Grace Deist

Doctor of Philosophy in Physics

University of California, Berkeley

Professor Dan M. Stamper-Kurn, Chair

The development of quantum technology demands systems of many interacting quantum particles, each individually controlled. Neutral atom arrays are a leading platform in this pursuit, boasting scalable, configurable arrays of single atoms trapped in optical tweezer traps, with demonstrated mechanisms for generating local interactions. Neutral atoms coupled to an optical cavity provide complementary capabilities, enabled by cavity quantum electrodynamics: the control of single atoms with single photons, photon-mediated interactions between distant atoms, and cavity-assisted measurement.

This thesis presents a novel platform for cavity quantum electrodynamics with a neutral atom tweezer array. After motivating and describing the experimental apparatus, I present the details of a quantum sensing result, using single atoms as scanning probes to characterize optical fields of our cavity. I then discuss our study of single-atom cavity state detection, used to demonstrate a mid-circuit measurement within a coherent neutral atom array. The integration of the tweezer array and cavity QED platforms represents a small step toward quantum information processing with neutral atoms.

Contents

List of Figures

List of Tables

Acknowledgments

I have many people to thank for helping me make this dissertation a reality.

My advisor, Dan Stamper-Kurn, supported me from the very beginning of grad school, pushing me to work hard, think deeply, and not shy away from any challenging task. Dan was kind and understanding about my interrupted and unpredictable last couple years in and out of the lab, for which I am very grateful.

I would like to thank Justin Gerber and Johannes Zeiher, with whom I spent many hours in the lab and at the whiteboard. I am grateful for their patience and good attitudes, and for all the learning we did together. I would also like to thank the next generation of experimenters on E6: Leon Lu, Jacqie Ho, Mary Kate Pasha, and Zhenjie Yan. I am grateful for their flexibility and hard work during the brief time we shared, and look forward to seeing what they do next. I also want to thank the other members of E6 over the years—Vicky Xu, Armando Montejano, Shantanu Debnath, Tongyu Zhao, Alec Bohnett, Rachel Tsuchiyama, and Aron Lloyd—for all their contributions and company in the lab.

I am grateful to all the members of the Stamper-Kurn group that I learned so much from: Sydney Schreppler, Claire Thomas, Tom Barter, Jonathan Kohler, Fang Fang, Shun Wu, Zephy Leung, Julian Wolf, Josh Isaacs, Scott Eustice, Kayleigh Cassella, Aaron Smull, Charles Brown, Shao-Wen Chang, and Malte Schwarz. I appreciate their willingness to stop their own work to answer a question or lend a hand.

I owe a great thanks to the mentors I had before my time at UC Berkeley. I am very grateful to Adam Cohen, who taught the first physics lecture I attended as an undergrad and offered me my first research position. And to Jen Hou, who was my grad student mentor in the Cohen lab and a great source of inspiration and encouragement. I am grateful also to John Townsend, whose undergraduate quantum mechanics class first sparked my interest in basic physics research. I would like to thank Philip Walther and his group at the University of Vienna, where I made up my mind about going to grad school for quantum physics. I thank also Melissa Franklin and Jenny Hoffman for their mentorship in college.

I would like to thank all of my friends outside of the lab, who supported me throughout grad school: Amy Phelps, Annie Giebelhaus, Molly Finlayson, Ezra Stoller, Jacqueline Elwood, Sarah Cohen, and all the singers of the San Francisco Choral Artists. And I thank the new community I found at playgrounds of UC Village while our children played, especially Belu Anaya.

I would like to thank my parents and family for all their love and support. Thank you to my grandparents for always asking how my project was going and listening to me ramble on about progress in the lab. Thank you to my aunts and uncles who encouraged me to finish. Thank you to my mom and mother-in-law, and my brother Matthew, for watching my kids and giving me time to write. Finally, I thank my husband Charlie and our kids, for the sacrifices they made to help me finish.

Chapter 1

Introduction

Quantum-enabled technology is an area of intense excitement and research today, in the midst of the apparent “third quantum revolution” [1]. Systems based on well-controlled, interacting quanta—qubits—offer prospects in quantum computation [2, 3], simulation [4, 5], metrology [6, 7], and communication [8], reaching beyond the capabilities of their classical counterparts. These qubits can be realized using superconducting circuits [9, 10], solid-state defects [11], photonic devices [12, 13], trapped ions [14, 15], and trapped neutral atoms [16–18]. Each platform has its own strengths and challenges with respect to controlling and scaling increasingly complex quantum systems [19].

Neutral atoms, guaranteed to be identical by nature, provide a natural fundamental unit for scalable quantum systems, aided by an extensive literature of established laser cooling and trapping techniques [20–22]. Large neutral atom arrays were first realized in optical lattice-based systems [23]. The development of quantum gas microscopy, which adds single-atom detection and control, opened up entirely new regimes of quantum simulation with ultracold atomic systems [24, 25].

Recent years have also brought tremendous progress in the neutral atom tweezer array platform for quantum science [26]. Tightly focused optical tweezer traps guarantee the trapping of one or zero atoms [27] and provide excellent control of atomic internal degrees of freedom [28]. Large defect-free arrays of single atoms can now be prepared in arbitrary geometries by imaging and rearranging probabilistically loaded tweezers [29, 30]. Interactions within a tweezer array are mediated through coupling to high-lying Rydberg states with large dipole-dipole interactions [31]. These interactions can be used to engineer many-body Hamiltonians for quantum simulation [32], realize two-qubit quantum gates [33], and generate large-scale entangled states [34]. The quantum engineering toolbox has been expanded further with the development of tweezer arrays of alkaline earth atoms [35, 36], fermions [37], including ytterbium nuclear-spin qubits [38], and molecules [39], as well as the integration of tweezer and lattice platforms [40].

In tweezer- or lattice-based neutral atom arrays, light provides our primary tool for manipulating the atoms: cooling and trapping, coupling ground and excited atomic states to realize interactions, and detection all rely on atom-light interactions. However, this is all done using coherent laser fields of many photons; rarely do we need to consider the quantum nature of this light. A different version of light-matter interaction can be found in the adjacent field of cavity quantum electrodynamics (QED) [41–44]. Cavity QED considers a strong interaction between a single atom and a single photon, achieved experimentally by picking out a single mode of the electromagnetic field with a resonator, or cavity, where a resonant photon repeatedly encounters the atom and the light-matter interaction is thus enhanced.

When a single photon and single atom interact in a non-negligible way, the system occupies an inherently "quantum mechanical" regime. Here, one observes fundamental quantum mechanical effects: the hybridization of atomic and photonic excitations [45, 46], quantum Rabi oscillations [47, 48], and changes to atomic emission due to the cavity vacuum field [49–51]. Cavity QED also provides a new set of tools for quantum technologies, realizing coupling between atomic and photonic qubits for distributed quantum networks, generating atom-atom entanglement through photon-mediated interactions, and providing tools for measurement [52].

During my PhD work in the Stamper-Kurn group at UC Berkeley, I worked with a team of other researchers on the experiment we call "E6" to design and build a system that combines the neutral atom array and cavity QED platforms for quantum science. In **Chapter 2**, after briefly introducing cavity QED, I discuss dual motivations for this novel system, considering what single atom control can bring to cQED, as well as what cQED can contribute to the now-leading neutral atom quantum information platform. I describe the technical considerations for such a system that led us to design and build a near-concentric optical cavity. This chapter concludes with a summary of the parameters of our first-generation science cavity, constructed and put under vacuum in December 2019, and still in vacuum as I write this in the fall of 2022.

In **Chapter 3**, I describe the rest of the experimental apparatus, focusing mostly on optical systems. **Chapter 4** presents our experimental methods, including alignment techniques that I hope will be useful to future researchers.

Chapters 5 and **6** provide additional information on E6's first two scientific results, published in Refs. [53] and [54]. In the first, we demonstrate superresolution microscopy of cavity fields using the ac Stark shift they effect on single tweezer-trapped atoms, a detour from cQED that arose out of a technique we developed to characterize our cavity. In the second, we demonstrate cavity state detection that is fast, high-fidelity, and local, fulfilling the requirements for mid-circuit measurement in a neutral atom quantum computing platform. I conclude in **Chapter 7** with a brief discussion of the outlook of the work presented in this thesis.

Chapter 2

Motivation: cQED with single-atom control

In this chapter, I will motivate this thesis in the context of the field of cavity QED (cQED) for quantum simulation and computation. After introducing some of the basics of cQED, we will consider the motivation for this apparatus from two vantage points: first, what single atom addressability and control can add to a cQED system; and second, what a cavity can add to a neutral atom tweezer array system. Then I will discuss the technical requirements for a system that combines these two platforms, and how they led us to design and build a near-concentric optical cavity holding a tweezer array.

2.1 Single-atom cQED

2.1.1 Jaynes-Cummings Hamiltonian

A good starting point for thinking about cQED is the Jaynes-Cummings model, which describes a two-level system interacting with a single cavity mode.

$$\mathcal{H}/\hbar = \omega_a \sigma^+ \sigma^- + \omega_c a^\dagger a + g(a\sigma^+ + a^\dagger \sigma^-) \tag{2.1}$$

Here, $\hbar\omega_a$ is the energy between the atomic energy levels $|g\rangle$ and $|e\rangle$, with corresponding raising and lowering operators $\sigma^+ = |e\rangle\langle g|$, $\sigma^- = |g\rangle\langle e|$. $\hbar\omega_c$ is the energy of a cavity photon, described by bosonic creation and annihilation operators $a^\dagger$ and a. g represents the real-valued atom-cavity coupling strength, with terms $a\sigma^+$ and $a^\dagger\sigma^-$ representing the exchange of a cavity excitation for an atomic excitation: the atom absorbing a cavity photon to transition from its ground state to its excited state, and the reverse process. The terms $a\sigma^-$ and $a^\dagger\sigma^+$, corresponding to simultaneous deexcitation and excitation of the atom and cavity, are energy-non-conserving and have already been dropped, according to the rotating wave approximation.

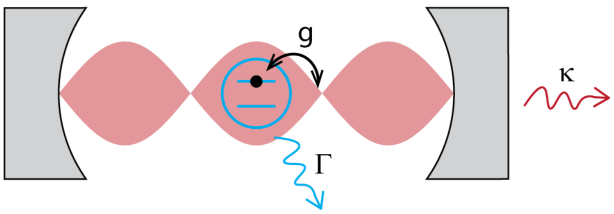

Figure 2.1: Jaynes-Cummings Hamiltonian

In a frame rotating at the atomic frequency ω_a, the Jaynes-Cummings Hamiltonian becomes

$$\mathcal{H}/\hbar = \Delta a^\dagger a + g(a\sigma^+ + a^\dagger\sigma^-) \tag{2.2}$$

where $\Delta = \omega_c - \omega_a$. This Hamiltonian is easily solved in each n-excitation subspace $\left\{|g,n\rangle, |e,n-1\rangle\right\}$. On resonance, the system will exhibit Rabi oscillations between these states at the Rabi frequency $2g\sqrt{n}$. More generally, the system can be thought of in terms of hybrid cavity-atom eigenstates $|\pm\rangle$ at the dressed state energies $E_\pm = \Delta/2 \pm \sqrt{(\Delta/2)^2 + g^2 n}$. The so-called "vacuum Rabi splitting" of the $|g,1\rangle$ cavity excitation into the $|\pm\rangle$ atom-cavity dressed states, separated by $2g$, forms the basis of the cavity transmission measurement described in Chapter 6. Initialization in a superposition state that is not within an n-excitation subspace, such as a coherent state of the cavity field $|g,\alpha\rangle$, will lead to collapse and revival of the atomic Rabi oscillations due to the different coupling to different photon Fock states. These dynamics are different from the simple two-level Rabi oscillations induced by coupling an atom to a coherent laser, hinting at the richness enabled by coupling an atom instead to a quantum light field.

2.1.2 Dissipation

Coherent evolution under the Jaynes-Cummings Hamiltonian is a nice textbook consideration of a two-level atom coupled to a quantum harmonic oscillator, but it is not complete without accounting for the dissipation necessarily present in a real system. The two sources of dissipation we add to our simple model are atomic spontaneous emission, or transitions from $|e\rangle$ to $|g\rangle$ with decay rate Γ, and leakage of photons out of the cavity, associated with the cavity annihilation operator a and the rate κ. These can be included as decay terms in a quantum master equation, or treated with quantum jump operators $\sqrt{\Gamma}\sigma^-$ and $\sqrt{\kappa}a$ in a stochastic wavefunction analysis. While each n-excitation subspace is closed under coherent evolution, the dissipation terms couple each n-excitation state to the (n-1)-excitation manifold, requiring us to consider the full ladder of states down to the zero-excitation state $|g,0\rangle$. Accounting for dissipation is necessary to explain cQED effects such as Purcell-enhanced spontaneous emission, the basis for the cavity fluorescence measurement described in Chapter 6.

The coherent interaction strength g and decay rates Γ and κ are often combined into a single dimensionless cQED figure of merit, the cooperativity, defined as $C = 4g^2/\kappa\Gamma$. $C > 1$ is often referred to as the "strong coupling regime" of cQED.[1] The cooperativity is not the perfect figure of merit for every cQED application: sometimes, absolute timescales matter, not just a unitless comparison between coherent and dissipative rates. The cooperativity as defined here also does not account for cavity leakage as a result of absorptive loss in the mirrors, which is entirely unwanted, versus transmission through the mirrors, which can be detected. A proper accounting of this will in some scenarios call for reducing C by increasing the transmissive contribution to κ, especially for applications involving the detection of cavity photons [52]. I discuss our optimization of C more in Section 2.4.2.

2.1.3 Atom-photon quantum interface

There is a rich body of research on using the Jaynes-Cummings interaction to create a quantum interface between atomic qubits and photons, which can be seen as the fundamental node of a quantum network. Nodes consisting of a single atom strongly coupled to a cavity, realized using Fabry-Pérot and photonic crystal cavities, have been used to demonstrate deterministic state transfer and generate entanglement between atomic and photonic qubits [55–58], and distribute entanglement between atoms trapped in separate cavities [59]. These capabilities can be understood as early realizations of quantum repeaters and quantum memories, with applications in quantum communication and key distribution, as well as atom-photon quantum gates, for distributed quantum computation [52, 60].

2.2 Multi-atom cQED

Going beyond single-atom cQED, one can make use of the Jaynes-Cummings atom-photon interaction to generate atom-atom interactions between atoms trapped in the same cavity, mediated by the exchange of real or virtual cavity photons. This can be done in many different contexts, with applications in quantum simulation, computation, and metrology.

Previous work in the Stamper-Kurn group has demonstrated cavity-mediated interactions between the center-of-mass motion and collective spin degrees of freedom of two atomic ensembles, where the modulations imprinted on the cavity light by one oscillator excite the other [61, 62]. A similar interaction can facilitate spin squeezing in atomic ensembles, leading to the formation of metrologically useful states [63–65]. Spatial variation of the atom-cavity coupling strength $g(r)$, given by the standing wave of a single cavity mode or more complex structure of many degenerate cavity modes, can give rise to spatially patterned interaction energies within an atomic ensemble, leading to self-organization and symmetry-breaking effects [66–69]. These are some of the many exciting results at the interface of cQED and few- and many-body physics [70].

---

[1] Note that this terminology is not perfect; sometimes, as in Ref. [52], the "strong coupling regime" is used to describe the more strict condition $g > \kappa, \Gamma$.

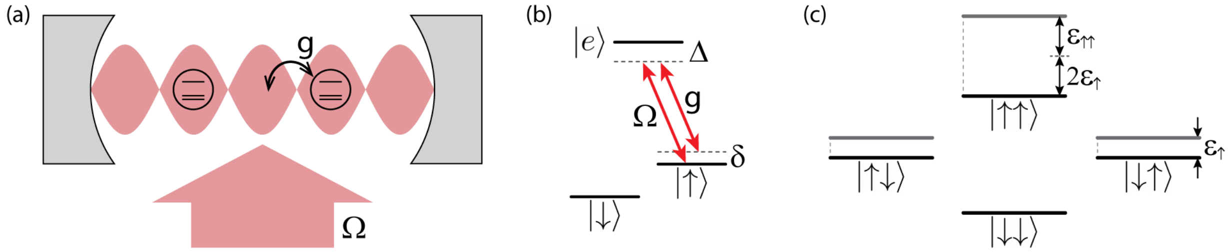

Figure 2.2: Cavity-mediated ZZ-interaction. (a) Two three-level atoms interact with one cavity mode with coupling strength g. Coherent drive illuminates both atoms with strength Ω. (b) Single-atom Λ system level structure. (c) Effective Hamiltonian in two-atom ground manifold subspace: the $|\uparrow\uparrow\rangle$ is shifted by more than twice the $|\uparrow\downarrow\rangle$, $|\downarrow\uparrow\rangle$ shift: this is the ZZ-interaction energy.

To motivate our novel experimental platform bringing together cQED with a tweezer array, a leading platform for neutral atom quantum computing, I will work through a specific example of a cavity-mediated interaction: the realization of an atom-atom ZZ-interaction, which could be used as the basis of a controlled-Z gate and fundamental unit of cavity-based quantum computing platform [71], or adapted more generally for cavity-based Hamiltonian simulation.

2.2.1 Cavity-mediated ZZ-interaction

To realize a cavity-mediated ZZ-interaction, we modify the Jaynes-Cummings Hamiltonian given in Eq. (2.1) in several ways:

1. We consider two atoms, which will be made to interact by the exchange of virtual cavity photons.
2. We consider each atom to be a three-level Λ system, with ground states $|\downarrow\rangle$ and $|\uparrow\rangle$, and excited state $|e\rangle$. We take $|\uparrow\rangle$ to be the cavity-coupled state, replacing $|g\rangle$ in Eq. (2.1).
3. We add a coherent drive term, coupling $|\uparrow\rangle$ and $|e\rangle$ with a standard electric dipole term $\Omega/2\ e^{-i\omega_L t}\,|e\rangle\langle\uparrow| + h.c.$ due to a drive laser with frequency ω_L.
4. We neglect coupling between $|\downarrow\rangle$ and $|e\rangle$ by the cavity and coherent drive. In a real system, this could be achieved with polarization and selection rules, or with a large detuning between $\omega_{L,c}$ and the $|\downarrow\rangle \rightarrow |e\rangle$ transition frequency.

In an appropriate rotating frame, this system, schematically depicted in Fig. 2.2, is described by the single-atom Hamiltonian

$$\mathcal{H}/\hbar = -\Delta\,|e\rangle\langle e| - \delta a^\dagger a + \left(ga\,|e\rangle\langle\uparrow| + \frac{\Omega}{2}\,|e\rangle\langle\uparrow| + h.c.\right) \tag{2.3}$$

where $\Delta = \omega_L - \omega_a$ and $\delta = \omega_L - \omega_c$.

Before we consider a second atom, we adiabatically eliminate the excited state $|e\rangle$ on the grounds that each atom starts in its ground state manifold and Δ is large, resulting in the effective Hamiltonian

$$\begin{aligned}\mathcal{H}/\hbar = & -\delta a^\dagger a + \left(\frac{g^2}{\Delta} a^\dagger a + \frac{|\Omega|^2}{4\Delta}\right) |\uparrow\rangle\langle\uparrow| \\ & + \frac{g}{2\Delta}\left(\Omega a^\dagger + \Omega^* a\right) |\uparrow\rangle\langle\uparrow| \end{aligned} \tag{2.4}$$

Now we consider two atoms with this effective Hamiltonian and take the cavity's initial state to be the vacuum state $|0\rangle$. For δ sufficiently large, we can again perform adiabatic elimination, this time of the states containing a cavity excitation, and obtain the effective two-atom interaction Hamiltonian

$$\mathcal{H}_{\text{int}}/\hbar = \frac{|\Omega|^2 g^2}{\Delta^2\delta} |\uparrow\uparrow\rangle\langle\uparrow\uparrow| + \frac{|\Omega|^2 g^2}{4\Delta^2\delta} |\uparrow\downarrow\rangle\langle\uparrow\downarrow| + \frac{|\Omega|^2 g^2}{4\Delta^2\delta} |\downarrow\uparrow\rangle\langle\downarrow\uparrow| \tag{2.5}$$

Note that I have dropped the single-atom energy shift terms in Eq. (2.5).

This interaction Hamiltonian can be written in the more illuminating form

$$\mathcal{H}_{\text{int}}/\hbar = \frac{|\Omega|^2 g^2}{4\Delta^2\delta}\left(\sigma_Z^{(1)} + \sigma_Z^{(1)} + 2\sigma_Z^{(1)}\sigma_Z^{(2)}\right) \tag{2.6}$$

representing a ZZ-interaction in the $\{|\uparrow\rangle, |\downarrow\rangle\}$ qubit basis between two cavity-coupled atoms.

2.2.2 Gate fidelity and cooperativity

A cavity-mediated ZZ-interaction used as the basis of a quantum gate will have a gate fidelity that is limited by the atomic and cavity decay rates Γ and κ. These sources of dissipation come in through the admixtures of the atomic and cavity excitation states that we adiabatically eliminated in the treatment above, yielding the effective decay rates

$$\Gamma_{\text{eff}} = \frac{|\Omega|^2}{4\Delta^2}\Gamma \tag{2.7}$$

$$\kappa_{\text{eff}} = \frac{|\Omega|^2 g^2}{4\Delta^2\delta^2}\kappa \tag{2.8}$$

These have the expected forms for the decay associated with off-resonant coupling to radiative states via one- and two-photon processes.

Comparing the total effective decay rate with the interaction strength $|\Omega|^2 g^2/2\Delta^2\delta$, we see that there is an optimal two-photon detuning $\delta_{\text{opt}} = g\sqrt{\kappa/\Gamma}$. Here, the ratio between the coherent interaction strength and the effective decay rate is $g/\sqrt{\kappa\Gamma} \propto \sqrt{C}$. The cooperativity, therefore, governs the achievable gate fidelity for a cavity-mediated atom-atom gate. Note that increasing the single-photon detuning Δ does not improve the coherent-to-incoherent rate ratio.

2.2.3 Other cavity-mediated interactions

Here I have described the particular example of a cavity-mediated ZZ-interaction realized between the ground states of two Λ system atoms. This is done using a cavity mode and classical drive field that couple the same $|\uparrow\rangle$ ground state to the excited state $|e\rangle$. Different cavity and drive coupling configurations within the Λ system, controlled using polarization and detuning, generate cavity-mediated interactions with different forms. A "flip-flop" $|\uparrow\downarrow\rangle\langle\downarrow\uparrow|$ interaction is realized with the classical drive coupling $|\downarrow\rangle$ to $|e\rangle$ [72], and a "flop-flop" $|\uparrow\uparrow\rangle\langle\downarrow\downarrow|$ interaction can similarly be realized with a different drive each atom, and cavity coupling between $|e\rangle$ and both ground states. In multilevel atoms, cavity-mediated interactions outside of the two-level qubit framework can give rise to richer dynamics, including spin mixing [72–74].

2.3 Many single-atoms in a cavity

In considering cavity-mediated interactions above, I neglected to mention one of the primary challenges of multi-atom cQED: placing multiple atoms within the same cavity to allow them to interact, while maintaining single-atom control. Indeed, most cQED systems up to this point have done one or the other, realizing global interactions within a bulk atomic gas [70] or demonstrating single-atom cQED effects with one atom [52]; a handful of cQED systems load exactly two atoms [75–79]. The apparatus described in this thesis bridges these regimes with an array of single atoms held in a high-finesse optical cavity, also recently realized in Ref. [80]. Its scientific prospects can be considered from the perspective of what single-atom control can add to a multi-atom cQED system, as well as what a cavity can add to a neutral atom quantum information system.

2.3.1 Programmable interactions: all-to-all becomes any-to-any

Without the ability to address individual atoms, a cavity-mediated interaction such as the one described in Section 2.2.1 is necessarily global, with interaction terms between every pair of atoms in the cavity. This speaks to one of the benefits of cavity-mediated interactions over other leading techniques: cavities naturally facilitate infinite-range interactions, and thus offer exciting prospects for building up entanglement across large systems. On the other hand, all-to-all interactions do not provide the flexibility that we desire in a general quantum information system. The physics of global all-to-all interactions can typically be described using mean-field approximations [81], limiting access to the true quantum many-body regime. The many-body entangled states that can be generated by such interactions are accordingly limited to "fully permutation-symmetric" spin states [82].

To access the full realm of quantum many-body physics with cavity-mediated interactions, local control must be used to tailor the cavity's all-to-all interactions into programmable any-to-any interactions. One method for doing this is to use spatially varying magnetic fields, which can differently shift the relevant energy levels of spatially separated atoms and effectively replace atomic states to the global Δ, δ with individually controlled Δ_i, δ_i in Eq. (2.6). This, coupled with spectral control of a drive field, can enable arbitrary spatially invariant cavity-mediated couplings, as demonstrated in Ref. [83].

Fully general control could be achieved with local drive beams focused onto individual atoms, which would allow one to optically turn on and off any of the possible cavity-mediated interactions between arbitrary atom pairs. Such a platform would enable quantum simulation with arbitrary connectivity, enabling explorations of novel many-body phenomena such as spin glass physics [84] and models of information scrambling in black holes [83, 85], as well as universal quantum computation based on cavity-mediated two-qubit gates.

2.3.2 cQED for neutral atom arrays: measurement opportunities

Above, I argue that a cavity with single-atom addressability could provide the basis for a fully general quantum simulator or computer. However, a fair treatment must consider how such a system would compare with leading quantum information platforms; in reality, such a cavity-based system using current technology would not be competitive. In particular, in Section 2.2.1, we noted that the fidelity of a cavity-mediated quantum gate is determined by the single-atom cooperativity—specifically, by $\sqrt{C}$, making prospects for improvement even more bleak. Typical Fabry-Pérot cQED systems have cooperativities between 1 and 50 [68, 72, 86–89]. Fiber and nanophotonic cavities have achieved higher cooperativities on the order of 100 [90, 91], but the technical prospects for scaling these to a large atom array are more challenging [79, 92]. These types of systems have demonstrated a handful of spin-exchange oscillations effected by cavity-mediated interactions [72] and measurement-based two-atom entanglement with fidelity of around 75% [79, 88]. These are impressive results, but they are very far from what a complete quantum information processor would require.

Rydberg atom tweezer arrays, on the other hand, can generate two-atom entanglement and perform two-qubit gates with infidelities on the order of 1% [33, 93]. They have rapidly outperformed previous records for entanglement generation between two neutral atoms [94, 95] and become the leading neutral atom quantum information platform. Their interactions, mediated by coupling to high-lying Rydberg states, are finite in range, but the drawback of local interactions is largely mitigated by the ease of reconfiguring tweezer-trapped atoms [34]. Achieving comparable performance using cavity-mediated interactions would require cooperativity of around $C \sim 10^4$, which is out of reach for many optical cavity constructions. Thus, rather than aiming for a fully cavity-based quantum information platform, it is worthwhile to consider what a cavity could add to a tweezer array whose gates are performed via Rydberg interactions. Here, I propose that the advantage of the cavity lies in facilitating measurement.

By enhancing the coupling between atomic qubits and a single optical mode, cavities naturally support measurement that is faster and more efficient than free-space imaging. Fast high-fidelity cavity state detection has previously been demonstrated for single-atom cQED systems [79, 89, 96, 97]. In Ref. [54], we demonstrate that our tweezer-cavity system enables the mid-circuit measurement of a single atom without destroying the coherence of the rest of the array. Such a mid-circuit measurement is necessary for the implementation of quantum error correction protocols for quantum computing, communication, and metrology [98–102], and has not been demonstrated in a traditional Rydberg tweezer array, whose state detection at the end of each experimental iteration typically relies on global fluorescence imaging.

Single-atom cavity measurement could also be used for measurement-based quantum computing in a Rydberg tweezer array. Unlike the standard quantum circuits model of quantum computation, which is based on performing entangling gates between initially uncorrelated qubits, measurement-based quantum computing, or one-way quantum computing, begins with a cluster state as its computing resource [103–105]. A cluster state is highly entangled, but requires only pairwise entangling gates between nearest neighbors in a two-dimensional array to comprise a useful substrate for quantum computation. This initial state could be prepared using local Rydberg interactions [34]. The computation then consists of performing single qubit measurements and rotations along the array from one end to the other, with sequential operations conditioned on the results of the previous measurements. In this process, the entanglement in the array is essentially used to teleport quantum gate operations, realizing a quantum circuit. This protocol requires mid-circuit measurements that can be performed, interpreted, and acted upon within the coherence lifetime of the cluster state; fast cavity measurement could provide this missing piece.

Cavity measurement can also be used for measurements beyond single-atom state detection. Collective measurements of multi-atom observables enable heralded entanglement generation [106–109], and cavity "carving" of complex many-body entangled states [110] and atomic Bell states [77]. Under strong nondestructive cavity measurement, quantum Zeno dynamics can effect deterministic entanglement generation [111]. The flexibility provided by cavity measurement may also allow the exploration of many-body measurement-induced phase transitions [112–115].

The work presented in this thesis utilizes a tweezer array in a cavity, but the science we motivate here is not limited to the tweezer array platform. Lattice-based neutral atom arrays, i.e. quantum gas microscopes [25], could also benefit from the capabilities offered by a high-finesse cavity, adding different coherent and dissipative interaction terms to our field's quantum simulation arsenal for more general studies of many-body physics [70, 116, 117]. These are all among the varied scientific prospects we had in mind as we designed our cavity-microscope apparatus.

2.4 System design

Having discussed the scientific prospects of a platform that brings together cQED and a neutral atom array, we consider the technical requirements for such a system. This begins with a discussion of the cQED figure of merit, the single-atom cooperativity, and the Fabry-Pérot cavity geometries, namely near-planar and near-concentric, that enable high cooperativity. Then we consider the compatibility of these cavity configurations with the optical requirements of a tweezer array system. These considerations led us to design and construct a near-concentric optical cavity with the tweezer array formed by light focused through an out-of-vacuum objective. This cavity-objective system comprises the heart of our experimental apparatus.

2.4.1 Defining cooperativity

For the cQED results and prospects that I described above, whether single-atom cQED effect or cavity-mediated atom-atom interaction, the cQED cooperativity, introduced in Section 2.1.2 as $C = 4g^2/\kappa\Gamma$, provides a good figure of merit for the system performance. To inform how to optimize C, we examine its constituent components g, κ, and Γ. This discussion is limited to Fabry-Pérot optical resonators.

Atom-cavity interaction rate g

The coherent part of the cQED interaction, described by the term $a\sigma^+ + a^\dagger\sigma^-$ in the Jaynes-Cummings Hamiltonian (Eq. (2.1)), has strength g. This term is the quantum version of the $\vec{\mathcal{E}}\cdot\vec{d}$ term that describes the classical electric dipole interaction. A complete version of quantizing the electromagnetic field can be found in many textbooks [118, 119]; I just give a quick intuitive overview.

To write down an electric dipole interaction for cQED, we seek the electric field $\vec{\mathcal{E}}$ of a single photon in the cavity mode. We know the energy of each cavity photon, $\hbar\omega$, and can equate it with the integrated energy in the volume of the cavity:

$$\hbar\omega = 2\epsilon_0 V_{\text{mode}} |\vec{\mathcal{E}}|^2 \tag{2.9}$$

For a Gaussian mode, the mode volume V_{mode} is given by

$$V_{\text{mode}} = \frac{\pi}{4} w_0^2 L \tag{2.10}$$

where w_0 and L are the cavity mode waist ($1/e^2$ intensity radius) and length.

Inverting Eq. (2.9) and using Eq. (2.10), we obtain cQED interaction strength due to the electric field of a single photon:

$$\hbar g = -\vec{\mathcal{E}}\cdot\vec{d} = \sqrt{\frac{2\hbar\omega L}{\epsilon_0 \pi w_0^2}}\, d_{eg} \tag{2.11}$$

A large interaction strength g is therefore achieved by concentrating a high energy photon within a small volume. Here I use d_{eg} to denote the dot product of the dipole matrix element $\vec{d}$ with the polarization vector of the cavity photon's electric field; the magnitude of d_{eg} depends on the cavity mode polarization and Clebsch-Gordon coefficient for the specific $|g\rangle \rightarrow |e\rangle$ transition being considered.

Cavity decay rate κ

The rate κ describes the leakage of photons out of the cavity, which can be understood as the inverse of the lifetime of a cavity photon. The time τ it takes a photon to traverse a Fabry-Pérot cavity with length L is given by $\tau = L/c$. The number of reflections a photon will make before leaving the cavity through absorption or transmission is given by $\mathcal{F}/\pi$ [52], defined in terms of the cavity finesse

$$\mathcal{F} = 2\pi/(T_{\text{tot}} + L_{\text{tot}}) \tag{2.12}$$

where T_{tot} and L_{tot} indicate the total transmissivity and loss of the cavity mirrors. The product of these yields the total cavity lifetime $1/\kappa = \tau\mathcal{F}/\pi$ and

$$\kappa = \frac{\pi c}{\mathcal{F} L} \tag{2.13}$$

The cavity decay rate thus depends only on the cavity length L and the quality of the cavity mirrors.

Atomic decay rate Γ

The rate Γ describes spontaneous emission and is fixed for a given atomic transition—in our case, the D_2 transition in ^{87}Rb. ^{87}Rb was selected for its ubiquity in cold atom experiments. Cooling and trapping techniques are well-established, and appropriate lasers are easily available. For the ^{87}Rb D_2 line, $\Gamma = 2\pi \times 6.07$ MHz.

It can also be instructive to inspect the theoretical expression for Γ, which contains a dependence on d_{eg}:

$$\Gamma = \frac{\omega^3 d_{eg}^2}{3\pi\epsilon_0\hbar c^3} \tag{2.14}$$

Cooperativity

Now we put g, κ, and Γ together to look at the direct dependencies of the cavity cooperativity.

$$C = \frac{4g^2}{\kappa\Gamma} = \frac{24c^2}{\pi\omega^2}\frac{\mathcal{F}}{w_0^2} \tag{2.15}$$

Note that the dipole matrix element d_{eg} has dropped out, since it appears in both g and Γ. This is relevant to someone designing a new cavity experiment who might think to increase C by using a narrow-line transition. This can help to increase g/Γ, but not C. For C, the only relevant parameter of the cavity-coupled transition is its frequency ω. Early studies of cQED achieved high cooperativity in part by using microwave transitions with small ω [47, 120–122].

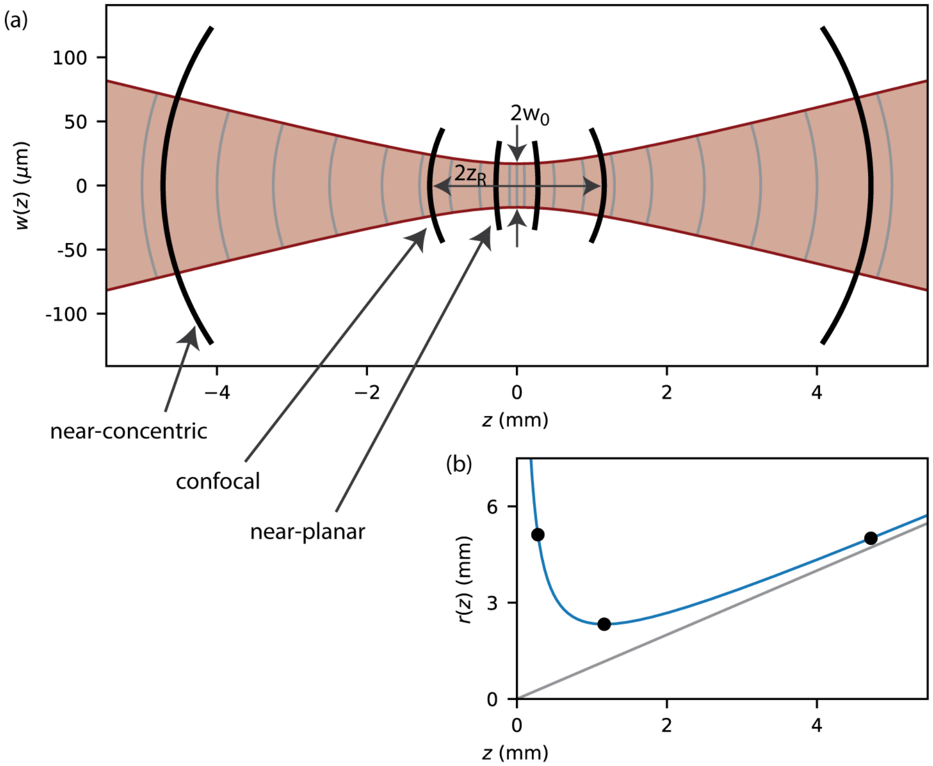

Figure 2.3: Gaussian beam and cavities. (a) Gaussian beam with waist $w(z) = w_0\sqrt{1 + (z/z_R)^2}$. Spherical wavefronts with $r(z)$ given by Eq. 2.16 are shown in gray. Pairs of mirrors whose radii of curvature match the wavefronts' will form cavities that support this spatial mode. Near-planar and near-concentric cavities with the same radius of curvature are shown. A confocal cavity has its mirrors separated by twice the Rayleigh range, where the wavefronts are maximally curved. (b) Wavefront radius of curvature $r(z)$.

The cavity length has also dropped out, since it appears in both in g, via the mode volume, and κ. We are left with an expression for C that just depends on the cavity finesse and the mode waist. These are the parameters that we optimize with our cavity design, as described in the following section.

2.4.2 Designing for cooperativity

Optimizing mode waist

A cavity will support a particular spatial mode if the mirror surfaces "match" the wavefronts of that mode at the mirror locations. The beam can then be thought of as reflecting back onto itself at all locations along the mirror surface, creating a stable cavity mode. The wavefronts of a Gaussian TEM_{00} mode with waist w_0 are given by

$$r(z) = z\left(1 + (z_R/z)^2\right) \tag{2.16}$$

where $z_R = \pi w_0^2/\lambda$ defines the beam's Rayleigh range. Any pair of mirrors matching the wavefronts on either side of the focus will support the same Gaussian mode, as illustrated in Fig. 2.3. Mirror pairs well within the Rayleigh range constitute a near-planar cavity, where the cavity length is much less than the mirror radius of curvature, while those well without form a near-concentric cavity, where the cavity length approaches twice the mirror radius of curvature. A near-confocal cavity is formed when the mirrors match the wavefronts at their most curved point, the edges of the Rayleigh range.

When building an optical cavity, however, we don't start with a tightly focused mode and form mirrors to match the wavefronts; we order mirrors with a certain shape and put them at different distances to form cavities. For a particular radius of curvature R of the mirrors and distance L between them,[2] the cavity waist is given by enforcing $r(L/2) = R$ in Eq. 2.16, which yields

$$w_0 = \left(\frac{\lambda}{2\pi}\right)^{1/2} \left(L(2R - L)\right)^{1/4} \tag{2.17}$$

In this expression, we see that small waists are achieved for small L and small $2R - L$, in the near-planar and near-concentric regimes, with a large waist found in the $L \sim R$ confocal regime. L must be less than $2R$ for a cavity mode to be found.

Decreasing R allows one to form more tightly focused cavity modes at a larger distance ϵ from the planar or concentric conditions. The achievable R is limited by fabrication techniques, and our mirror substrates were made with $R = 5$ mm, the smallest available at the time of fabrication using conventional grinding and superpolishing techniques. Smaller R can be achieved using laser machining [123–126], but decreasing R may also lead to difficulty in applying a highly reflective coating to the strongly curved mirror surface.

Optimizing finesse

High finesse is achieved by using mirrors with very smooth surfaces and coated for high reflectivity. The first determinant of loss is the root-mean-squared surface roughness σ_{RMS} of the mirror substrate, with

$$L_{\mathrm{abs}} = \left(\frac{4\pi\sigma_{\mathrm{RMS}}}{\lambda}\right)^2 \tag{2.18}$$

Our mirror substrates were fabricated and superpolished by Perkins Precision Developments with a measured average surface roughness of 1.14 Å, which according to Eq. (2.18) should yield absorptive losses at the probe wavelength of 780 nm at the few-ppm level.

---

[2] I consider identical mirrors and symmetric mirror placement.

Parameter	Spec'd	Measured
Mirror substrates: Perkins Precision Development		
R_{mirror}	5 mm	-
Mirror diameter	3 mm	-
Mirror length	3.4 mm	-
Surface roughness (RMS)	1.5 Å($<$ 1 Å best effort)	1.14 Å (average of six samples characterized by Perkins)
Mirror coating: Five Nine Optics		
L_{780}	$<$ 10 ppm	$L_{\mathrm{tot}} = 170$ ppm
T_{780} (3 batches)	2 ppm 25 ppm 250 ppm	3.5 ppm (T_{in}) - 250 ppm (T_{out})
L_{1560}	$<$ 2 ppm	$L_{\mathrm{tot}} = 70$ ppm
T_{1560}	100 ppm	-

Table 2.1: Cavity mirror specifications: substrates and coatings. The mirror transmissivities at the probe wavelength of 780 nm were measured as described in Ref. [127] Section 4.6. The absorptive loss per mirror was inferred from cavity ringdown measurements of κ, shown in Ref. [127] Fig. 4.9, through Eqs. (2.13) and (2.12). Transmissivity for the 25 ppm cavity lock wavelength of 1560 nm was not measured because it is not a critical parameter.

Absorptive loss can also occur in the dielectric mirror coatings, but this is typically considered to be negligible. The dielectric mirror coating is designed to achieve some transmission specification T. We ordered three batches of mirror coatings from Five Nine Optics with desired transmissions of 2, 25, and 250 ppm.

Based on these specifications, we hoped to build a cavity with a finesse exceeding $100,000$, using $T = 2,\ 25$ ppm mirrors to construct a one-sided cavity with total losses below 20 ppm. These specifications were met by E6's predecessor experiment, E3, built a decade before [87]. However, in our test cavity setup, we never measured a cavity finesse larger than $17,000$. Independent transmission measurements yielded mirror transmission coefficients within the coating specifications provided by Five Nine Optics, so we attribute the persistently low finesse to anomalous loss, likely due to mirror damage during the coating process.[3] Because of the unexpectedly high loss, we used a more transmissive $T = 250$ ppm mirror as the cavity outcoupling mirror, reducing C for a more desirable ratio of the contributions to κ due to transmission and loss [52, 127].

The specifications of the cavity mirror substrates and coatings are listed in Table 2.1. Note that these include loss and transmission specifications at the cQED probe wavelength of

---

[3] More detail on this saga can be found in Justin's thesis [127]. I advise based on this misfortune to insist on surface characterization by the companies or by you at every step of the mirror fabrication process.

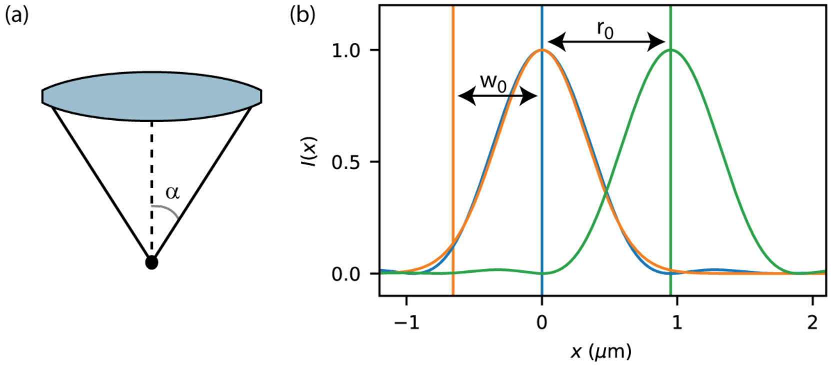

Figure 2.4: NA and resolution. (a) NA is determined by the opening angle α of the imaging lens, per Eq. (2.19). (b) Blue, green: PSF of a NA= 0.5 lens at $\lambda = 780$ nm, separated by the corresponding Rayleigh imaging criterion $r_0 = 950$ nm. This PSF is similar in size to a Gaussian beam with a waist of $w_0 = 660$ nm, shown in yellow; this is approximately the smallest $\lambda = 780$ nm beam waist that can be generated by an objective with this NA.

780 nm and the auxiliary cavity locking wavelength of 1560 nm, discussed more in Chapter 3.

2.4.3 Tweezer array: high NA

The requirements for a system compatible with a tweezer array are less complicated. One simply needs sufficient transverse optical access to form tightly focused traps with a focusing objective positioned at the correct working distance from the atoms. The transverse optical access is quantified by the numerical aperture (NA), defined as

$$\mathrm{NA} = n \sin(\alpha) \tag{2.19}$$

where n is the index of refraction between the object and lens and α is the half opening angle of the imaging lens; see Fig. 2.4. An objective's NA determines the minimum Gaussian waist that can be formed by focusing light through it, as well as the achievable imaging resolution; both are determined by the objective's point spread function (PSF).

The PSF of a diffraction-limited lens is an Airy disk whose first zero defines the Rayleigh resolution r_0:[4]

$$I(r) \propto \left(\frac{2J_1(3.8317\ r/r_0)}{3.8317\ r/r_0} \right)^2 \tag{2.20}$$

The Rayleigh resolution for light at the wavelength λ is determined by the NA as

$$r_0 = 1.22 \frac{\lambda}{2\ \mathrm{NA}} \tag{2.21}$$

---

[4] The scaling factor 3.8317 is the first zero of the first order Bessel function, such that $I(r_0) = 0$.

The Rayleigh criterion is often used to characterize the resolution of an imaging system, stating that two point sources are resolvable when they are separated by at least r_0, as indicated in Fig. 2.4(b). However, single atoms can be discriminated at closer spacings than the Rayleigh criterion with sufficient signal-to-noise and image postprocessing, as has been demonstrated with single-site-resolved imaging in quantum gas microscopes: in Ref. [128], an objective with NA= 0.68, whose Rayleigh criterion is 700 nm, is used to resolve single atoms at a lattice spacing of 532 nm.

For the work in this thesis, we are not imaging lattice-trapped single atoms, pushing the limits of our imaging system as a quantum gas microscope. The more relevant specification of our objective, then, is not the imaging resolution, but the achievable waist of our tweezer traps. This can be determined by approximating the PSF as a Gaussian, as shown in Fig. 2.4(b); the corresponding Gaussian waist ($1/e^2$ beam radius) is roughly

$$w_0 \sim 0.69\ r_0 = 0.42\frac{\lambda}{\mathrm{NA}} \tag{2.22}$$

A tweezer trap waist of around 1 μm or less is required for the collisional blockade to take effect, guaranteeing that the tweezer occupation is zero or one [27]. This has been demonstrated with an objective with NA= 0.5 and tweezer trapping wavelengths of 808 nm and 850 nm [29, 30]; we therefore take NA= 0.5 as the design goal for our first-generation cavity-microscope system, with the potential to upgrade to a higher NA objective if necessary for future work.[5]

Compatibility with a Fabry-Pérot cavity

Achieving transverse imaging with NA> 0.5 in a Fabry-Pérot optical cavity is primarily a technical challenge, rather than a fundamental one. The NA is not fundamentally limited by the divergence of the cavity mode until the cavity mode waist approaches the wavelength λ and the beam divergence becomes huge; we are nowhere near this limit.

Instead, the technical challenge is constructing a cavity whose mirror substrates do not limit the transverse NA, which is frequently the case for near-planar cavities; see, for instance, an image of the near-planar cavity in the Stamper-Kurn group's other cavity experiment, E3, shown in Fig. 2.5(a) [87, 129]. Ref. [80] has recently shown that this technical challenge can be overcome using coned-down conventional mirror substrates, with their realization of a "miniature" near-planar cavity containing an eleven-atom tweezer array. New fabrication techniques, such as laser machining, can create even smaller high-quality mirror substrates, with much smaller radii of curvature [125, 126, 130]. These offer a route toward realizing a tweezer array in a fiber cavity.

Our solution, following the example of Ref. [72], was to opt for a near-concentric cavity geometry using conventionally superpolished ground glass mirrors, where the mirror sub-

---

[5] Per Eq. (2.22), sufficiently tightly focused tweezer traps can in theory be realized with lower NA, but targeting NA= 0.5 allows a bit of breathing room for experimental imperfections such as optical aberration.

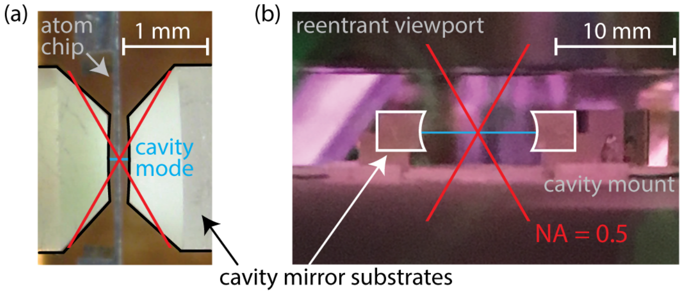

Figure 2.5: Cavity geometries and NA. The figure presents photographs of the in-vacuum cavity setups both in our current experiment (E6) and in the previous generation atoms/cavity experiment (E3). The cavity mirrors in each image are highlighted for clarity; the red lines indicate the opening angle corresponding to NA= 0.5. (a) E3 uses a near-planar cavity, whose substrates limit the transverse NA [87, 129]. The image also shows the side-cut atom chip (gray) that lies between the two cavity mirrors, which, in the specific construction of the E3 experiment, also obscures the optical access transverse to the cavity. (b) Our near-concentric cavity allows sufficient transverse NA for tweezer traps and single-atom fluorescence imaging.

strate size is a non-issue in terms of transverse NA: see Fig. 2.5(b).[6] The only remaining challenge, then, is to design a cavity mounting apparatus and vacuum chamber that permit the placement of the high NA objective at the correct working distance from the center of the cavity mode. We achieve this with a reentrant viewport dropping down toward the in-vacuum cavity and an out-of-vacuum commercially available objective with NA= 0.5, described more in Section 3.2.4. The full cavity mounting apparatus and vacuum chamber are detailed in Justin Gerber's thesis [127].

2.4.4 Science cavity

The first-generation science cavity, placed under vacuum in December 2019, is shown in Fig. 2.6. It was constructed from $T = 2,250$ ppm mirrors fabricated by Perkins Precision Development and coated by Five Nine Optics per the specifications listed in Table 2.1. The science cavity parameters, measured and estimated, are summarized in Table 2.2.

Note that our "near-concentric" cavity is actually 600 μm shorter than the concentric condition for our mirrors. We did not push this limit very hard, as we worried about the alignment stability of a very-near-concentric cavity in our rigid mount design surviving a vacuum bakeout. Other groups have built cavities much closer to concentricity using in-vacuum piezo-actuated mirror mounts [82, 132]. I believe that there is room for improvement

---

[6] A near-concentric cavity has the additional advantage that the atoms are trapped at a larger distance from the mirrors and their mounts and piezos. This could be an important consideration for the integration of Rydberg capabilities, given the large sensitivity of Rydberg states to electric fields.

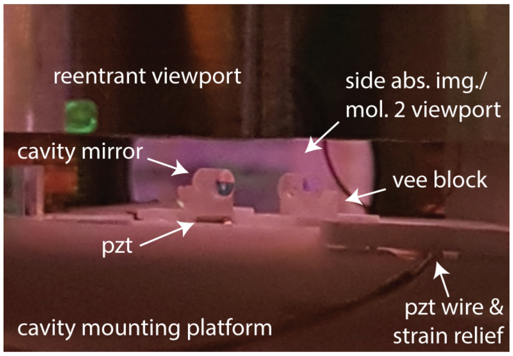

Figure 2.6: First-generation science cavity, pictured in the vacuum chamber at a 45° angle.

Parameter	Value	Obtained from
κ	$2\pi \times 1.06$ MHz	Cavity ringdown measurement (Ref. [127] Fig. 4.9)
L_{cav}	9.4 mm	Transverse mode spacing (ν_{RMS}) to free spectral range (ν_{FSR}) ratio (Ref. [127] Section 4.7.3)
$\mathcal{F}$	15,000	Eq. (2.13)
w_0	20(3) μm	ac Stark shift microscopy/force sensing (Ref. [53]) Eq. (2.17) predicts 17 μm.
g	$2\pi \times 2.7(4)$ MHz	Eq. (2.11) (for stretched state cycling transition)
Γ	$2\pi \times 6.07$ MHz	Ref. [131]
C	4.5(1.3)	Eq. (2.15). The uncertainty in our determination of C is dominated by uncertainty in w_0; w_0 could be measured more precisely using e.g. the cavity scattering rate vs. radial position in fluorescence detection.
L_{tot}	170 ppm	Eq. (2.12), measured $T_{\mathrm{in,out}}$ (Table 2.1)
η_{out}	58%	$\eta_{\mathrm{out}} = T_{\mathrm{out}}/(T_{\mathrm{tot}} + L_{\mathrm{tot}})$
ν_{FSR}	16 GHz	$\nu_{\mathrm{FSR}} = c/2L_{\mathrm{cav}}$
ν_{TMS}	2.4 GHz	Ref. [127] Section 4.7.3

Table 2.2: Science cavity parameters. These values are reported for the probe wavelength of 780 nm and ^{87}Rb D_2 $F = 2 \rightarrow F' = 3$ stretched state cycling transition where applicable.

even with our rigid cavity mount; an upgraded cavity with less lossy mirrors arranged closer to concentric could increase C by a factor of 10 or more.

Chapter 3

Experimental apparatus

In this chapter, I give an overview of our experimental apparatus. The apparatus is held on two optics tables, shown in Fig. 3.1. I begin by describing the systems on the "laser table," where the cooling, repump, and cavity probe and lock lasers generate several beams that are sent by optical fiber to the "science table." Then I describe the systems on the science table, comprising the output beam paths of the laser table fibers as well as the optical transport and tweezer laser systems, which direct light into the vacuum chamber to manipulate the atoms. I devote particular attention to the cavity detection system. Finally, I briefly describe the microwave system that we use for hyperfine state manipulation. Complementary descriptions of many of our experimental systems can be found in Justin Gerber's thesis [127].

Laser	Wavelength	Type	Beams & Frequencies
Cooling	780 nm	DBR	2D MOT: $\nu_{23} - 2\pi \times 8$ MHz 3D MOT: $\nu_{23} - 2\pi \times$ (60-17) MHz molasses: $\nu_{23} - 2\pi \times$ (65-5) MHz abs. img. and BAB: ν_{23} depump: ν_{22}
Repump	780 nm	DFB	2D & 3D MOT, abs. img. and cavity repump: ν_{12}
Cavity probe	780 nm	Toptica ECDL	transmission probe and fluorescence probe: $\nu_{23} + \Delta_{pa}$
Cavity lock	1560 nm	Toptica ECDL	-
Transport	1064 nm	IPG fiber laser	-
Tweezers	808 nm	Thorlabs VHG	-

Table 3.1: Laser specifications for the lab's six lasers. Frequencies relative to the ^{87}Rb D_2 transition frequencies $\nu_{F,F'}$ are given for the 780 nm beams.

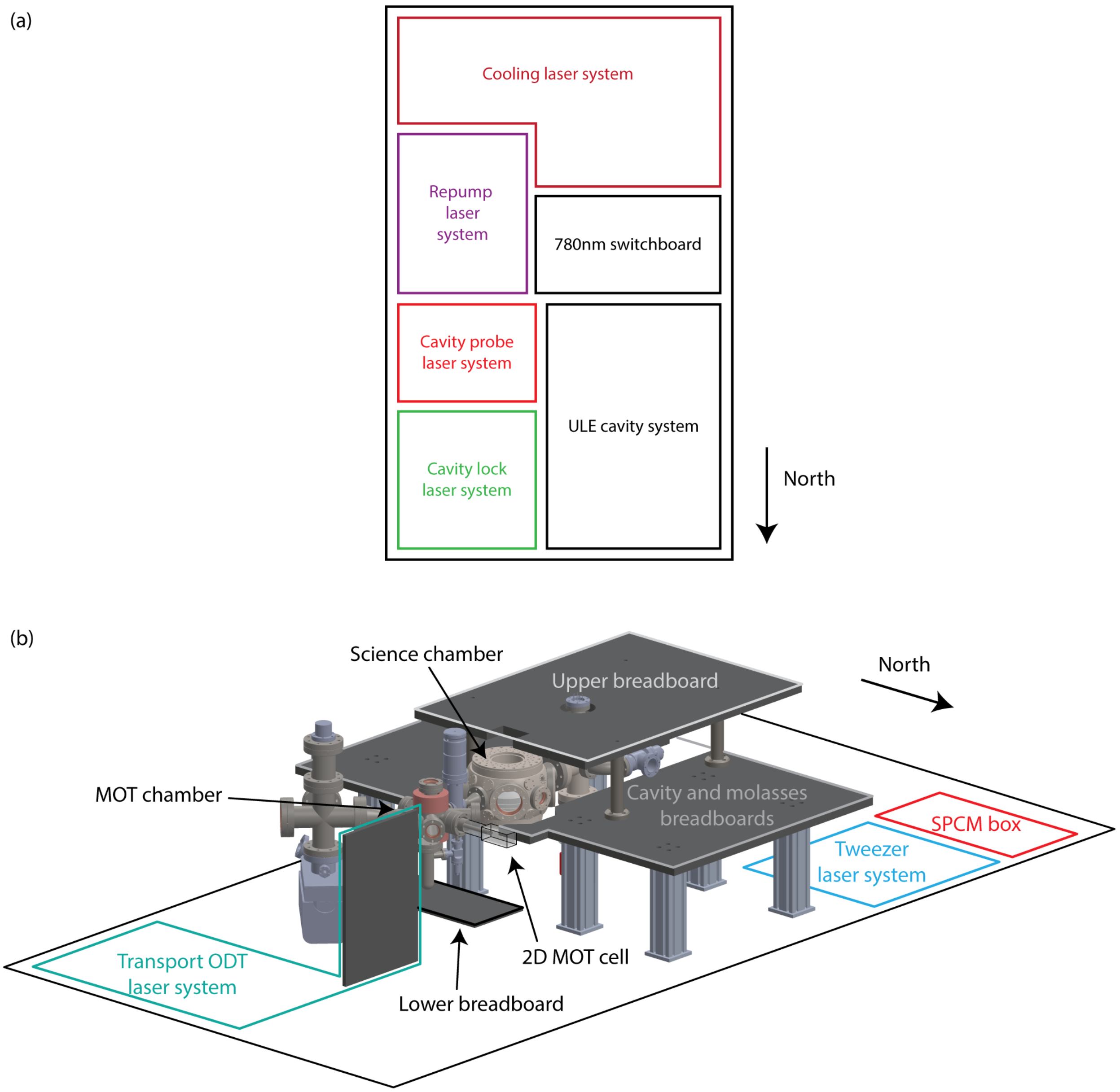

Figure 3.1: Apparatus overview. (a) Laser table. (b) Science table.

3.1 Laser table

3.1.1 Cooling laser system

The cooling laser system, shown in Fig. 3.2(a), generates light near the frequency of the ^{87}Rb D_2 $F = 2 \rightarrow F' = 3$ cycling transition. The laser is a Photodigm distributed Bragg reflector (DBR) laser, referenced to ^{87}Rb through saturated absorption spectroscopy with an atomic vapor cell. Its emission is divided into several different beams, each passing through an acousto-optic modulator (AOM) for frequency and intensity control. The frequency of each beam is given in Table 3.1.

2D MOT and 3D MOT cooling light is amplified by tapered amplifiers (TA) and coupled into 2×4 and 2×6 fiber splitters, where it is combined with repump light and delivered to the MOT "fiber launches," described in Section 3.2.1. Some of the output of the 3D

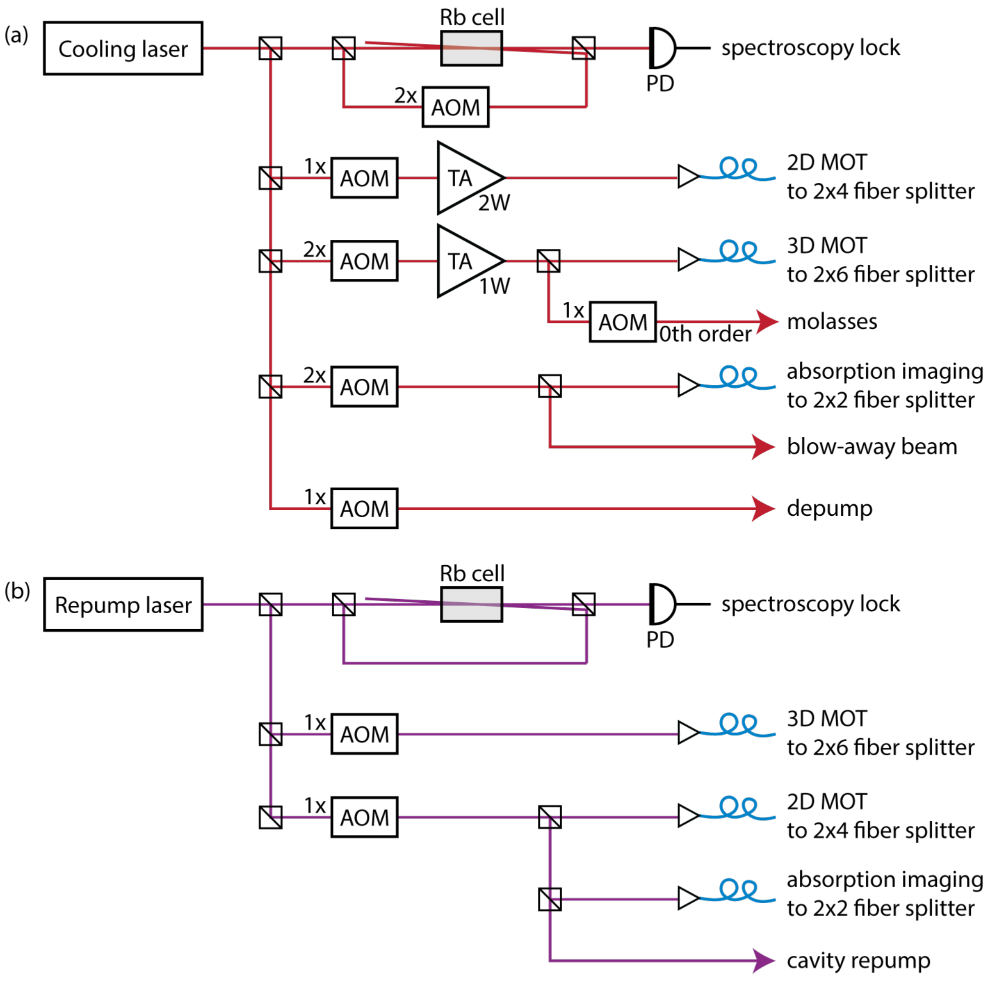

Figure 3.2: Cooling and repump laser systems

MOT TA is picked off and used as "molasses" light for single-atom fluorescence imaging in the tweezer array. The cooling laser also provides resonant $F = 2 \rightarrow F' = 3$ light for absorption imaging, and for our so-called "blow-away beam" (BAB), as well as depump light resonant with the $F = 2 \rightarrow F' = 2$ transition, used for state preparation. The absorption imaging light is coupled into a 2×2 fiber splitter for absorption imaging in the MOT and science chambers. The molasses, blow-away, and depump beams are routed in free space to the 780 nm switchboard described in Section 3.1.5, to be combined with repump and probe light.

3.1.2 Repump laser system

A second, independent locked laser system produces light that drives D_2 transitions out of the $F = 1$ ground state. The basis of this repump laser system, shown in Fig. 3.2(b), is a distributed feedback (DFB) diode laser whose frequency is locked using saturated absorption spectroscopy to the strong crossover peak between the $F = 1 \rightarrow F' = 1$ and $F = 1 \rightarrow F' = 2$ resonances. Resonant $F = 1 \rightarrow F' = 2$ repump light is sent to the 2D and 3D MOT and absorption imaging fiber splitters, and to the 780 nm switchboard for eventual delivery to the science chamber as "cavity repump" for state preparation and detection.

3.1.3 Cavity probe laser system

The cavity probe laser is a Toptica DL Pro external cavity diode laser (ECDL) at a wavelength of 780 nm. It was selected for its narrow linewidth—below 100 kHz and importantly, narrower than the cavity linewidth—and broadly tunable wavelength—by several nanometers. This allows us to operate at a wide range of probe frequencies. In Chapter 5, we operate at a probe detuning of $2\pi \times 400$ GHz below the ^{87}Rb D_2 line, at a wavelength of 781 nm. In Chapter 6, we operate very close to the $F = 2 \rightarrow F' = 3$ cycling transition resonance, at 780 nm.

Light at the probe laser output is picked off and sent through a fiber electro-optic modulator (fEOM) to a reference cavity made of ultra-low expansion (ULE) glass. The ULE cavity, described in detail in Justin's thesis, serves as a stable frequency reference for our cavity probe and cavity lock light, with mirror transmissivity of about 200 ppm for these wavelengths and cavity modes every 1.5 GHz. The probe laser can be tuned to an arbitrary frequency by adjusting the fEOM frequency and locking the upper or lower sideband to a ULE line via a Pound-Drever-Hall (PDH) lock.

The probe light is then divided into two beams that go through double-pass AOMs and are coupled into fibers. These are used in this thesis as the cavity transmission probe and fluorescence probe. The transmission and fluorescence probe AOMs are driven at the same frequency, producing light with the same probe-cavity detuning Δ_{pc}, via a rf phase lock. The transmission probe light is delivered directly to the science table. The fluorescence probe light is carried over a short fiber to the 780 nm switchboard, described in Section 3.1.5, and plugged into the global or local fluorescence probe port depending on the application.

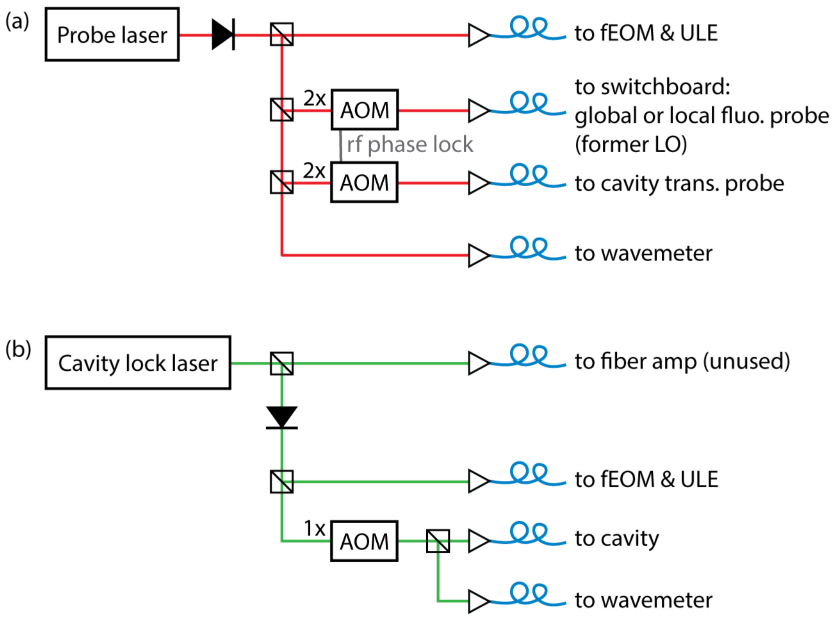

Figure 3.3: Cavity probe and lock laser systems

Note that the fluorescence probe path was previously used to generate a local oscillator (LO) beam at a frequency offset from the cavity probe for heterodyne detection, as described in Justin's thesis [127].

Finally, some light from the cavity probe laser is sent to a wavemeter, which measures the probe frequency with precision at the tens of megahertz level. This allows us to coarsely adjust the probe laser frequency and quickly check that the correct fEOM sideband is locked to the correct ULE mode during normal operation of the experiment.

3.1.4 Cavity lock laser system

The cavity lock laser system is very similar to the cavity probe. The laser is also a narrow-linewidth Toptica DL Pro ECDL, with a broadly tunable wavelength around 1560 nm. This laser generates light that is coupled into the science cavity and used to lock the cavity length. This light was initially intended to be used as a one-dimensional cavity lattice to trap the atoms with identical coupling to the commensurate cavity probe light, following the example of several other ^{87}Rb cQED experiments; see Refs. [72, 133] and Section 5.1. For this reason, Justin calls this the "Cavity ODT." In this thesis, however, cavity light at 1560 nm is never used as trapping light, as atoms are trapped in the tweezer array instead. I thus refer to this 1560 nm laser as the cavity lock laser.

The cavity lock laser outputs about 45 mW. Roughly half of this output power is immediately coupled into a fiber to be used as a seed for a fiber amplifier, intended for a free-space lattice transverse to the cavity axis.[1] The remaining power is used for the cavity lock system.

As with the cavity probe laser, the cavity lock laser frequency is stabilized by locking a fEOM-generated sideband to the ULE cavity. The fEOM frequency is tuned to find a simultaneous science cavity resonance with the cavity lock light and the desired cavity probe frequency. A single-pass AOM provides downstream intensity and frequency control of the science cavity lock light, which is also monitored on the wavemeter.

3.1.5 780 nm light switchboard

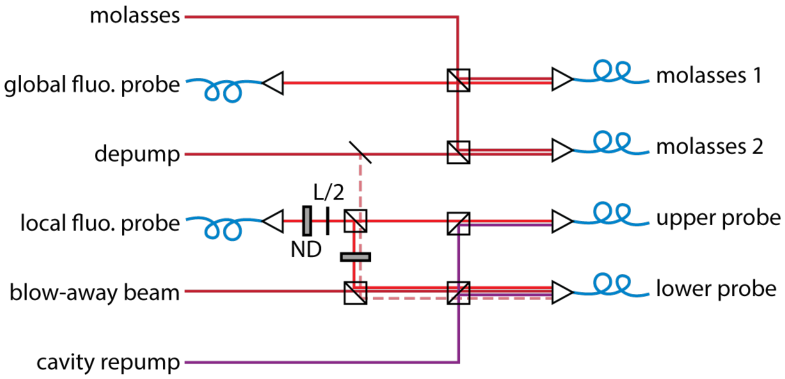

Figure 3.4: 780 nm light switchboard combines light from cooling, repump, and probe lasers to send to the science chamber. Neutral-density filters (ND) and a power-balancing half-wave plate ($L/2$) are used to balance the upper and lower local fluorescence probe beams, which require very low power.

As described above, some of the cooling, repump, and cavity probe light is coupled from the independent laser systems into fiber splitters and fibers for direct delivery to the 2D and 3D MOT fiber launches, and absorption imaging and cavity transmission probe paths. The rest is routed to the 780 nm switchboard region of the laser table to be combined in different configurable pairings for delivery through shared fibers to the science chamber, as depicted in Fig. 3.4.

The “molasses 1” path can contain molasses imaging light derived from the cooling laser and global fluorescence probe light from the cavity probe laser. The “molasses 2” path was initially set up as a second molasses imaging path but later reconfigured to provide depump light for state preparation. The “upper probe” fiber provides local fluorescence probe and repump light for local cavity detection. The “lower probe” fiber has been used for optical pumping to the $F = 2$ stretched states with appropriately polarized depump and repump light, as a blow-away beam for loss-based state detection and optical alignment,

---

[1] The fiber amplifier (Precilasers Single Frequency Fiber Amplifier) has been tested, but the free-space lattice has not yet been built.

and finally as the second local fluorescence probe beam.[2] The upper and lower fluorescence probe paths require low power and careful power balancing for the local cavity fluorescence measurement demonstrated in Ref. [54]. This is achieved using neutral density (ND) filters for coarse adjustment and a half-wave plate ($L/2$) and polarizing beam-splitter (PBS) for fine adjustment; see also Section 6.3.4. The depump-to-lower-probe path (dashed line) was dismantled in the process of building the local fluorescence probe paths, but was used in the stretched state preparation described in Section 4.5.2.

3.2 Science table

Now we turn to the science table, home to two more lasers—the optical transport laser and the optical tweezer laser—and the vacuum chamber, where all the beams overlap in three key locations: the 2D MOT cell, the 3D MOT chamber, and the science chamber. An overview is shown in Fig. 3.5, and each path is discussed in more detail below. The cavity paths are especially important, so they are given their own section: Section 3.3.

3.2.1 2D and 3D MOT fiber launches

The 2D and 3D MOT cooling and repump light is delivered to the science table using 2×4 and 2×6 fiber splitters. Each fiber output provides an independent 2D or 3D MOT beam that is sent directly into the 2D MOT cell or 3D MOT chamber via a “fiber launch,” shown in Fig. 3.6. Each fiber launch sends its collimated fiber output through a $L/2$ and PBS, used for polarization cleanup and power balancing, and a quarter-wave plate ($L/4$), to set the appropriate circular polarization to effect a MOT. Then the beam is telescoped to a large size to create a large trapping volume. The 2D MOT fiber launches feature separate cylindrical telescopes for collimation along the x and y axes, creating elliptical beams with waists $w_{x,y} \sim 20,\ 60$ mm that roughly fill the 2D MOT cell. The 3D MOT telescopes create circular beams with a waist of approximately 14 mm. Finally, some of the paths contain gold mirrors to direct the beams into the chamber while preserving (but flipping the handedness of!) their circular polarization.

The 2D MOT fiber launches are mounted to the optics table on large vertical posts, and the 3D MOT fiber launches, constructed using the Thorlabs cage-mount system, are mounted directly to the MOT chamber viewports. This design sacrifices alignment knobs for the sake of saving space: note that the up/down 3D MOT fiber launches don’t have any mirrors at all! This can make alignment of the 3D MOT tricky, but it is workable. Early in the lifetime of the experiment, we made the decision to not retroreflect the 2D or 3D MOT beams. This has worked well enough, but the 2D MOT in particular is quite power-hungry: each beam uses over 60 mW of cooling power. Retroreflecting the 2D MOT beams using a

---

[2] This fiber was originally used for vertical absorption imaging in the science chamber and is thus labeled “image_single” in the lab and “science vertical imaging” in Justin Gerber’s thesis [127].

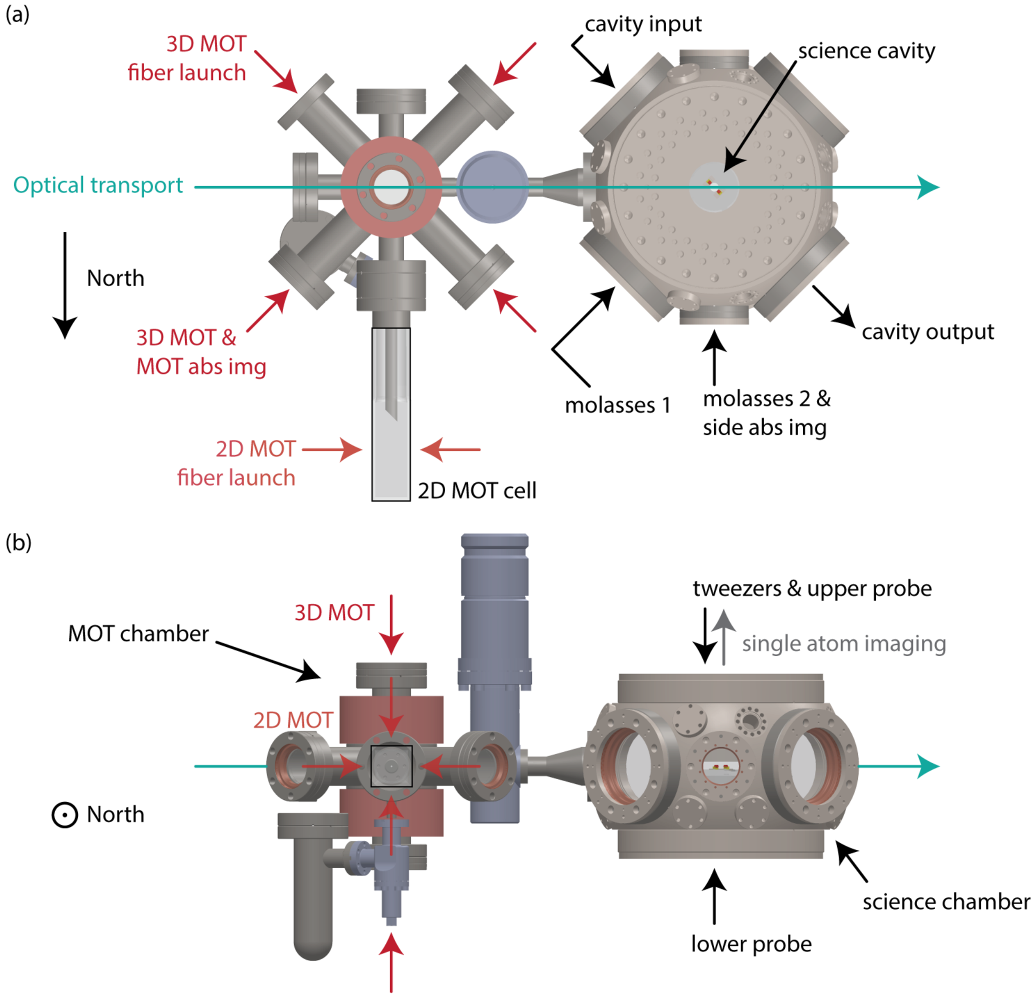

Figure 3.5: Vacuum chamber and beam paths. (a) Top view. (b) Front view.

gold hollow roof prism mirror would immediately reduce the power requirement by half, but would require swapping out the 2D MOT 2 × 4 fiber splitter.[3]

The northeast-southwest 3D MOT beam axis is shared with the MOT absorption imaging system, as shown in Fig. 3.6(b). The absorption imaging 2 × 2 fiber splitter output is coupled into the MOT beam path through the unused port of the polarization cleanup PBS, and coupled out in the same way on the other side of the chamber. The imaging path shares the 3D MOT beam collimation lenses; a final $f = 100$ mm lens images the MOT onto a CCD camera (FLIR Grasshopper USB3 GS3-U3-15S5M-C) with a measured imaging magnification of 0.36. This imaging system is used to optimize the 3D MOT and loading of the transport optical dipole trap.

---

[3] This points out a downside of the fiber splitters, which are otherwise quite convenient: they do not offer any flexibility.

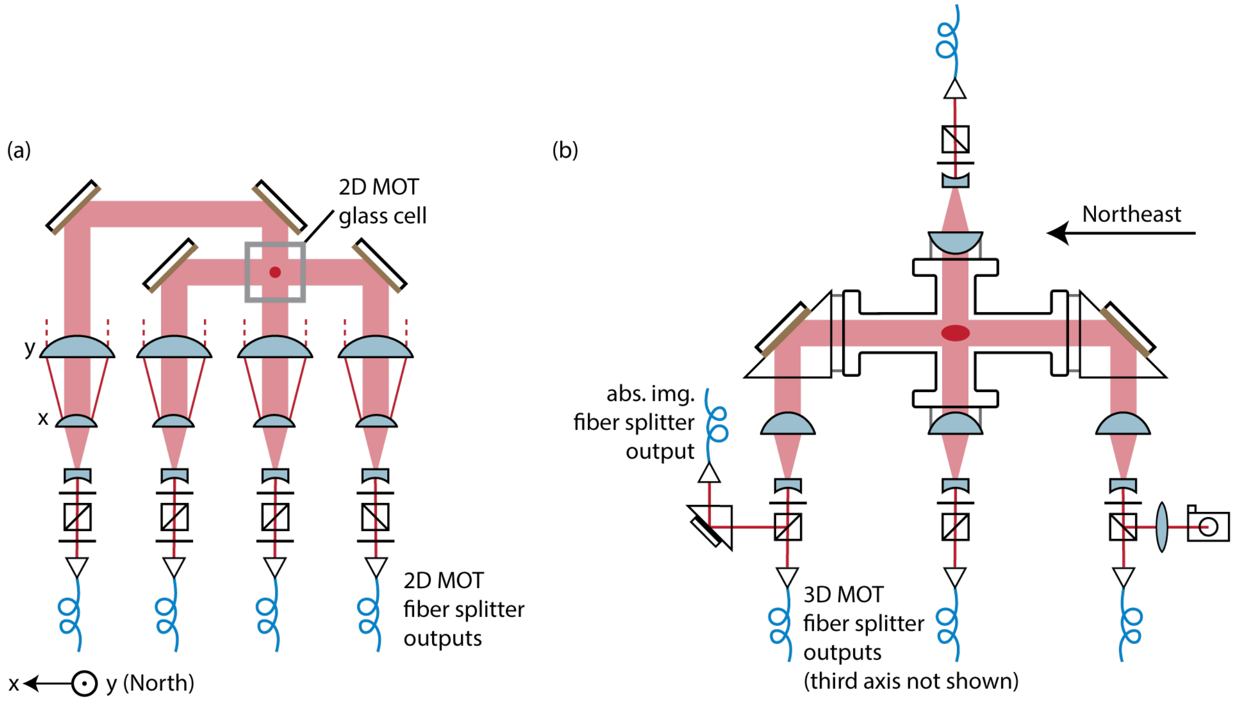

Figure 3.6: MOT fiber launches. (a) 2D MOT. (b) 3D MOT.

3.2.2 Optical transport system

The optical transport laser is a 20 Watt fiber laser from IPG Photonics (YLR-20-1064-LP) at a wavelength of 1064 nm. The laser specifications indicate that it is a “broadband” laser with a bandwidth of 0.3 nm, but it is more properly understood as a multi-frequency laser, almost a frequency comb, within that bandwidth.[4] This laser is used to generate a far-off-resonant optical dipole trap that traps atoms out of the MOT and transports them to the science cavity and tweezer array. The transport is realized using a tunable-focus lens (TFL).

The transport laser system is shown in Fig. 3.7. As this is a high-power laser system, the figure indicates all the beam dumps (BD) used to deflect power for safe laser alignment. The fiber output mode shape and even pointing change with output power due to thermal effects, so after coarse alignment has been done using the built-in low-power visible red laser pointer, proper alignment should be done with the laser outputting its maximum power (20 W), but with most of the power dumped at the first PBS. This is done using the first half-wave plate at the laser output, oriented at a slight angle toward a beam dump to prevent back-reflection into the laser.

---

[4] This is relevant as pairs of tones can drive stimulated Raman transitions out of the $F = 2$ manifold, causing atomic heating and loss; for this reason, the atoms are depumped into the $F = 1$ hyperfine ground state prior to optical transport.

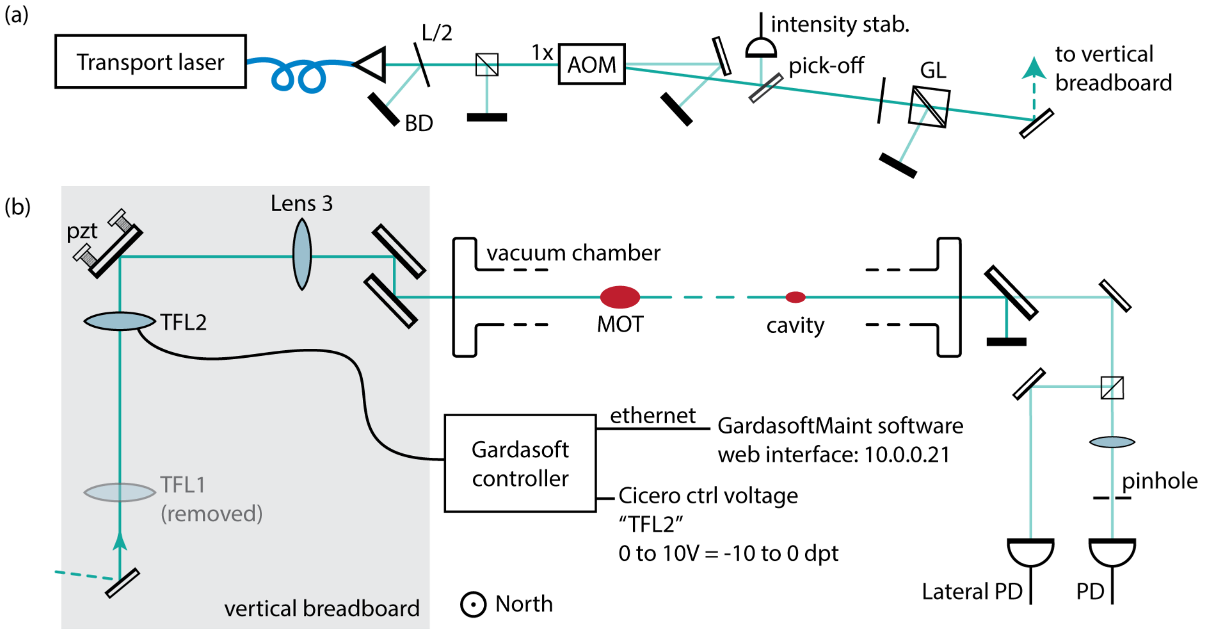

Figure 3.7: Optical transport laser system. (a) Fiber laser output. (b) Vertical breadboard and propagation through the vacuum chamber.

The collimated fiber laser output has a large waist of 1.8 mm, chosen to require minimal beam shaping before the tunable lens focusing system and to minimize thermal lensing effects. However, such a large beam requires special care to be taken to avoid clipping, which can lead to dramatic aberrations at the beam focus. The beam goes through a single-pass water-cooled AOM driven at a fixed frequency using a direct digital synthesizer (DDS) and voltage variable attenuator for intensity control. Following the AOM is a pickoff to a photodiode for intensity stabilization and a high-power Glan-Laser (GL) polarizer. The beam is then deflected to a vertical breadboard, which holds the tunable focus lens system used to transport the atoms.

The tunable focus lens (TFL) system, shown in Fig. 3.7(b), follows the method described in Ref. [134]. Two elastic lenses whose focus can be tuned with an applied current (Optotune EL-C-16-40-TC), labeled TFL1 and TFL2, are mounted upstream of a fixed lens, labeled Lens 3, with focal length $f_3 = 250$ mm. The only critical distance in the setup is the spacing between TFL2 and Lens 3, which should equal the focal length of Lens 3. This ensures that adjusting TFL2 changes the focal position of the final beam without changing the beam waist, thus keeping the dipole trap parameters fixed during transport. This can be seen from the ray transfer matrix analysis of the beam going through TFL2 and Lens 3, with propagation distance f_3 in between:

$$\begin{bmatrix} x_f \\ \theta_f \end{bmatrix} = \begin{bmatrix} 1 & 0 \\ -1/f_3 & 1 \end{bmatrix} \begin{bmatrix} 1 & f_3 \\ 0 & 1 \end{bmatrix} \begin{bmatrix} 1 & 0 \\ -1/f_2 & 1 \end{bmatrix} \begin{bmatrix} x_i \\ \theta_i \end{bmatrix} = \begin{bmatrix} x_i(1 - f_3/f_2) + f_3\theta_i \\ -x_i/f_3 \end{bmatrix} \tag{3.1}$$

Importantly, θ_f, which determines the beam waist of the focused dipole trap, depends only on f_3 and the size of the beam at TFL2, x_i. The final focal position can be found by applying another free space propagation matrix and solving for $x = 0$, which result will depend on the setting of f_2.

An additional TFL placed upstream of TFL2 and Lens 3 provides the ability to tune the beam waist as well, by changing x_i in Eq. (3.1). One can imagine using this capability to optimize for the ideal fixed beam waist for trapping and transporting atoms out of the MOT, or to construct a more sophisticated trapping sequence that begins with a large trap, mode-matching the MOT, and then compresses the trap to provide tight confinement during transport. Such dynamic control of the trapping potential is also explored also in Ref. [134]. We experimented with this during the initial setup of the TFL system, but the practical difficulties of working with the TFLs undermined the imagined benefits of this approach. Our challenges with aberrations, thermal drift, and repeatability problems led us to remove TFL1. The remaining TFL is still labeled TFL2.

TFL2 is mounted horizontally, per the recommendation of the manufacturer: when mounted vertically, gravity causes distortion of the elastic lens, which is composed of an optical liquid held in a polymer membrane, resulting in beam aberrations. TFL2's focusing power can be tuned from −10 to 10 diopters (or focal length from −100 mm to 100 mm, through infinity). We use a current controller provided by Gardasoft (TR-CL180), which can be configured through a web interface to accept an analog control voltage. TFL2 was configured to restrict its tuning range to −10 to 0 diopters, never operating as a focusing lens, to prevent the high-power transport beam from being accidentally focused onto an optical element or the vacuum chamber input viewport.

Optical transport occurs by adjusting TFL2 from roughly −1.1 dpt, where the beam is focused at the MOT, to roughly −5.6 dpt, where the beam is focused at the cavity, using an S-shaped curve. These values, especially the cavity position, must be adjusted regularly, as they are highly sensitive to thermal changes. The thermal sensitivity, according to an Optotune engineer, can be understood in terms of two counteracting effects: the optical fluid expands with temperature, and its refractive index decreases, with the former effect dominating. Since the transport laser operates at a high power of about 6 W, the lens is heated locally during normal operation, and in a way that varies throughout the experimental cycle. The cavity diopter setting may thus require adjustment according to changes in laser power, experimental cycle time, and ambient temperature in the lab. The MOT diopter setting is far less sensitive, given the large size of the MOT and the shorter distance to the MOT chamber.

To facilitate frequent readjustment of the cavity diopter setting, a focal position monitoring system was constructed at the chamber output, using a small amount of laser power transmitting through a backside-polished mirror that deflects most of the transport power to a beam dump. The beam is sent through a focusing lens and pinhole to a photodiode, which provides a measurement of the beam size at the pinhole as the focal position is varied. This can be used to quickly adjust the cavity diopter setting when setting up an experimental run. A 2D lateral effect position sensor (Thorlabs PDP90A) was also installed to monitor

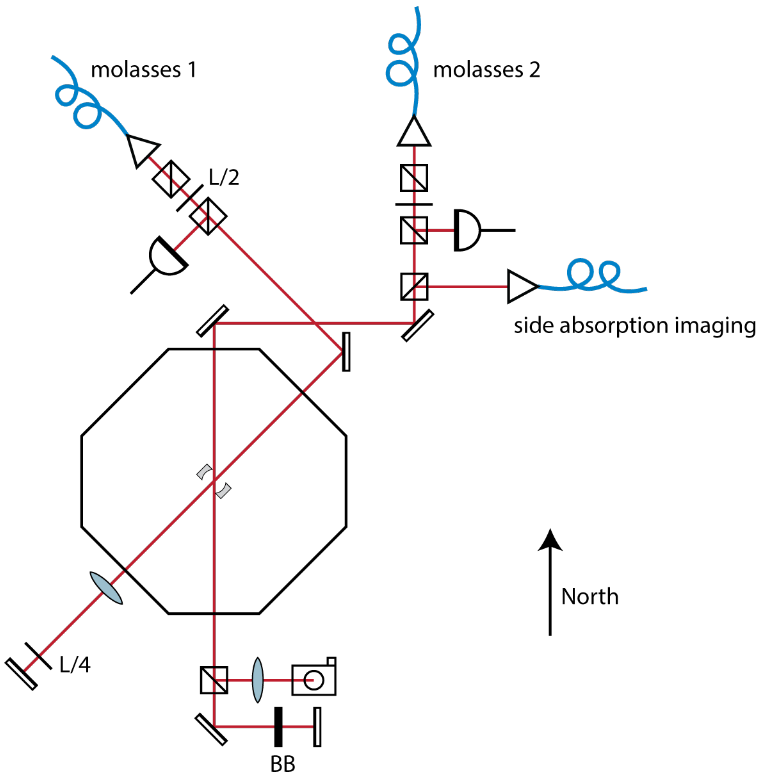

Figure 3.8: Molasses and side absorption imaging paths. Optional beam block (BB) can be removed for molasses 2 retroreflection (not used in this thesis).

the transverse alignment of the transport ODT to the center of the cavity. A piezo-actuated mirror before Lens 3 helps with the sensitive alignment demanded by the long propagation distance to the cavity.

The transport beam waist is about 45 μm at the MOT and about 50 μm at the cavity, with the larger waist at the cavity likely due primarily to aberration of the focus. Deviation from the ideal f_3 separation between TFL2 and Lens 3 may also play a role. The transport distance is about 32 cm down the east-west axis of the vacuum chamber.

3.2.3 Molasses 1, molasses 2, and side absorption imaging

Now we move to the beams around the science chamber. Breadboards mounted to have a beam height at the center of the cavity hold the cavity probe and lock optics, which are described in Section 3.3, and the imaging molasses and side absorption imaging paths, which I describe here. These systems are shown in Fig. 3.8.

Molasses 1

The "molasses 1" path enters the science chamber through the northeast viewport, propagating perpendicularly to the cavity. It is also at a slight vertical angle, starting on 3-inch optics pedestals before the chamber and ending on 1-inch pedestals on the other side. This is to provide some cooling along the vertical axis during single-atom fluorescence imaging in the optical tweezers.

The molasses 1 beam is collimated with an aspheric lens (Thorlabs C240TMD-B, $f = 8$ mm) to a beam waist ($1/e^2$ intensity radius) of roughly 800 μm. It passes through two PBS cubes, for polarization cleanup and power pickoff for intensity stabilization, and a $L/4$ to give it circular polarization. Then it is sent into the science chamber with a silver mirror.

On the other side of the chamber, the molasses 1 light is retroreflected with a $L/4$ to realize a $\sigma^+ - \sigma^-$ molasses configuration. The retroreflection path also includes an achromatic lens (Newport PAC21AR.16, $f = 150$ mm), selected for future retroreflection of a lattice at 1560 nm planned to share this axis.

The molasses 1 path is used for single-atom fluorescence imaging, using molasses light derived from the cooling laser, and early studies of cavity fluorescence detection, described in Section 6.3, using fluorescence probe light derived from the probe laser. Since this light illuminates the entire tweezer array, I refer to it as "global fluorescence probe" light, in contrast to the "local fluorescence probe" light that illuminates a single atom in the center of the cavity for local measurement 6.3.4.

Molasses 2 and side absorption imaging

The "molasses 2" and side absorption imaging paths enter the science chamber through the north viewport, perpendicular to the optical transport axis.

The absorption imaging optics are all mounted using Thorlabs cage system, attached directly to the north and south viewports using custom threaded "bolt washers" that we installed on every viewport of the science chamber.[5] Using the cage-mount system allowed us to bring these beam paths up above the other optics crowded around the science chamber. The molasses 2 optics start on the breadboard and are coupled into the cage-mount imaging path with periscopes and a PBS.

The side absorption imaging fiber output is the second port of the 2 × 2 absorption imaging fiber splitter, which contains resonant absorption imaging and repump light. Its first port goes to the MOT absorption imaging path described in Section 3.2.1. The fiber output collimator (Thorlabs F810APC-780) creates a beam with a large waist of 3.75 mm, chosen to cover the entire science cavity in its field of view. The beam passes through a PBS, used to couple in the molasses 2 light, and a $L/2$ before going through the chamber.[6]

---

[5] These are described and pictured in Justin's thesis [127], Section 5.8.

[6] In Justin's thesis, he describes circularly polarized absorption imaging light along this "science side imaging" path. This was changed to provide linearly polarized depumping light in the molasses 2 path for optical pumping to $|F = 2, m_F = 0\rangle$, described in Section 4.5.2.

On the other side of the chamber, molasses 2 and side imaging are separated on another PBS. The imaging path continues with a $f = 75$ mm lens that images the center of the vacuum chamber onto a CCD camera (FLIR Grasshopper USB3 GS3-U3-15S5M-C) with a magnification of 0.77. This imaging system is very helpful for aligning the optical transport beam with the cavity, tweezer array, and molasses 1 and 2 beams.

The molasses 2 path was built to match the molasses 1 path, with the same collimating lens and beam waist of 800 μm. It was intended to be used as a second σ^+-σ^- retroreflected molasses path for fluorescence imaging. However, we found experimentally that molasses 2 was not necessary for single-atom imaging.[7] For the work in this thesis, the molasses 2 path was used instead to send in vertically polarized depump light, π–polarized with respect to a vertical applied magnetic field, for optical pumping to the $|F = 2, m_F = 0\rangle$ state, for which the retroreflection path was blocked.

3.2.4 Upper breadboard: high-resolution systems

All of the high-resolution optics systems lie on the breadboard above the science chamber. This includes the tweezer array and single-atom fluorescence imaging systems described in Justin's thesis, and a new tightly focused "upper probe" path containing fluorescence probe and repump light for local cavity measurement. The upper breadboard systems are shown in Fig. 3.9(a). All of them share the high-resolution objective directed into the chamber through the upper bucket window, shown in Fig. 3.9(b).

High NA objective

The heart of the high-resolution optics systems is the objective (Mitutoyo G Plan Apo 50x Objective). The objective has a numerical aperture NA = 0.5, effective focal length $f = 4$ mm, and working distance of roughly 15 mm, which includes compensation for imaging through glass thickness of 3.5 mm.[8] The objective and viewport were characterized before the science chamber was constructed, with a measured PSF characterized by a Rayleigh criterion of 1050 nm at the imaging wavelength of 780 nm [127]. The theoretical Rayleigh criterion of a NA = 0.5 diffraction-limited system is 950 nm.

The objective is mounted on a custom machined part that attaches directly to the upper reentrant viewport of the science vacuum chamber, shown in Fig. 3.10. The mount was designed to achieve maximum passive stability between the objective and the science cavity, while still providing the necessary degrees of freedom to align the objective: x,y, and z piezo-actuated translation stages, as well as a mirror mount for tip/tilt control. The objective drops down into the bucket window, held by lens tubes, and is positioned a few millimeters above

---

[7] We expected single-atom imaging to require molasses k-vector components along all three spatial axes to achieve three-dimensional cooling; Ref. [135] also observed that this was not necessary for imaging in a quantum gas microscope.

[8] This lens is thus called "Glass Thickness-Compensated," intended for applications such as inspecting LCDs and flat-screen televisions, as well as imaging into vacuum chambers.

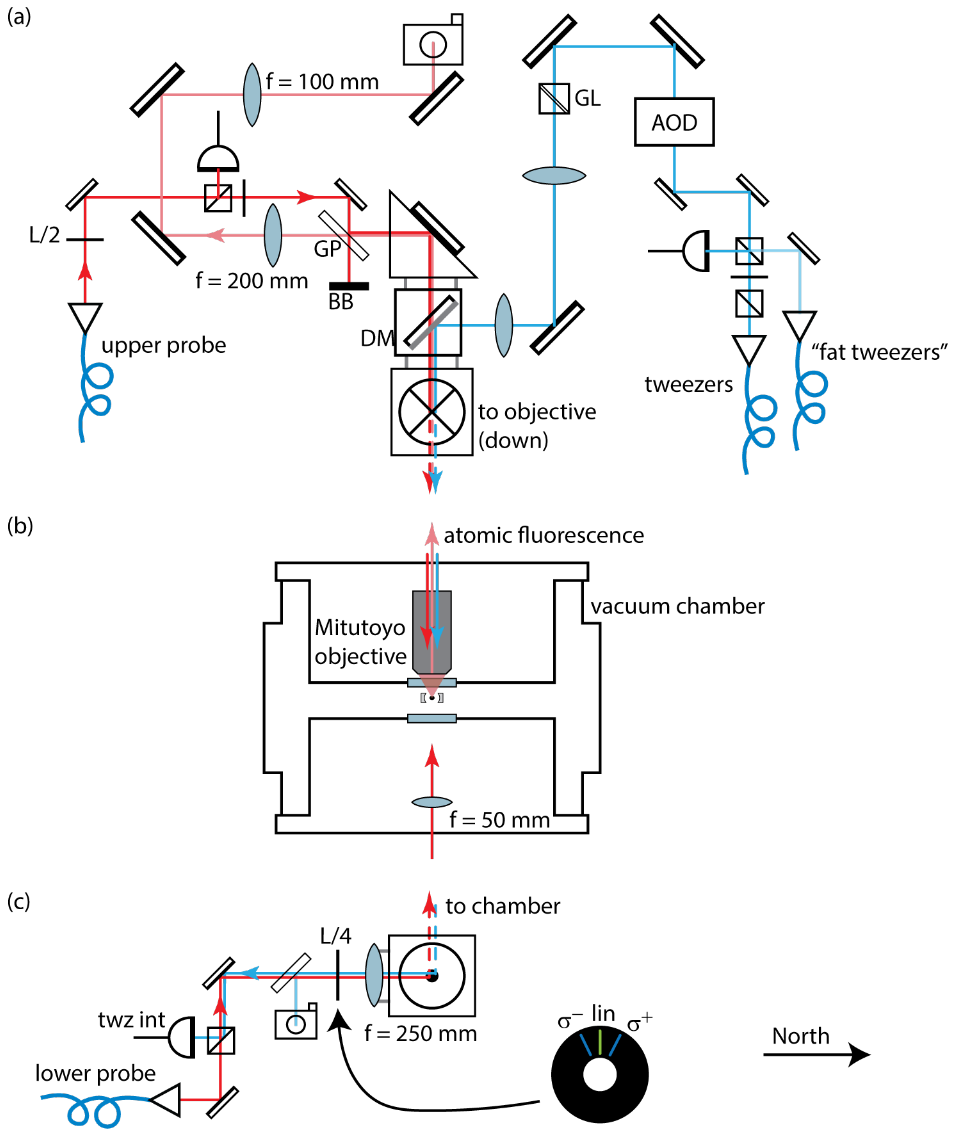

Figure 3.9: Upper and lower breadboards, bucket windows, and high NA optics. (a) Upper breadboard (top view). (b) Bucket windows and objective (side view). (c) Lower breadboard (top view).

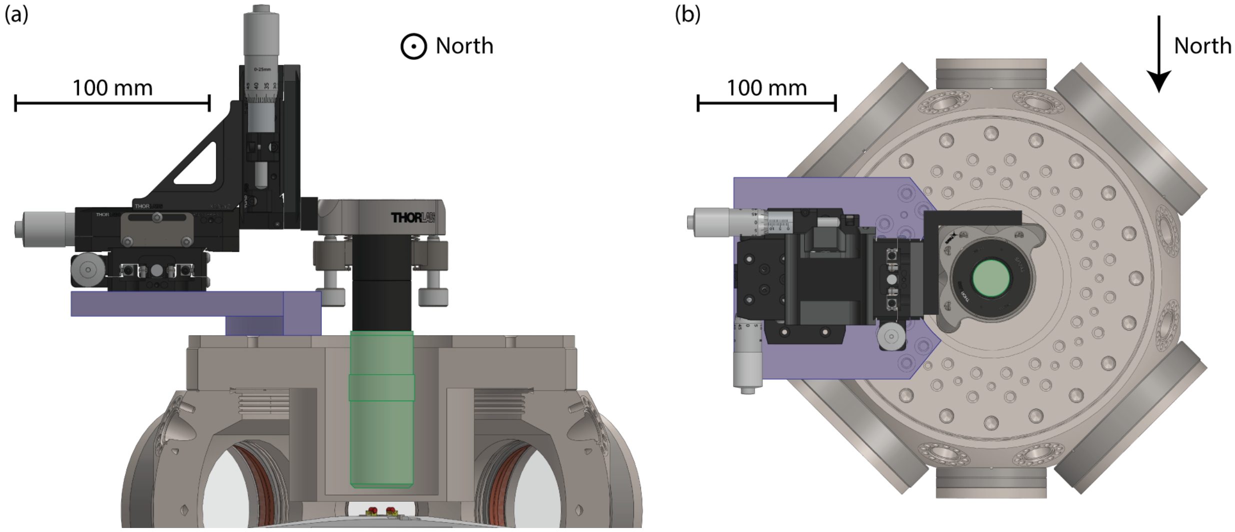

Figure 3.10: Objective mounting. (a) Side view. (b) Top view. The objective, highlighted in green, is attached via lens tubes to a kinematic mirror mount, which is mounted to xyz translation stages. The translation stage stack is mounted to a custom mounting platform, highlighted in purple, that is attached directly to the top flange of the science chamber.

the reentrant viewport. Given the long mechanical lever arm between the vacuum chamber and the objective, we do observe thermal drift between the science cavity and tweezer array, discussed more in Section 5.3.1.

Optical tweezers

The optical tweezer laser is a volume-holographic-grating (VHG) diode laser at a wavelength of 808 nm, with a maximum power output of 500 mW (Thorlabs LD808-SEV500). The laser output path is simple, consisting of a single-pass AOM for intensity control and switching, polarization cleanup optics, and several line filters to clean up the broad pedestal of the diode output. The light is coupled into a fiber and sent to the tweezer system on the upper breadboard; see Fig. 3.9(a).

The tweezer fiber output is collimated by an aspheric lens with a focal length of $f =$ 18.40 mm (Thorlabs C280TMD-B). This generates a large beam with a waist of around 1.8 mm, selected to fill the back aperture of the objective and create the tightest possible tweezer trap. After collimation, the tweezer beam goes through a PBS for polarization cleanup and power pickoff to a photodiode. The cleanup PBS is also used as an in-coupling port for a second diagnostic tweezer path that begins with collimation to a smaller beam waist of roughly 430 μm, resulting in a larger spot size at the atoms. It is thus referred to as the “fat tweezer” path and has been used to send 808-nm and 780-nm light through the objective for early stages of alignment.

The tweezer beam then goes through the acousto-optic deflector (AOD) that generates the tweezer array. The AOD (AA Optoelectronics DTSX-400-780) is driven by a PCIe arbitrary waveform generator (Spectrum Instrumentation M4i6631-x8). It has a center frequency of 105 MHz and bandwidth of 36 MHz. Each rf tone driving the AOD generates an optical tweezer trap, with tweezer spacings of roughly 5 μm per MHz. For the work presented in this thesis, we work with an array of 11 tweezers or less, limited by the tweezer laser output power. The one-dimensional array is oriented to be roughly perpendicular to the cavity axis, spanning the cavity mode radially. However, the AOD is mounted on a rotation mount to allow the array to be oriented along the cavity axis for future work. A natural future upgrade would be to replace the one-dimensional tweezer array with a two-dimensional one, with a static array formed by a DMD or SLM and a two-dimensional AOD used for atom-by-atom rearrangement.

The AOD output is relayed via a $4f$-imaging system consisting of two $f = 300$ mm achromatic doublets (Thorlabs AC508-300-B) to the back of the high-NA objective. Along the way, the tweezer light also passes through a GL polarizer for polarization cleanup. The polarizer is mounted on a rotation mount to carefully set the tweezer polarization to be linear at the atoms, as circularly polarized light at the tight tweezer focus can cause heating due to fictitious magnetic fields. This polarization is adjusted using the tweezer-trapped atom lifetime as the optimization signal. The final mirror of the tweezer path is piezo-actuated. This is used to move the tweezer along the cavity axis for the work described in Chapter 5 and Ref. [53].

Finally, the tweezer light is combined with the 780-nm upper probe and fluorescence imaging paths on a dichroic mirror (DM) with a cutoff wavelength of 808 nm (Thorlabs DMSP805) and sent down through the objective to the middle of the science chamber. Based on the PSF of the objective measured at the 780 nm imaging wavelength, we estimate the tweezer waist to be 750 nm. We have measured the tweezer trap depth through its ac Stark shift and typically operate with trap depths in the range $k_B \times (0.25 - 1.5)$ mK.

Fluorescence imaging

We've followed the tweezer path through the objective into the chamber; now we follow the imaging path back out.

Atomic fluorescence is collected and collimated by the high-NA objective, whose solid angle subtends 6.6% of isotropic free space emission. The objective has a transmission of 70% at the fluorescence wavelength of 780 nm. Fluorescence transmits through the dichroic mirror and a glass plate, used for coupling in the upper probe light. It is then imaged with a $f = 200$ mm achromatic lens (AC508-200-B) located roughly 400 mm from the objective and $2f$ imaging relay ($f = 100$ mm) onto an Andor Zyla 2.4 sCMOS camera with an imaging magnification of roughly 50. Line filters (FBH780-10) on a tube lens immediately in front of the camera reduce the imaging background counts.

The overall photon collection efficiency of this single-atom imaging system is estimated to be roughly 1.5%. The imaging detection noise can be found in Section 5.2.2.

Upper probe path

The upper probe fiber output, containing both fluorescence probe and repump light for local cavity detection, is coupled into the objective through the glass plate in the imaging system. Its fiber output is collimated to a beam size of roughly 430 μm, which is focused to a waist of 3.3 μm at the atoms. A PBS sets its polarization to be p–polarized, resulting in north-south linearly polarized light at the atoms. The counter-propagating lower probe path is east-west polarized at the atoms, realizing a lin$\perp$lin molasses configuration with the pair of local fluorescence probe beams.

3.2.5 Lower breadboard

Opposite the high-resolution system above the chamber is a simpler moderate-resolution system below, shown in Fig. 3.9(b) and (c). A diffraction-limited lens with NA= 0.20 (Thorlabs AL2550H-B) is positioned roughly its focal length ($f = 50$ mm) from the atoms, mounted directly to the science chamber lower flange like the objective above. A $f = 250$ mm lens and Thorcam (Thorlabs DCC1545M) complete the imaging system with a magnification of 5. This is used to image a small amount of tweezer light after propagation through the vacuum chamber, providing a useful diagnostic tool for monitoring the tweezers and testing new tweezer configurations, as well as aligning the upper probe light to the tweezers. The rest of the tweezer light goes through a PBS, used to couple in the lower probe light, to a PD for intensity stabilization of the total tweezer power.

Lower probe path

The “lower probe” fiber output contains a $f = 11$ mm collimating lens (C220TMD-B). The axial position of the collimator is used to set the size of the lower probe beam at the atoms. When the beam is properly collimated to a beam waist of 1 mm, the beam at the atoms has a waist of roughly 200 μm, large enough to span the entire tweezer array. This is the configuration used for global stretched state preparation described in Section 4.5.2.

The collimating lens can be displaced from the collimating position to create a smaller beam at the atoms, with a waist of 13 μm. This is the configuration used for local cavity measurement described in Chapter 6. The alignment of the collimating lens can be coarsely adjusted while looking at the image plane of the atoms, located between the mirror and glass plate in the lower probe input path, with a IR card or viewer. Fine adjustment can be done by monitoring a small amount of lower probe power on the Zyla single-atom imaging camera above to make the smallest spot.

The lower probe polarization is set using a $L/4$ mounted between the glass plate and $f = 250$ mm, with configurations generating $\sigma^{\pm}$ light for optical pumping to the stretched states indicated with blue marks. Linearly (east-west) polarized lower probe light is used for cavity measurement, indicated by the green mark, which effect a lin$\perp$lin optical molasses with the north-south polarized upper probe beam. Note that this $L/4$ is shared with the downward-propagating tweezer path, and affects the power picked off by the glass plate and BS, so the tweezer intensity stabilization should be recalibrated when the lower probe polarization is changed.

3.3 Cavity beam paths and detection

Here I describe cavity beam paths and detection system. These include the cavity lock light, used to lock the cavity length, and the cavity probe light, addressing the ^{87}Rb atom according to the Jaynes-Cummings interaction described in the previous chapter, and detected at the cavity output.

Justin's thesis [127] Section 6.3 details the heterodyne detection system that we built initially. Heterodyne detection allows one to measure amplitude and phase changes effected on the cavity probe light by atoms in the cavity, and has been used in our group for sophisticated measurements in cavity optomechanics [61, 136] and spin optodynamics [62]. For the work in this thesis, we partially dismantled the heterodyne system and replaced it with single photon counting. Single photon counting provides a more straightforward measurement of the light level coming out of the cavity with twice the detection efficiency of heterodyne's amplitude measurement, at the expense of the phase information. Future work on E6 will likely benefit from the sophistication and flexibility afforded by heterodyne detection, so I include the LO components in my schematics; I hope that this will aid with quick revival of the LO system when it is needed.

3.3.1 Cavity input

A schematic of the cavity input optics is shown in Fig. 3.11. These are arranged roughly according to the layout on the table, with some pairs of steering mirrors omitted. The cavity probe and lock light are directed into the science chamber at the southeast viewport, entering the cavity through its less transmissive mirror.

The cavity probe is collimated to a beam waist of about 5 mm using an achromatic lens with a focal length of 35 mm (Thorlabs AC254-035-B). This nontraditional choice for fiber collimation was made to create a large probe beam that could be directly coupled into the tightly focused cavity mode with a $f = 150$ mm focusing lens (Newport PAC21AR.16) positioned just outside the cavity input viewport, without requiring additional telescoping. After a $L/2$ and cleanup PBS, the probe beam goes through a 50/50 beam splitter (BS), which picks off half the probe power for intensity stabilization and the now-unused probe-LO optical phase lock. It then passes through a set of ND filters, effecting a total power attenuation of roughly ND= 7.5 (Thorlabs ND05A+NE20A+NE50A). These are used to reduce the probe fiber output power on the order of 1 mW to an intracavity photon number on the order of 1 during cavity measurement. The ND filters are removed when aligning the probe, overlapping the probe and lock laser frequencies, and measuring cavity detection efficiency. Next, the probe is directed into a PBS, once used to combine the probe and LO

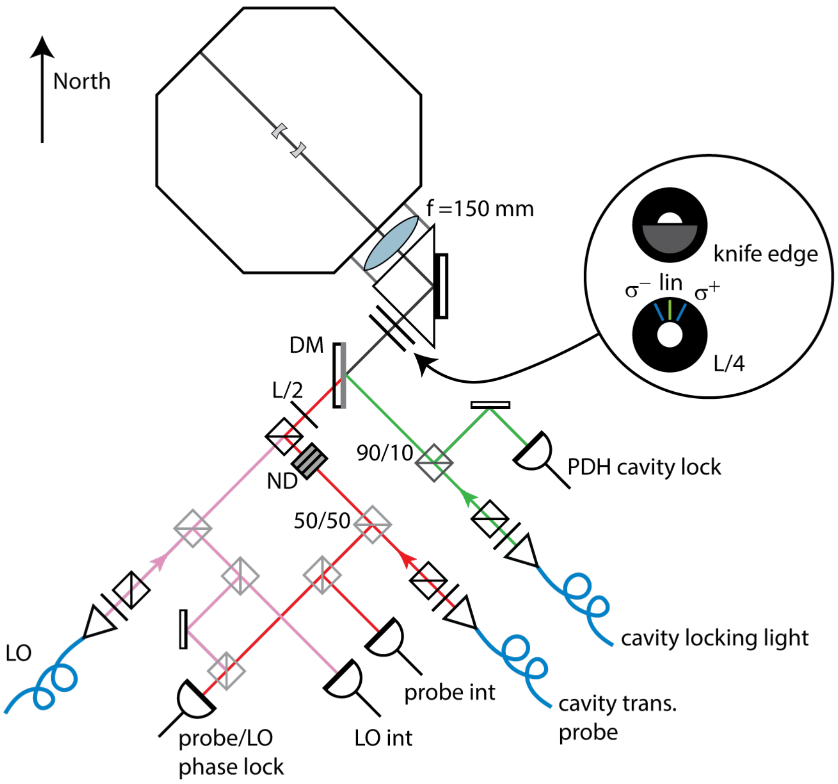

Figure 3.11: Cavity input optics

paths for parallel propagation through the vacuum chamber, and through a $L/2$ for linear polarization rotations, and then combined with the cavity lock light.

The cavity lock light is likewise collimated to a large beam waist at its fiber output using an achromatic lens (AC254-050-C). After polarization cleanup, it hits a 90/10 plate beam splitter (Thorlabs BSX18). The cavity reflection back to this 90/10 BS is used to lock the cavity length using a PDH lock in reflection, feeding back to the shear-stack piezo of a cavity mirror.[9] This lock sets the cavity length to some integer multiple of the 780-nm half-wavelength of the cavity lock light, thus also determining the frequency ω_c of the cavity resonance nearest the ^{87}Rb probe frequency. Note that the factor of two between the cavity probe and cavity lock wavelengths results in a factor of two between the frequency shifts needed to be applied to the two tones to maintain simultaneous resonance with the science cavity.

The cavity probe and lock light are combined on a dichroic mirror (Thorlabs DMSP950L) and pass through a shared $L/4$ at 780 nm and knife edge. Both were installed after the work described in Chapter 5, which uses linearly polarized TEM$_{00}$ modes of probe and lock light.

---

[9] The other port of the 90/10 BS was initially used for intensity stabilization of the cavity locking light; now intensity stabilization is performed using the transmitted cavity lock light.

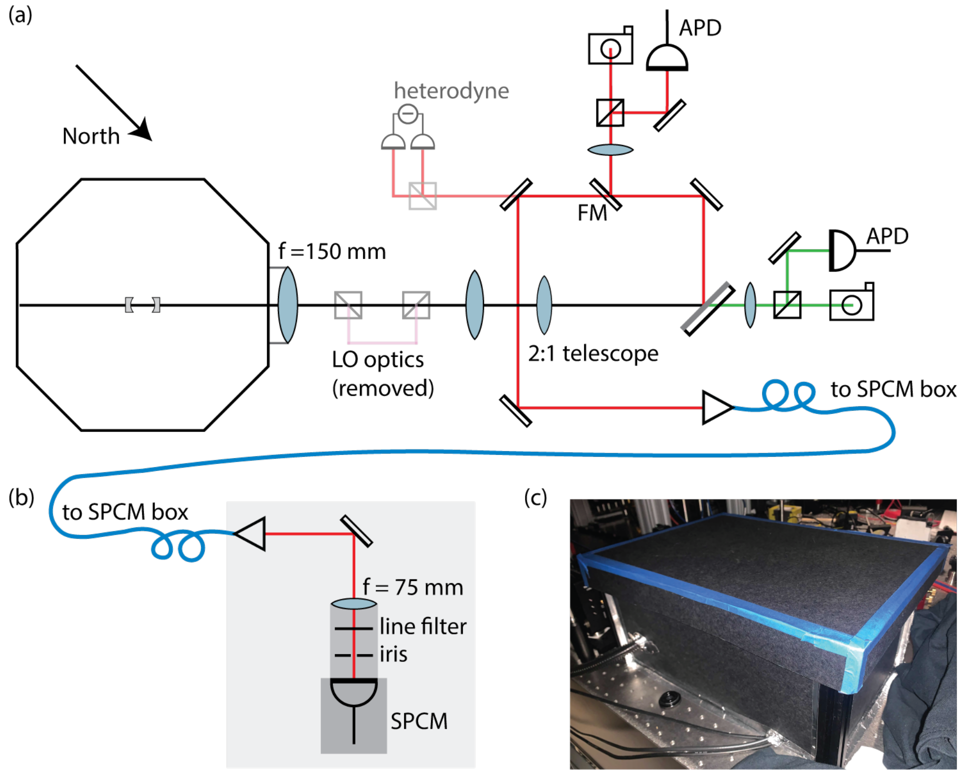

Figure 3.12: Cavity output and detection system. (a) Cavity output on chamber-level breadboard. (b) Cavity detection box interior, which contains a single photon counting module (SPCM). (c) Cavity detection box exterior.

For the work described in Chapter 6, the $L/4$ generates circularly polarized probe light for the cavity transmission measurement, and the knife edge enables locking the science cavity to a TEM_{01} mode of the cavity lock light.

The cavity beams are reflected off a silver mirror and focused into the cavity using a $f = 150$ mm achromatic lens (Newport PAC21AR.16) mounted directly to the science chamber viewport. The distance from the viewport to the center of the cavity is roughly 135 mm.

3.3.2 Cavity output

The cavity probe and lock beams, leaving the cavity through the more transmissive output mirror and the northwest window of the science chamber, have significant divergence due to the small cavity mode waists. They are immediately collimated, with the same $f = 150$ mm achromatic lens used on the input side, and then telescoped down with a $2:1$ telescope to a more manageable beam size for the detection optics. Two PBSs, previously used to separate and recombine the probe and LO beams, were removed.

The cavity output beams are separated using a long-pass dichroic. The transmitted locking light is divided: half is focused onto an avalanche photodiode (APD410C) used for intensity stabilization. The other half is imaged onto a diagnostic camera (Cinogy CinCam CMOS 1201-IR),[10] which allows us to identify higher order cavity modes such as the vertical TEM_{01} used to lock the cavity in Chapter 6.

The probe path contains a flip mirror (FM) after the dichroic with an analogous camera (Thorcam DCC1545M) and APD (Thorlabs APD410A) diagnostic detection system, used to optimize mode matching of the probe to the cavity TEM_{00} mode and to overlap the cavity lock and probe modes, both done with the probe input ND filters removed. When the flip mirror is down, the probe light is routed into a single-mode fiber. The cavity output is already a single spatial mode, so we achieve very good fiber coupling efficiency of up to 90%. The fiber is enclosed in black plastic tubing to prevent light from entering through the fiber cladding and directed to the single photon detection system.

3.3.3 SPCM detection system

The enclosed single photon detection system, shown in Fig. 3.12(b) and (c), is very simple: the fiber output is collimated, reflected off of a single steering mirror, and focused onto the single photon counting module (SPCM) with a spherical singlet with $f = 75$ mm. The distance from the focusing lens to the SPCM is enclosed with a lens tube, which also contains a 780 nm line filter to remove unwanted wavelengths and an iris to aid with optical alignment.[11] The SPCM is enclosed within a second black metal box inside the larger foam enclosure.

The SPCM (Perkin-Elmer SPCM-AQR-13) takes a 5 V power supply and outputs a TTL pulse with a duration of 35 ns whenever it detects a photon. The dead time between pulses is 50 ns. A gate input turns off the SPCM output when a TTL low voltage is applied. This gating is used to define probe intervals in the cavity measurement work described in Chapter 6. The measured quantum efficiency of the SPCM is 60%. The measured dark count rate is 400 counts per second, compared to the specification of 250 counts per second. The maximum detection rate is specified as 5 million counts per second (Mc/s). However, detection above 1 Mc/s causes self-heating, which increases the detector's dead time and can lead to dropped counts. For our cavity, with linewidth $\kappa = 2\pi \times 1.1$ MHz and detection efficiency of 26%, a photodetection rate of 1 Mc/s corresponds to an intracavity photon number of 0.6; in other words, this is a highly relevant experimental limit.

---

[10] It was difficult to find a camera sensitive to light at the cavity lock wavelength of 1560 nm. Shortwave infrared (SWIR) Indium Gallium Arsenide (InGaAs) cameras are very expensive; the Cinogy CinCam is a standard CMOS camera with a built-in IR phosphor filter that converts the incident IR light to a visible wavelength. The camera resolution, limited by the particle size in the phosphor coating, is about $5-9$ μm.

[11] This iris was added after we initially aligned to a backreflection from the SPCM's glass window; see Section 6.3. The SPCM's sensitivity to low light levels makes such a mistake possible.

3.3.4 Detection efficiency

The cavity detection system has a detection efficiency of $\eta \sim 25\%$, determined in the following way. With the probe input NDs removed, we measure the power just outside the cavity output viewport and in front of the optical fiber to the SPCM. Note that this must be done with the cavity lock light intensity stabilization turned off, as measuring the probe power requires blocking the lock output beam, causing the intensity stabilization to rail. The free-running intensity drift of the lock light is small enough to not significantly affect the measurement. The measurement must also be repeated with the cavity locked and unlocked, subtracting the power due to scattered probe late that is not transmitted through the cavity. The measured optical path efficiency is 81%. The fiber coupling efficiency has been as high as 90%, but for the data in Ref. [54] was 80%.

The quantum efficiency of the SPCM was measured by inserting calibrated ND filters (OD = 5.58, or attenuation of 2.6×10^{-6}) at the output of the detection fiber and comparing the power pre-attenuation with the attenuated photon counts, converted to an optical power according to the energy of each photon counted during the 5 ms detection time. This measurement yielded a quantum efficiency of 60%. The transmission efficiency of cavity photons through the output mirror is reported in Table 2.2 as $\eta_{\mathrm{out}} = 58\%$, based on the transmission and loss parameters of the cavity mirrors. The overall cavity detection efficiency, the product of these factors, is thus roughly 25%.

3.3.5 SPCM electronics

The SPCM output, a string of TTL pulses, has been recorded in two ways. Initially, the full output voltage trace was recorded using a PC-based oscilloscope system referred to as Gagescope (GaGe CompuScope 14200), intended for heterodyne detection. The voltage trace was then processed in software to convert the raw voltage trace to a series of time stamps indicating photon arrivals. The Gagescope card (a model from the year 2004 inherited from E3) failed after a few months of use, however, forcing us to implement a more appropriate photon-counting system.[12]

Jon Simon's group helped us implement a cheap and memory-efficient photon time-tagger system using an Opal Kelly FPGA board (XEM6001). The Opal Kelly records the timestamp of each photon arrival with a timing resolution of about 8 ns and saves the timestamp list as a binary file after each experimental shot. These data are then processed in software to determine the photon count during each probe interval and calculate quantities such as the $g^{(2)}(\tau)$ correlation function; see Chapter 6.

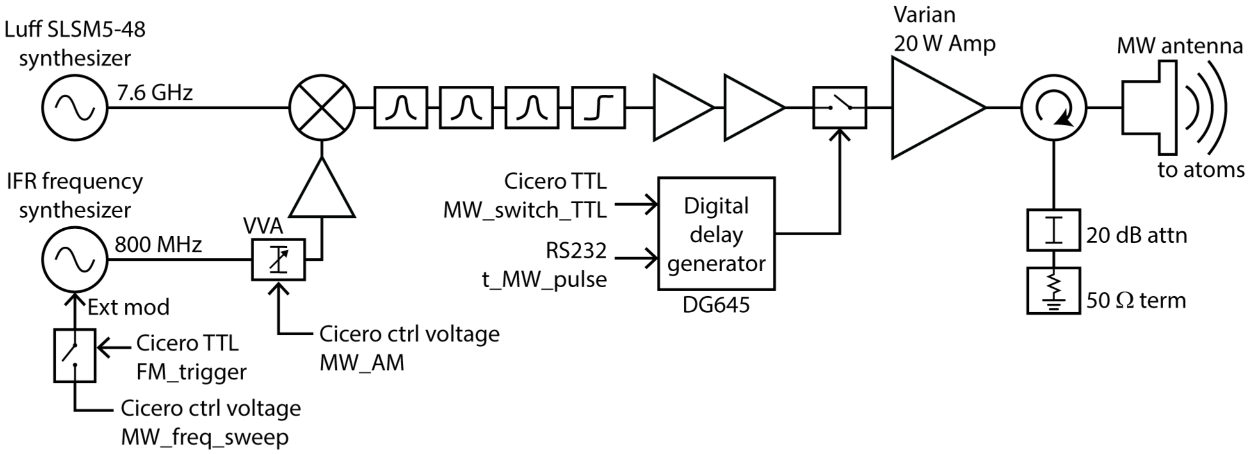

Figure 3.13: Microwave system block diagram

3.4 Microwave system

The microwave system used to drive between the $F = 2$ and $F = 1$ Zeeman state manifolds is shown in Fig. 3.13. A Luff SLSM5-48 frequency synthesizer generates a microwave signal 800 MHz plus a variable detuning $\delta\nu_{\mathrm{MW}}$ above the ^{87}Rb hyperfine frequency of $\nu_{\mathrm{Rb}} = 6.834$ GHz. The Luff synthesizer is programmed with a Python script over serial communication through a USB to RS485 adapter.[13] The Python control script receives the variable detuning $\delta\nu_{\mathrm{MW}}$ from Cicero, our experimental control software, at the beginning of each experimental iteration (shot). The Luff synthesizer output cannot be changed in real time during a shot.

Real-time frequency and amplitude control of the microwaves is achieved by mixing the Luff's fixed output with the output of a Marconi IFR 2042 frequency synthesizer, set to generate a signal at 800 MHz. The IFR synthesizer has an external modulation input that is used for frequency modulation via an analog control voltage from Cicero. This is used for real-time frequency modulation during experimental shots, enabling Landau-Zener sweeps and variable phase delays between $\pi/2$ pulses. However, the frequency modulation input is also a source of noise when a fixed frequency is desired, so the control voltage can be turned off with a TTL switch. Note also that the conversion between the control voltage MW_freq_sweep and corresponding frequency change depends on the IFR setting of "FM magnitude" selected on the front panel.

The IFR output goes through a voltage variable attenuator (Mini Circuits ZX73-2500+) for amplitude control and pre-amplifier (Mini Circuits ZFL-500LN+) before being combined

---

[12] Future heterodyne detection will require another PC-based oscilloscope or similar hardware, so we ordered a new Gagescope card (RazorMax PCIe CSE161G4).

[13] It can also be controlled using Luff's "SLSM5 Tuner" software, which is helpful during initial setup and troubleshooting.

with the Luff 7.6 GHz carrier. The output of the mixer (Mini Circuits ZX05-73L+) is thus three peaks, at the Luff synthesizer frequency $\nu_{\mathrm{Rb}} + \delta\nu_{\mathrm{MW}} + 800$ MHz and the sideband frequencies $\nu_{\mathrm{Rb}} + \delta\nu_{\mathrm{MW}}$ and $\nu_{\mathrm{Rb}} + \delta\nu_{\mathrm{MW}} + 1600$ MHz. The lower sideband at $\nu_{\mathrm{Rb}} + \delta\nu_{\mathrm{MW}}$ is used to address the atoms. We use this technique of frequency-modulating the IFR-generated sideband on the fixed Luff carrier because the IFR, originally purchased for a different lab and purpose, cannot generate a signal above 5.4 GHz, and the Luff cannot perform frequency sweeps. The combination, though a bit inelegant, provides what we need.

Three bandpass filters (Mini Circuits VBFZ-6260+) and a high-pass filter (Mini Circuits VHF-5500) follow the mixer to pick out the desired tone. Then the signal is amplified by two pre-amps (Mini Circuits ZX60-8008E+) and passes through a high-isolation RF switch (Analog Devices HMC-C019). The switch is triggered by a digital delay generator (SRS DG645) with a pulse length that is programmed by Cicero over RS232 serial communication and triggered by a Cicero digital channel. This enables precise timing control of $\pi/2$-pulses, below Cicero's timing resolution limit of 5 μs.

Finally, the signal is amplified to high power by a Varian amplifier (VZC6961K1) and delivered through a circulator to a rectangular waveguide microwave antenna (Narda-ATM 137-201B-2). The Varian amplifier's specifications indicate a gain of 35 dB and maximum output power of 20 Watts; the maximum power we have measured at the output of the amplifier is 12 Watts.[14] The antenna points into the science chamber at the southwest viewport of the science chamber. Its output polarization is uncontrolled.

The third port of the circulator goes through a 20 dBm attenuator to a 50 Ohm terminator. This circulator port provides a nice place to plug in a spectrum analyzer or microwave power meter for microwave system diagnostics. The reflected microwave power measured here should be minimized while positioning the antenna to maximize the power directed toward the atoms.

---

[14] The light indicator on the Varian front panel stops at two bars. I assume that if it were new, the whole panel would light up, and that this is related to the lower measured output power.

Chapter 4

Experimental methods

In this chapter, I describe the experimental methods, beginning with laser cooling and trapping in a magneto-optical trap, and ending with experiments using single atoms trapped in a tweezer array spanning the science cavity. Fig. 4.1 guides us through the different steps of the experimental sequence. Along the way, I point out alignment methods that we have found useful for optimizing the different experimental transitions. The durations of experimental stages (MOT and ODT loading, optical transport, imaging exposure, etc.) are sometimes optimized differently according to what a particular experiment requires; here I describe a typical sequence that was optimized for a fast cycle time, for experiments with up to ten atoms in the tweezer array.

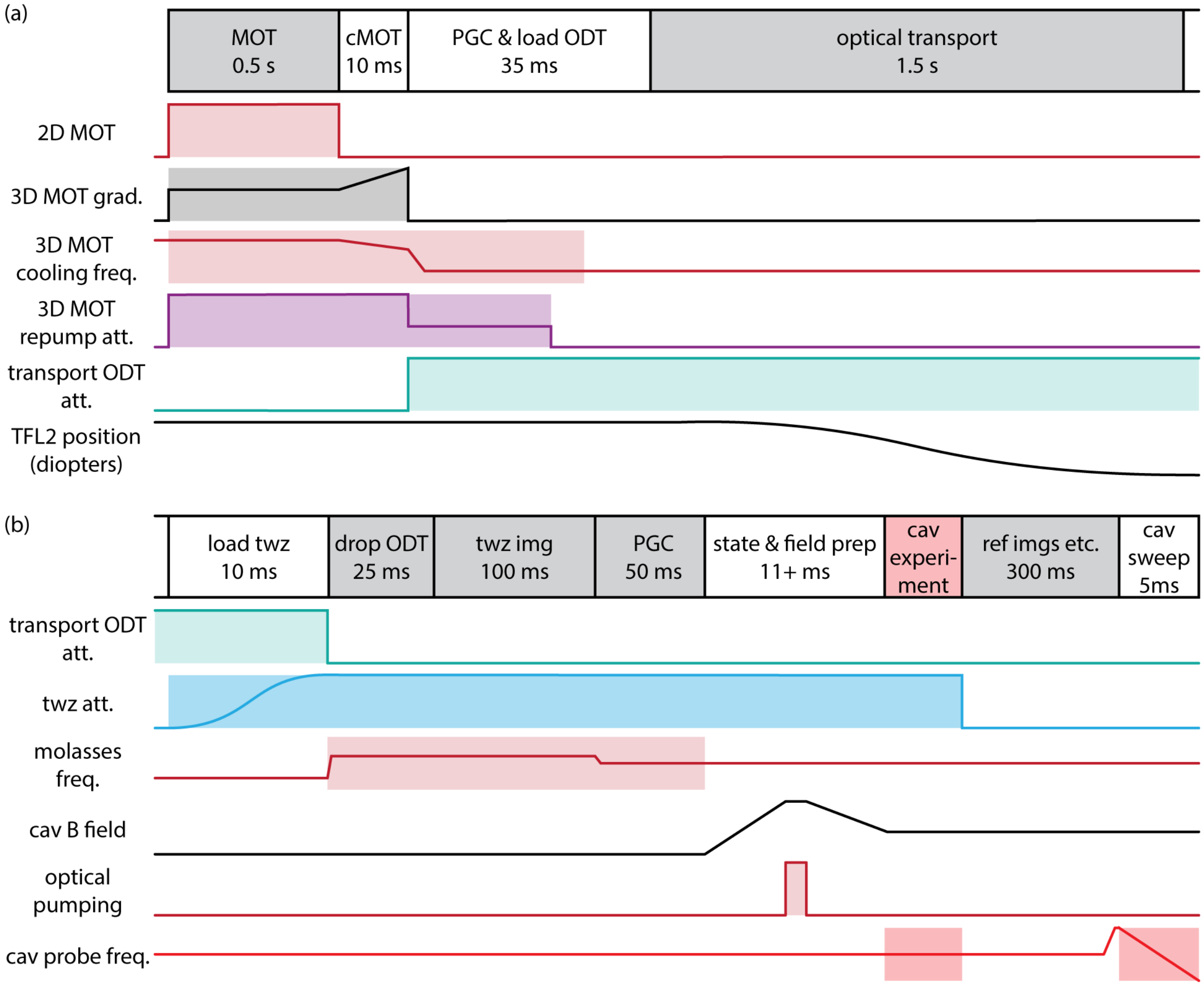

Figure 4.1: Experimental sequence. (a) From MOT loading to optical transport. (b) From tweezer loading to the end of the sequence. The cavity experiment, highlighted in red, takes a small fraction of the experimental cycle time. Long time steps, shaded in gray, are not to scale.

4.1 MOT

The sequence begins with laser cooling and trapping in 2D and 3D MOTs. Our 2D MOT creates an atomic beam directed into the MOT chamber, where we load a 3D MOT for 0.5 s. During MOT loading, the MOT gradient is 16 G/cm and the cooling light detuned from the ^{87}Rb $F = 2 \rightarrow F' = 3$ transition by $-2\pi \times 17$ MHz. 3D MOT loading is followed by a 10 ms compressed MOT (cMOT), wherein the 3D MOT field gradient is ramped to 28 G/cm and the cooling light detuning brought to $-2\pi \times 30$ MHz. Then the magnetic field gradient is turned off altogether for a stage of polarization-gradient cooling (PGC) under zero magnetic field. The cooling light detuning is set to $-2\pi \times 60$ MHz, and the repump intensity is reduced.

Coarse optimization of the 2D MOT can be done using a security camera looking down the axis of the 2D MOT glass cell. When the 2D MOT is optimized, one can see fluorescence from the atomic beam overlapped with the differential pumping tube leading from the 2D MOT cell to the 3D MOT chamber. The position of the atomic beam is tuned using the current to each of the four 2D MOT coils, after the 2D MOT beam polarizations and power balance has been set. Fine-tuning of the 2D MOT is done using the 3D MOT atom number as an optimization signal, by measuring the 3D MOT atom number in absorption imaging or by detecting 3D MOT fluorescence with a photodiode and oscilloscope. The latter method allows for a simpler 2D MOT optimization sequence, just toggling the 3D MOT on and off, and a faster duty cycle. This photodiode should not be used to optimize the 3D MOT parameters, as it may lead you to an odd 3D MOT configuration that sends maximal fluorescence to the photodiode but does not optimize the atom number.

The 3D MOT parameters are optimized using MOT absorption imaging. The security camera, now looking into the 3D MOT chamber through the viewport opposite the 2D MOT cell, comes in handy again for optimizing PGC: when the atom number is sufficiently high and PGC is working, one can see the atomic vapor slowly diffuse during a long (~ 1 s) PGC duration. Otherwise, the atoms rapidly disappear and can even be seen to be pushed in a particular direction by unbalanced cooling beams.

Typical 2D MOT and 3D MOT operation typically results in loading roughly 1.5×10^8 atoms in 2 seconds; we use a MOT loading time of 0.5 s for a rapid experimental cycle, since only a few atoms are used for the ultimate cavity experiment.

4.2 Optical transport

The transport optical dipole trap (ODT) is turned on during PGC, focused at the MOT location with a power of 6 W. Overlap between the MOT and ODT is optimized using the MOT absorption imaging signal. The location of the center of the MOT can be seen by imaging a small MOT immediately following PGC, and tuned by adjusting bias fields during MOT loading.[1] The optically trapped atoms can be seen after allowing the MOT to

---

[1] Remember to turn the bias fields off for PGC, which requires zero magnetic field!

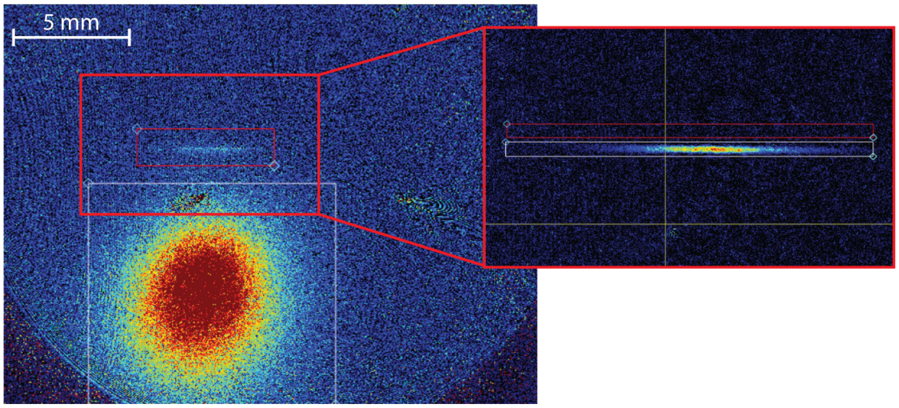

Figure 4.2: MOT chamber absorption imaging. Atoms trapped in the ODT can be seen above the falling MOT. The inset shows the ODT with optimized atom loading.

drop away for tens of milliseconds; see Fig. 4.2. Using this signal, the transport ODT atom number is optimized by tuning the MOT position (bias fields), PGC duration, and TFL2 focal position. The ODT alignment can also be adjusted if necessary, but this will require realigning the ODT to the cavity and tweezer array as well. Typical ODT loading after a 2 s MOT yields 5×10^5 atoms at a temperature of about 30 μK. During the PGC and ODT loading word, the cooling light is left on for 5 ms longer than the repump light. This prepares the atoms in the $F = 1$ ground state, which results in improved transport efficiency compared to $F = 2$ atoms.

The atoms are transported into the science chamber by tuning the TFL2 focal power from about -1 dpt to -5.6 dpt using a two-point cubic spline. A transport duration of 2 s results in transport efficiency of over 60%, measured using repeated back-and-forth transport between the MOT and science chambers. For fast cycle time, we operate at the shortest transport duration of 1.5 s; we have found that faster transport results in unmanageable atom loss.

4.3 Cavity, ODT, and tweezer alignment

In the science chamber, the transport ODT, tweezer array, and fluorescence imaging molasses must meet at the center of the science cavity, a tricky alignment when no initial signal is present. Here I take a brief detour from the description of the experimental sequence to describe how this alignment is done, using the side absorption imaging and upper fluorescence imaging systems in the science chamber after transport.

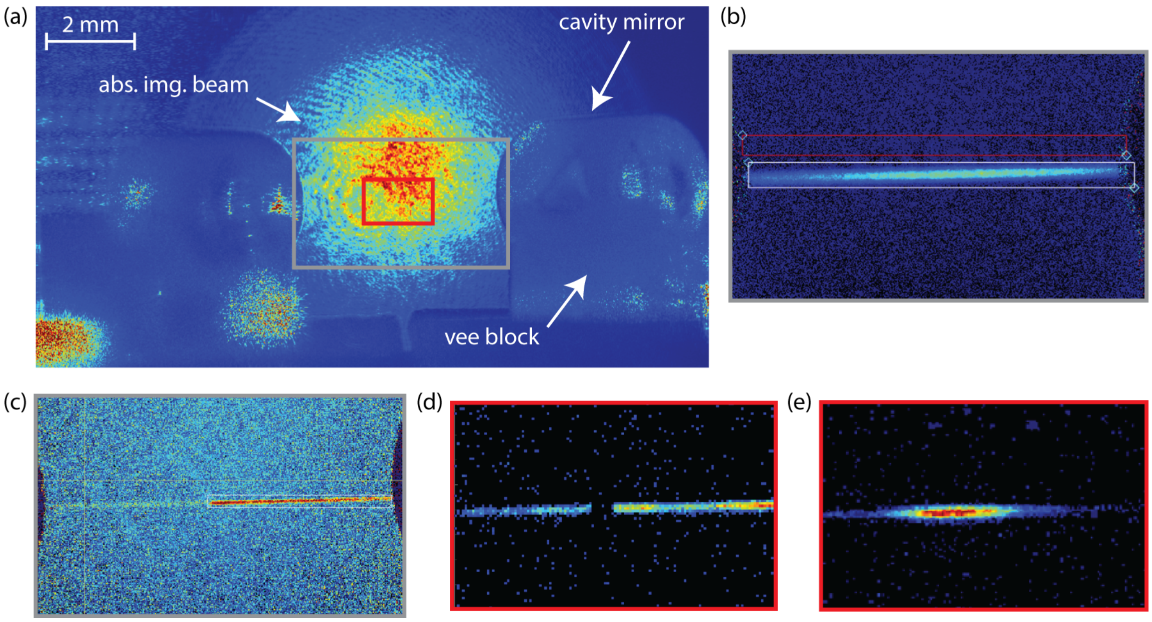

Figure 4.3: Science side absorption imaging. (a) The large field of view encompasses the whole science cavity, here illuminated with the large absorption imaging beam. Gray and red boxes indicate the regions shown in (b-c) and (d-e). (b) The optically trapped atomic cloud after transport into the science cavity. (c) When the transport ODT intersects with a bright cavity lock mode, atom loss is apparent. (d) The BAB, aligned to the transport ODT using this atom loss signal, serves as a guide beam for the tweezers. (e) PGC within the transport ODT due to properly aligned fluorescence imaging molasses (molasses 1) is visible as a density enhancement.

4.3.1 Side absorption imaging

The side absorption imaging system has a large field of view that encompasses the entire science cavity, viewed at an angle of 45°. This is shown in Fig. 4.3(a).

First, the transported atom cloud is centered within the science cavity, as shown in Fig. 4.3(b), by tuning TFL2. Note that the atom cloud is very long along the transport axis: a Gaussian beam waist of 50 μm at the transport ODT wavelength of 1064 nm has a Rayleigh range of 7.4 mm, fully spanning the projection of the science cavity at its 45° orientation. Still, variation of .05 in the TFL2 cavity diopter setting leads to displacement of the transport ODT from the cavity center and poor tweezer loading. The transport ODT monitoring pinhole described in Section 3.2.2 assists with frequent adjustment of this control parameter.

The transport ODT is then aligned vertically to the cavity axis by locking the cavity with a large amount of cavity lock light. When the transported atoms hit the cavity lock mode, atom loss is clear in the absorption imaging: Fig. 4.3(c). Under normal experimental operation, the cavity lock intensity is reduced to a level that does not cause this loss.

Now the tweezer array must be aligned to the intersection of the cavity and ODT. Tweezer-trapped single atoms are not visible in side absorption imaging, so a resonant guide beam propagating through the chamber from below is used for tweezer alignment. This beam is the 780 nm blow-away beam (BAB), used also for state detection as described in Section 4.5.3. The BAB blows a hole in the atom cloud held in the transport ODT, as shown in Fig. 4.3(d), which is then aligned to overlap with the cavity intersection point. When the BAB is aligned to the upper Zyla camera and the tweezer light aligned to the BAB, the tweezer array is at the correct location with respect to the cavity and ODT, and within the field of view of the single-atom fluorescence imaging system.

Single-atom fluorescence imaging also requires proper alignment of the imaging molasses, using the molasses 1 path described in Chapter 3.2.3. With the retroreflection blocked, the molasses light blows a hole in the ODT-trapped cloud, similar to the BAB. When the retroreflection is aligned well (and both beams correctly polarized for optical molasses), the effect of PGC is visible as a density enhancement in the center of the cloud: see 4.3(e).

4.3.2 Fluorescence imaging

After aligning the ODT, cavity, tweezers, and molasses using side absorption imaging, fluorescence imaging is used for the final alignment of the imaging system and tweezer focal plane, and more careful optimization of the imaging molasses. The objective's vertical z position is tuned using a piezo-actuated translation stage to image the ODT-cavity plane, as shown in Fig. 4.4(a). Note that the optimal imaging parameters (molasses detuning and exposure time) are different for imaging atoms trapped in the transport ODT versus the tweezer array.

Fluorescence imaging of the ODT can also be used to see the cavity position, as the cavity lock light effects an ac Stark shift that changes the effective molasses detuning at the cavity location. This is shown in Fig. 4.4(b), and is the basis of the ac Stark shift measurement described in Ref. [53] and Chapter 5.

Finally, the tweezer array, aligned to the counter-propagating BAB as a guide, is overlapped with the ODT, enhancing the density of the trapped gas at the tweezer locations. The tweezer focal plane is adjusted to maximize this signal, shown in Fig. 4.4(c), using the tweezer fiber output collimator. This completes the alignment procedure used to prepare for single-atom fluorescence imaging.

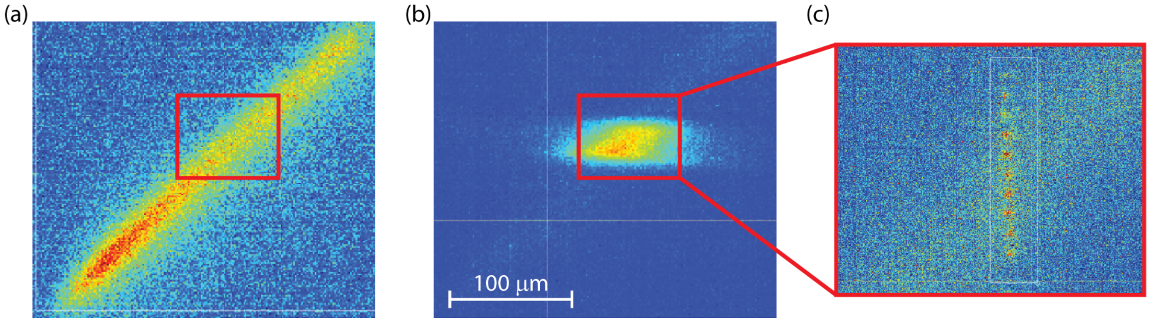

Figure 4.4: ODT fluorescence imaging. (a) Atoms trapped in the ODT. (b) Atoms trapped at the intersection of the ODT and the cavity lock light. The fluorescence imaging detuning has been shifted to image the atoms experiencing the ac Stark shift of the cavity lock light. (c) Zoom-in of the atomic density enhancement in the ODT due to optical tweezer light (these are not trapped single atoms). These signals are used to overlap the transport ODT, cavity mode, and tweezer array.

4.4 Single atom trapping and imaging

After transport, the atoms are loaded in the tweezer array. The tweezer light is ramped on in a cubic spline over 10 ms, after which time the ODT is turned off and molasses light, detuned from the ^{87}Rb cooling transition by $-2\pi \times 30$ MHz, turned on. Photo-assisted collisions mediated by the molasses light leave each tweezer with an occupation of zero or one atom [27]. A 25 ms hold time ensures that the transport ODT atoms have fallen away before a fluorescence image with an exposure time of 100 ms is taken to determine the initial tweezer occupation.

An averaged image of a ten-tweezer array and histogram of the measured counts within the indicated region of interest (ROI) are shown in Fig. 4.5. Using a threshold, we determine if each tweezer contains an atom. For the work in this thesis, this image is used to postselect data with atoms. Since I left the lab, the experiment has been upgraded with deterministic tweezer loading, as has become typical for tweezer array experiments after the first demonstrations in Refs. [29, 30].

4.4.1 Moving tweezers

For the work in Ref. [54] and Chapter 6, we use a two-tweezer array in two configurations: first, atom A is held within the cavity and atom B without, and then the array is translated through the cavity to place atom B within the cavity and atom A without (on the other side). The tweezers are moved by sweeping the frequency tones driving the AOD, programmed using an arbitrary waveform generator (AWG). Care must be taken to match up the phases between the static tweezer waveforms and the sweep waveform, which is initiated with a trigger using the "sequence replay" mode of the Spectrum Instrumentation M4i6631-x8 AWG. We use a

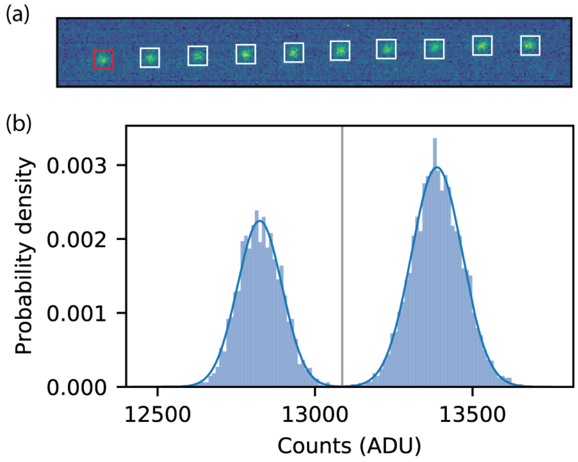

Figure 4.5: Single atom imaging. (a) Averaged image of a ten-tweezer array. Boxes indicate ROIs used for single-atom detection. (b) Bimodal counts distribution for the red ROI in (a). Binary tweezer occupation is determined using a threshold (gray line).

sweep with a smooth $1-\cos(x)$ velocity profile to move the tweezers up to 40 μm in 200 μs. A shorter sweep duration of 80 μs leads to atom loss of roughly 35%; we do not observe atom loss with a 200 μs sweep.

4.5 State preparation and detection

After the atoms have been trapped and imaged in the tweezer array, we perform state preparation, according to the experiment that will follow. For the results presented in Chapter 5 and Ref. [53], no state preparation is necessary, as the ac Stark shift measurement is based on state-insensitive fluorescence imaging. For the results presented in Chapter 6 and Ref. [54], we prepare the atom in the $F = 2$ or $F = 1$ ground state manifold to characterize the single-atom cavity measurement, or in the $|F = 2, m_F = 0\rangle$ clock state for the two-atom Ramsey experiment. In future work, we might wish to prepare the atoms in the $|F = 2, m_F = \pm 2\rangle$ states, which can achieve the strongest Jaynes-Cummings coupling g to $\sigma^{\pm}$–polarized cavity modes, per the stretched-state Clebsch-Gordon coefficients.[2] Here I will describe our state preparation protocols for all of these, as well as our loss-based state detection method.

---

[2] Circularly polarized cavity probe light can also effect optical pumping to the stretched states, as we learned while studying the cavity transmission measurement; see Section 6.4.2.

4.5.1 Manifold preparation

Preparing atoms in the $F = 2$ and $F = 1$ manifolds without Zeeman-specificity is straightforward and technically easy, due to the large hyperfine splitting of $2\pi \times 6.8$ GHz. State preparation just requires illumination with light at the right frequency, independent of polarization.

Preparation in the $F = 2$ manifold is achieved by illuminating the atoms with repump light that enters the science chamber through the side absorption imaging path; see Section 3.2.3. We call this the "global repump" light, as the large beam illuminates the entire tweezer array. This name distinguishes it from the "local repump" beam, which enters the science chamber from the upper probe path and is tightly focused in the center of the cavity for local cavity state detection. Illumination with global repump light for 2 ms prepares the atoms in $F = 2$ with a state preparation error below 0.6%. As discussed in Ref. [54], we cannot distinguish state preparation error from measurement error, but we see that longer repump time does not help.

Preparation in the $F = 1$ manifold is done analogously, by illuminating the atoms with depump light resonant with the $F = 2 \to F' = 2$ transition. We initially used $F = 2 \to F' = 3$ cooling light for preparation in the $F = 1$ manifold, as is done before optical transport. However, since it relies on off-resonant coupling through the $F' = 2$ excited state, this method is slower and lower effective than using resonant $F = 2 \to F' = 2$ depump light. The depump light used for $F = 1$ manifold preparation enters the science chamber through the "molasses 2" path. Illumination with depump light for 0.75 ms prepares $F = 1$ atoms with a state preparation error below 0.9%.

4.5.2 Zeeman state preparation

Preparation in a specific $|F = 2, m_F\rangle$ Zeeman state requires simultaneous illumination with depump and repump light. Proper polarization configurations of depump light create so-called "dark states" within the $F = 2$ manifold, from which there are no dipole-allowed transitions that the depump light can drive. After multiple scattering events between the $F = 2$ and $F = 1$ manifold, the atom is eventually optically pumped into the dark state, where it remains. The polarization of the repump light is not important, as dipole selection rules do not create dark states with respect to the $F = 1 \to F' = 2$ transitions. The depump polarizations used to optically pump the atoms into the $|F = 2, m_F = -2, 0, +2\rangle$ dark states are shown in Fig. 4.6. We perform all of our optical pumping with a magnetic field of 5 G applied in the $+z$ vertical direction, ramped linearly in 5 ms from the zero-field condition used for fluorescence imaging. After optical pumping, the field is ramped in another 5 ms to the desired configuration for the cavity experiment.

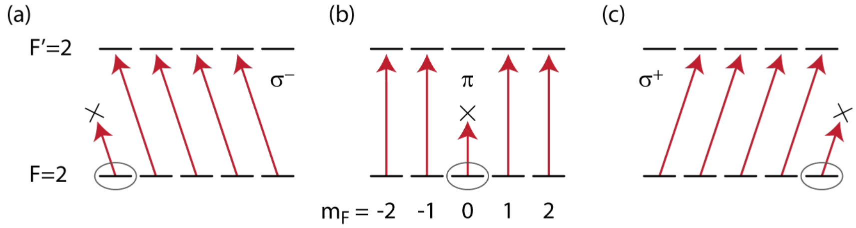

Figure 4.6: Optical pumping and dark states. Simultaneous illumination with repump and depump light of a particular polarization optically pumps ^{87}Rb atoms to the desired Zeeman state. (a) σ^-–polarized light pumps to $|F=2, m_F=-2\rangle$. (b) π–polarized light pumps to $|F=2, m_F=0\rangle$. (c) σ^+–polarized light pumps to $|F=2, m_F=+2\rangle$.

Stretched states

Atoms are optically pumped to the $|F=2, m_F=\pm 2\rangle$ stretched states under illumination with σ^+– or σ^-–polarized depump and repump beams, which enter the science chamber through the lower probe fiber. The $L/4$ configurations for $\sigma^\pm$ pumping are indicated in Fig. 3.9(c).

Our best stretched-state preparation was achieved with a repump power of approximately 30 μW and depump power of approximately 15 μW, measured at the output of the lower probe fiber, and an optical pumping duration of 35 μs. Note that this was done with the lower probe fiber output collimated, generating an optical pumping beam waist of roughly 60 μm at the atoms for global state preparation in the tweezer array.[3] We estimate this m_F state preparation fidelity to be about 95%, based on the Zeeman spectrum measured using Landau-Zener sweeps; see Section 4.5.3. This could likely be improved with more careful optimization.

Clock state

Atoms are optically pumped to the $|F=2, m_F=0\rangle$ clock state under illumination with repump and π–polarized depump. Selection rules forbid the $|F=2, m_F=0\rangle$ to $|F'=2, m'_F=0\rangle$ π transition, for which $\Delta F=\Delta m_F=0$. π–polarized depump light is sent into the chamber via the molasses 2 path, with its polarization set to be vertical. This polarization setting is very sensitive, as misalignment between the magnetic field axis and depump polarization allows $\sigma^\pm$ transitions out of the $|F=2, m_F=0\rangle$ state, making the dark state "less dark." Simultaneous repump illumination comes through the side absorption imaging "global repump" path. The global repump polarization is the linear opposite of the molasses 2 path: horizontal, or a mix of $\sigma^\pm$.

---

[3] The lower probe collimating lens was later adjusted to generate a small lower probe beam waist of 13 μm for local cavity fluorescence detection; see Section 3.2.5.

As with optical pumping to the stretched states, π optical pumping is done with roughly comparable intensities of depump and repump light. As the molasses 2 and side imaging paths generate quite different beam waists at the atoms (see Section 3.2.3), these intensities were set to be roughly equal by looking at the depump and repump timescales under illumination with each beam alone. An optical pumping duration between 200 μs and 1 ms yields a $|F=2, m_F=0\rangle$ state preparation fidelity of 90%.

4.5.3 State detection

We perform global state detection by driving state-selective loss using resonant $F = 2 \to F' = 3$ light as a "blow-away beam" (BAB), which blows away atoms in the $F = 2$ ground state, and then imaging the remaining $F = 1$ atoms. This is a standard state detection technique, also referred to as "push-out" detection [137–139]. Global BAB state detection is useful for optimizing state preparation and microwave protocols, and provides an important complement to the single-atom cavity detection that we demonstrate in Chapter 6 and Ref. [54], which is not particularly well-suited to measuring the state of many atoms in a tweezer array.

The BAB shares the lower probe path, also used for stretched-state optical pumping and local cavity detection. Early state detection efforts used the large side absorption imaging beam as a BAB, but the smaller lower probe beam achieves better state detection fidelity. Future work may benefit from adding a second lower probe path to accommodate the different output beam waists required for global BAB detection and stretched-state optical pumping versus local cavity detection; currently, these are configured manually by adjusting the setting of the lower probe collimating lens.

Zeeman state detection

Zeeman state population within the $F = 2$ manifold is measured by adding microwave manipulation under an applied magnetic field before BAB or cavity state detection: a microwave Landau-Zener (LZ) sweep is performed, centered at some microwave detuning $\delta\nu_{\mathrm{MW}}$ from the $F = 1 \to F = 2$ hyperfine transition frequency of 6.8 GHz. These LZ sweeps have a duration of 20 ms and total sweep range of roughly 70 kHZ, set using a frequency modulation magnitude of 50 kHz on the IFR front panel and linear Cicero control voltage sweep of MW_freq_sweep from -1 to 1 V; see Section 3.4 for a complete description of the microwave system. When the LZ sweep range encompasses the correct Zeeman-shifted transition frequency, atoms are adiabatically transferred from $|F=2, m_F\rangle$ to $|F=1, m'_F\rangle$. The BAB is then applied, blowing away all remaining $F = 2$ atoms, so that the final fluorescence image of the $F = 1$ atoms indicates the initial $|F=2, m_F\rangle$ population.

Fig. 4.7 shows the LZ transfer probability as a function of $\delta\nu_{\mathrm{MW}}$ for atoms prepared in the $F = 2$ manifold without Zeeman-state selectivity, as described in Section 4.5.1. The unpolarized microwave field drives transitions at 7 resonance frequencies, as indicated, separated by a frequency difference of 1.2 MHz that corresponds to an applied magnetic field of

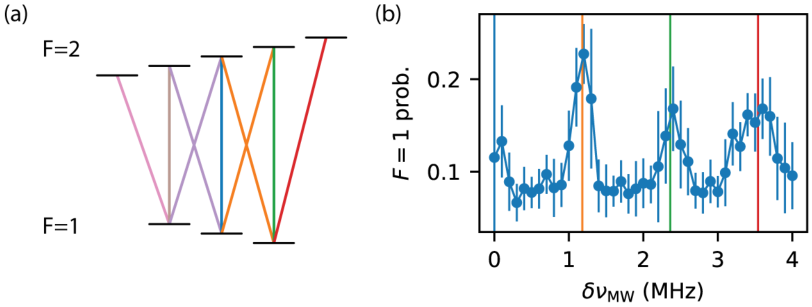

Figure 4.7: Zeeman state detection. (a) Landau-Zener (LZ) sweeps centered at $\delta\nu_{\mathrm{MW}}$ drive transitions from $|F = 2, m_F\rangle$ to $|F = 1, m'_F\rangle$. (b) The $F = 1$ detection probability versus $\delta\nu_{\mathrm{MW}}$ exhibits 7 peaks at the Zeeman-shifted transition frequencies ($\delta\nu_{\mathrm{MW}} > 0$ shown here). These data are taken with a probabilistically loaded ten-tweezer array. The peak on the right, corresponding to the $|F = 2, m_F = 2\rangle \to |F = 1, m_F = 1\rangle$ transition, is maximized to optimize σ^+ optical pumping; the center peak, corresponding to the $|F = 2, m_F = 0\rangle \to |F = 1, m_F = 0\rangle$ transition, is maximized to optimize π optical pumping.

1.7 G. The broad widths of the resonances may be due to magnetic field noise or fictitious magnetic fields due to circularly polarized tweezer light.

From data such as these, we calculate the Zeeman state populations, assuming constant LZ transfer efficiency for $\sigma^\pm$ and π transitions due to our uncontrolled microwave polarization. Optical pumping is optimized by maximizing the peak (or peaks) corresponding to transitions out of the desired $|F = 2, m_F\rangle$ initial state. This signal is also used to zero the magnetic field in the science chamber, tuning the field to collapse the peaks onto the zero-field resonance.

4.6 Cavity experiment

After atoms have been cooled, trapped, and delivered to the tweezer array, imaged for postselection based on tweezer population, and prepared in the desired initial state, the cavity experiment begins. This portion of the sequence varies greatly based on the experiment in question. The two cavity experiments that were performed during my PhD are described in Refs. [53, 54], with more detail given in Chapters 5 and 6. The cavity experiment duration is a small fraction of the experimental cycle time, which is dominated by atom preparation, specifically MOT loading and optical transport.

After the cavity experiment concludes, reference images are taken to determine the final tweezer occupation and measure background imaging and cavity detection levels. Finally, the cavity probe is swept across cavity resonance to measure the empty cavity transmission profile, used to track the cavity frequency drift during long experimental runs.

Chapter 5

Cavity characterization using single atoms

This chapter discusses our published experimental work on using single tweezer-trapped atoms for superresolution microscopy of optical fields, published in Ref. [53] and provided in Appendix A. The text below presents additional material and does not reproduce the content of that published work.

This chapter discusses our characterization of our bichromatic cavity, using single atoms as scanning probes to measure the local ac Stark shift due to cavity light at the cavity probe and cavity lock wavelengths. What began as our attempt to understand the relative phase between the nearly commensurate probe and lock standing waves became a result in single-atom sensing, where the cavity fields serve as standing-wave "test patterns" for a superresolution measurement. This work is published in Ref. [53] and demonstrates the key features of our apparatus in action, despite being a bit of a detour from our general motivation in cavity QED. Ref. [53] is included in Appendix A.

In this chapter, I start with a description of the bichromatic cavity and how we got into this project initially, before elevating the work to a stand-alone project. Then I describe the basic measurement method, followed by some details on the measurement sensitivity and noise, and how the performance of our realized single-atom sensor compares to an ideal one. This discussion was motivated by questions we received during peer review, and may also be useful to those who wish to improve the sensor performance in the future. I also discuss the measurement resolution, and the data processing used to detect and correct a slow relative drift between the tweezer array and cavity, after which we were able to achieve a superresolving measurement. Finally, I detail the model and fit function used to characterize the cavity probe mode in Ref. [53], and summarize the experimental takeaways from this work that I believe will be most relevant for our future experiments in cQED.

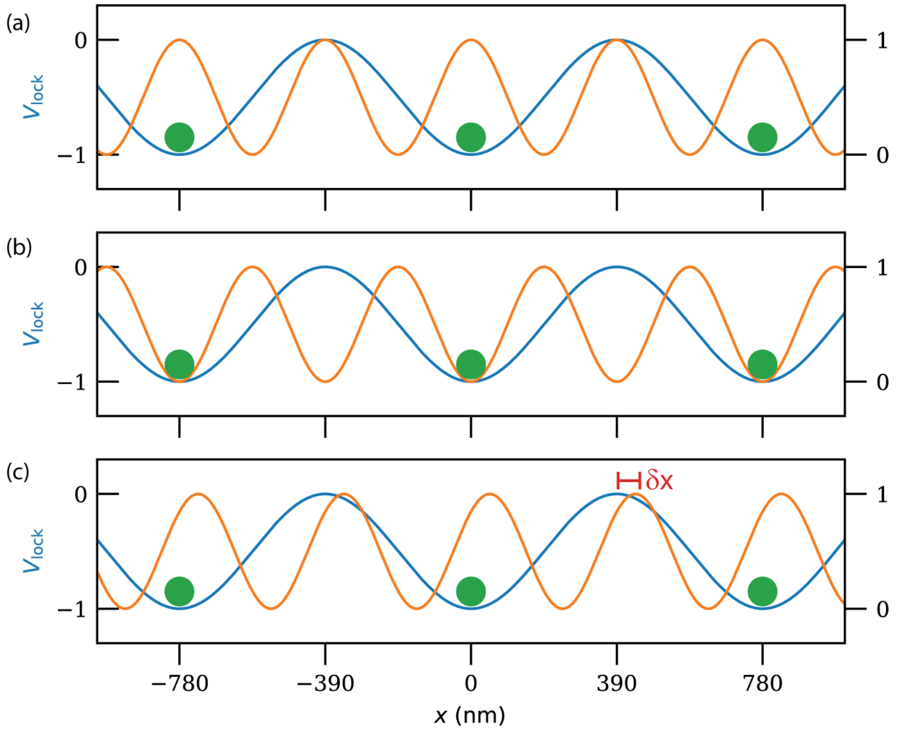

Figure 5.1: Bichromatic cavity mode overlap. Blue: cavity lock light ($\lambda = 1560$ nm) trapping potential V_{lock} in arbitrary units, with atoms (green) at trap minima. Orange: cavity probe ($\lambda = 780$ nm) coupling strength $|g|^2$ in arbitrary units. (a) Desired overlap: probe antinodes aligned with trap minima. (b) Worst-case scenario: zero probe coupling at trap minima. (c) Spatial offset δx between cavity lock and probe modes.

5.1 Bichromatic cavity

Justin Gerber's dissertation [127] provides a lengthy discussion of our bichromatic cavity, including its motivation, technical details about the coatings, and a thorough consideration of how to tune the atom-probe coupling in a one-dimensional lattice formed by the cavity locking light, referred to here as the cavity trap. Briefly, our thinking was as follows: A cavity coated for high reflectivity at both the ^{87}Rb probe wavelength of 780 nm and also its doubled wavelength, 1560 nm, can be tuned to be simultaneously resonant with light at both wavelengths. The 1560 nm light can then be used not only to lock the cavity, but also to trap atoms in an optical lattice that is perfectly registered to the probe standing wave. Atoms trapped at antinodes of the 1560 nm cavity trap will experience identical coupling to the cavity probe, at least over some large region in the center of the cavity where the atoms are trapped. This method is used in several other ^{87}Rb cQED experiments [72, 133], and is also related to the method used in our predecessor cavity experiment E3, which uses an optical lattice wavelength of 845 nm to effect different atom-cavity coupling at neighboring lattice sites [87].

The specific cQED coupling at trap minima depends on how close the cavity probe and lock beams are to the exact wavelength-doubled condition, $\nu_{\text{probe}} = 2\nu_{\text{lock}}$, as well as the reflection phase of each beam on the cavity mirrors. For most cQED experiments, we would desire maximum coupling to the probe, or alignment of the probe and trap antinodes; see Fig. 5.1. The opposite phase registration, with atoms trapped at locations of zero probe-atom coupling, would be found at the next adjacent longitudinal mode of the cavity probe, one free spectral range away. Asymmetric mirror phases might yield some other axial displacement between the probe and lock modes at the center of the cavity; one could work around this by tuning the probe and lock frequencies and moving the atoms away from the center of the cavity to obtain the desired probe coupling.

However, to control the phase overlap between the cavity probe and lock light, we must be able to measure it. In the lab, we initially planned to distinguish between the maximum and minimum coupling conditions, Fig. 5.1(a) and (b), by overlapping the cavity lock light with adjacent longitudinal probe modes and observing a difference in the dispersive cavity shift due to atoms trapped in the cavity locking lattice. As we thought about the fully general problem, though, including possibly asymmetric reflection phases on the cavity mirrors, we realized this might be more complicated—in the meantime, we trapped and imaged single atoms in the tweezer array! And as we learned about fluorescence imaging in the presence of the large excited-state ac Stark shift of the cavity trap light, we realized that we could use single atom imaging to measure the ac Stark shifts of the cavity beams directly, characterize the probe-lock overlap, and come up with an interesting quantum sensing result as well.

Since then, all our work has been done using the tweezers to trap single atoms—we do not rely on the cavity lock light to trap the atoms at a specific position with respect to the cavity probe standing wave. But, still, the local intensity (or intensity gradient) of cavity lock light at the locations of tweezer traps may end up being important, either of use or as a hindrance, due to the strong ac Stark shift on the atomic excited state. This can interfere with atom-light interactions, or it can indeed be used as a tool to shift an atom's resonance in a controlled way. We may also become interested in the local intensity of light at other wavelengths, and in other longitudinal or transverse modes of the cavity. Our ability to map out light fields will be important again when that happens.

5.2 Measurement sensitivity

Our measurement is based on imaging single atoms with near-resonant fluorescence light and converting the detected photon number to the local ac Stark shift, δ_{ac}, through the relation between the atomic scattering rate, Γ_{sc}, and detuning of the imaging light, $\Delta = \omega_L - \omega_0$. In some measurement time τ, with detection efficiency η, we detect an average of

n photons:

$$n = \Gamma_{\text{sc}}\tau\eta = \frac{A}{(\omega_L - \omega_0 - \delta_{\text{ac}})^2} \tag{5.1}$$

The proportionality constant A, a function of atomic parameters, imaging light intensity, exposure time, and detection efficiency, is experimentally obtained by performing a fit to reference data of photon counts versus imaging light detuning, taken in the absence of an optical field under measurement.

Inverting this equation, we obtain $\delta_{\text{ac}} = \omega_L - \omega_0 - \sqrt{A/n}$, and through standard error propagation determine the uncertainty in δ_{ac} due to the uncertainty in n:

$$\text{Var}(\delta_{\text{ac}}) = \left(\frac{\partial \delta_{\text{ac}}}{\partial n}\right)^2 \text{Var}(n) = \frac{1}{4}\frac{A}{n^3}\text{Var}(n) \tag{5.2}$$

This variance is converted to measurement sensitivity S, in units of MHz/$\sqrt{\text{Hz}}$, by dividing it by the measurement rate, $1/\tau$, and taking the square root.

5.2.1 Shot noise limit

The fundamental limit to photodetection noise is the shot noise limit. Plugging $\text{Var}(n) = n$ into Eq. (5.2), we obtain the measurement sensitivity

$$S = \sqrt{\frac{1}{4}\frac{A}{n^2}\tau} = \sqrt{\frac{A}{4(\eta\Gamma_{\text{sc}})^2\tau}} \tag{5.3}$$

The measurement sensitivity is fundamentally limited by the maximum scattering rate of the atom, $\Gamma/2$. However, Eq. (5.1) and the treatment that follows are only valid in the far-detuned, low-saturation regime, where we are limited to a lower scattering rate. We operate in this regime to avoid atom loss and ensure continuous operation of the sensor with simultaneous laser cooling. We observe that the experimental limit of photon flux on the camera is about 1700 photons in 500 ms, occurring at a minimum detuning of the imaging light from the transition's ac-Stark-shifted resonance of $\Delta - \delta_{\text{ac}} = -2\pi \times 30$ MHz. This photodetection rate would yield a shot-noise-limited sensor performance of $2\pi \times 250$ kHz/$\sqrt{\text{Hz}}$.

5.2.2 Photodetection noise

Our measurement is not shot-noise-limited, however. Electronic read noise, background light, and atomic internal dynamics all contribute additional variance to the measured photon count distribution, making the sensor performance worse.

In this section, as I attempt a careful accounting of our photodetection noise, I primarily work in the units reported by our Andor Zyla 2.4 sCMOS camera: analog digital units (ADU), or "counts." The conversion from ADU to photons quoted in the Zyla manual is 0.28; we convert between ADU and photon units to properly account for photon shot noise.

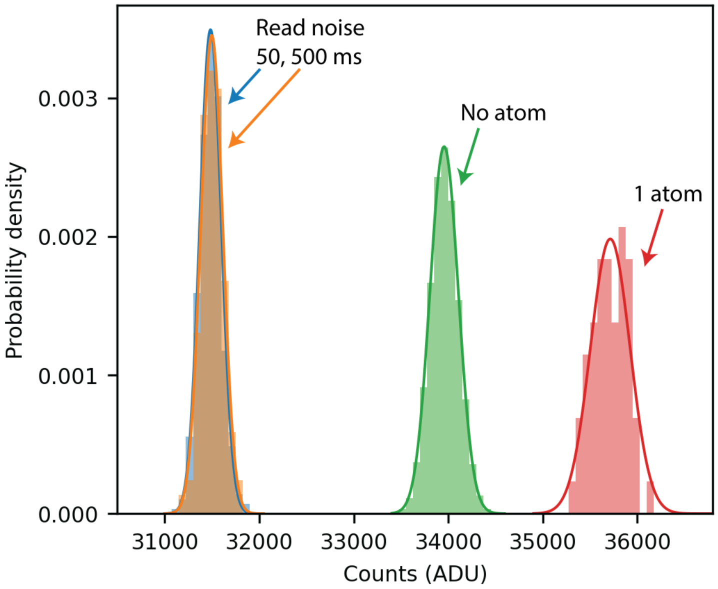

Figure 5.2: Imaging photodetection noise. Blue, orange (overlapping): counts detected during imaging exposures of 50 and 500 ms with the camera's lens cap on. The mean indicates an offset of 105 counts per pixel; the variance represents electronic read noise. Green, red: no-atom and one-atom counts in an imaging exposure of 500 ms. The variance of the no-atom distribution is well-explained by the shot noise of the background light. The one-atom distribution exhibits super-Poissonian noise. All data are counts detected within a ROI of 300 pixels.

Electronic read noise

We measure the electronic read noise by taking repeated camera exposures of 50 and 500 ms with no light on and the lens cap over the camera. The results of the two measurements are identical, indicating that the measured counts are just read noise and not due to background light. In our single-atom imaging, we look at a region of interest of 20×15 pixels around each tweezer position, so the observed count number is the total for 300 pixels.

As shown in Fig. 5.2, the average counts detected in a "dark" exposure of 50 or 500 ms is 31500, or 105 per pixel. The mean is just an offset that can be subtracted. More relevant to us is the width of the distribution, which has a variance due to electronic read noise of $\sigma_{\mathrm{rn}}^2 = 12800$. This seems to indicate a per pixel e^- read noise of 6.5 counts, far exceeding the median level of 0.9 counts/pixel specified in the Zyla manual. This discrepancy may be related to suboptimal configuration of the camera settings and should be investigated further for future work that would benefit from reduced photodetection noise.

Background light

The additional noise due to background light is obtained from "no-atom" images. The average count is higher than the read noise level by 2500, indicating the detection of 700 photons of background light. The variance increases to 22200, due to the Poissonian shot noise of the background light. Note that the comparison is a little confusing with the conversion factor of 0.28 between ADU and photons: photon statistics are Poissonian—$\mathrm{Var}(n) = n$—in units of photons, not ADU!

Adding the additional ADU variance expected from the shot noise of 700 photons, $700/(0.28)^2$, to the measured read noise variance, 12800, yields an expected variance of 21700; we observe 22200. The background light is thus basically Poissonian and well-understood.

Super-Poissonian atomic emission

The photons scattered by the atoms exhibit additional noise above shot noise. Looking specifically at the detected photon counts for an atom imaged at a molasses detuning of $-2\pi \times 54$ MHz, the average count has increased by 4200 ADU counts (roughly 1200 photons), whose shot noise, when added in quadrature to the noise sources we have already discussed, would yield a variance of 27800 ADU counts. Instead, the observed distribution has a variance of 46200.

We attribute the fact that the light collected from the atom has super-Poissonian fluctuations to internal state dynamics of the atom: the illuminated atom can be depumped into the dark $F = 1$ ground state through off-resonant coupling to the $F = 2 \to F' = 2$ transition for a variable amount of time before being repumped back into the bright $F = 2$ ground state to continue scattering light on the $F = 2 \to F' = 3$ transition. Thermal position fluctuations of the atom may be a source of additional noise as well.

We quantify the increased variance using a Fano factor F [140], setting $\mathrm{Var}(n) = Fn$, for the photon number n detected above the reference (no atom) level. From the measured "one-atom" photon number distributions at several measurement settings, including the one shown in Fig. 5.2, we determine a conservative Fano factor of 3.

5.2.3 Actual measurement sensitivity

Electronic read noise, background light, and super-Poissonian noise of the detected atomic fluorescence all contribute to worse sensor performance than the fundamental shot noise limit given in Eq. (5.3), with single-shot measurement sensitivity now given by

$$S = \sqrt{\frac{1}{4}\frac{A}{n^3}\left(\sigma_{\mathrm{rn}}^2 (0.28)^2 + n_{\mathrm{background}} + F n_{\mathrm{atom}}\right)\tau} \tag{5.4}$$

Here, as in Eq. (5.3), n is in units of photons, not ADU, so the read noise variance σ_{rn}^2 is multipled by the squared ADU-photon conversion factor $(0.28)^2$.

At the maximum photodetection rate, where the shot-noise-limited sensor sensitivity would be $2\pi \times 250$ kHz/$\sqrt{\mathrm{Hz}}$, we achieve $2\pi \times 500$ kHz/$\sqrt{\mathrm{Hz}}$.

5.2.4 Sensor speed and dynamic range

Related to the measurement sensitivity are two other important quantities characterizing any sensor: speed and dynamic range. The development of fast scanning probe techniques is motivated by the desire for simultaneously spatially and temporally resolved sensing [141, 142]. However, there is a fundamental tradeoff between measurement sensitivity, quoted in units per $\sqrt{\mathrm{Hz}}$, and speed. The time τ that appears in the expressions for sensitivity given above refers to the exposure time of our fluorescence imaging, and the sensitivity exhibits characteristic scaling with the inverse square root of τ. However, our actual sensor speed is limited by the experimental cycle time. For this work, the atom preparation sequence, consisting of loading a MOT, transferring atoms into an optical dipole trap, optically transporting the atoms into the cavity, and loading the optical tweezers (see Chapter 4), took about 3.5 seconds. The tweezer-trapped atoms were then interrogated in 10 exposures of 500 ms each, at different imaging detunings. Reducing the experimental cycle time would increase the sensor speed at no cost to the measurement sensitivity.

Our consideration of sensor speed came after we took the data in Ref. [53], which were collected in long experimental scans of multiple parameters that were not optimized for speed. To be specific, the data in Ref. [53], Fig. 3 (also included in Appendix A), which shows the spatially resolved scanning probe measurement of the cavity lock light, took about five hours to collect, interspersed through a longer experimental scan of about 20 hours. Each atom was imaged in ten different imaging exposures taken at different imaging detunings, only one of which was ultimately used for the measurement. Optimizing for speed and instead interrogating each atom at the optimal frequency 10 times per iteration, the same quantity of data—between 5 and 40 seconds of averaging time at each tweezer position—could be collected in about 30 minutes, or half that with deterministic tweezer loading.

The dynamic range is also intrinsically related to the measurement sensitivity, by the simple fact that it is difficult to measure signals very precisely over a large amplitude range [6]. For a specific setting of the imaging detuning Δ and exposure time, the dynamic range is bounded by the minimum and maximum photon counts that can be detected, above the photodetection noise floor at large $|\Delta - \delta_{\mathrm{ac}}|$ and below the limit of scattering-induced heating and loss at decreasing $|\Delta - \delta_{\mathrm{ac}}|$. With an exposure time of 500 ms, the measurable range of δ_{ac} is between approximately $\Delta + 2\pi \times 30$ MHz and $\Delta + 2\pi \times 80$ MHz. Decreasing the exposure time would increase the measurement sensitivity, but would also decrease the workable range of $\Delta - \delta_{\mathrm{ac}}$. This range can be adjusted to include a signal of interest by changing the imaging detuning Δ.

A more fundamental limit to the dynamic range of the sensor is reached when the light under measurement begins to interfere with the measurement process in one of three ways. Our imaging requires PG cooling to balance the heating due to Rayleigh scattering of the imaging light, leading to a steady-state temperature; when the Rayleigh scattering of the light under measurement approaches that of the imaging light, the steady-state temperature will increase and result in worse measurement resolution and, eventually, atom loss. The light under measurement can also effect state-dependent light shifts that interfere with PG cooling. We observed increased atom loss when the cavity lock light's scalar ac Stark shift δ_{ac} reached about $2\pi \times 100$ MHz, which may be explained by the corresponding tensor ac Stark shifts and this effect. Finally, the measurement light can exert a force that pulls the atom out of the tweezer, imposing another limit on the measurable field. These limits will be reached at different intensities and in different orders depending on the wavelength of the light being considered, the depth of the tweezer trap, and the parameters of the imaging light and PG cooling.

5.2.5 Thermal broadening

In the above, I have only considered the measurement uncertainty $\mathrm{Var}(\delta_{\mathrm{ac}})$ arising from photodetection noise $\mathrm{Var}(n)$. $\delta_{\mathrm{ac}} = \omega_L - \omega_0 - \sqrt{A/n}$ A more complete treatment would also account for the spectral broadening of the ac Stark shift due to the tweezer trapping light, δ_{twz}, whose average is subtracted from the measured ac Stark shift to obtain δ_{ac} of the cavity field, explicitly included as $\delta_{\mathrm{ac}} = \omega_L - \omega_0 - \delta_{\mathrm{twz}} - \sqrt{A/n}$. For our largest tweezer depth, δ_{twz} is as large as roughly $2\pi \times 40$ MHz, and based on our estimate of the atomic cloud width (see Section 5.3.2 below), we expect that the atoms thermally sample such a shift with a variance of roughly $(2\pi \times 4 \text{ MHz})^2$.

However, the atoms sample the ac Stark shift of the tweezer on their motional timescale on the order of $t \sim 10$ μs, much shorter than the exposure time τ. The contribution of δ_{twz} to the variance of δ_{ac} is thus reduced by a factor of t/τ, to roughly $(2\pi \times 20 \text{ kHz})^2$. This is negligible compared to the photodetection noise.

5.3 Finite measurement contrast

A major part of our result in Ref. [53] is the demonstration of a superresolution measurement, which is not limited by the diffraction limit of our optical imaging system. Rather, the measurement resolution is limited by the thermal extent of the tweezer-trapped atoms, after we correct for a slow drift between the tweezer array and the cavity mode. Here I will explain how we observe and correct the relative drift in data analysis, and discuss the measurement contrast that we ultimately achieve.

5.3.1 Detecting and correcting thermal drift

The axial scans of the cavity lock mode shown in Ref. [53], Fig. 3—reproduced in Appendix A—represent part of a large experimental scan taken over the course of a full day (see Section 5.2.4). On this timescale, we observed that the tweezer positions drift relative to the cavity, resulting in poor contrast of the cavity axial pattern when averaged across the full data set.

We account for this drift by looking at the repeated axial scans in a time-resolved way, breaking the full dataset of 160 measurements at each of 10 axial positions, scanned using

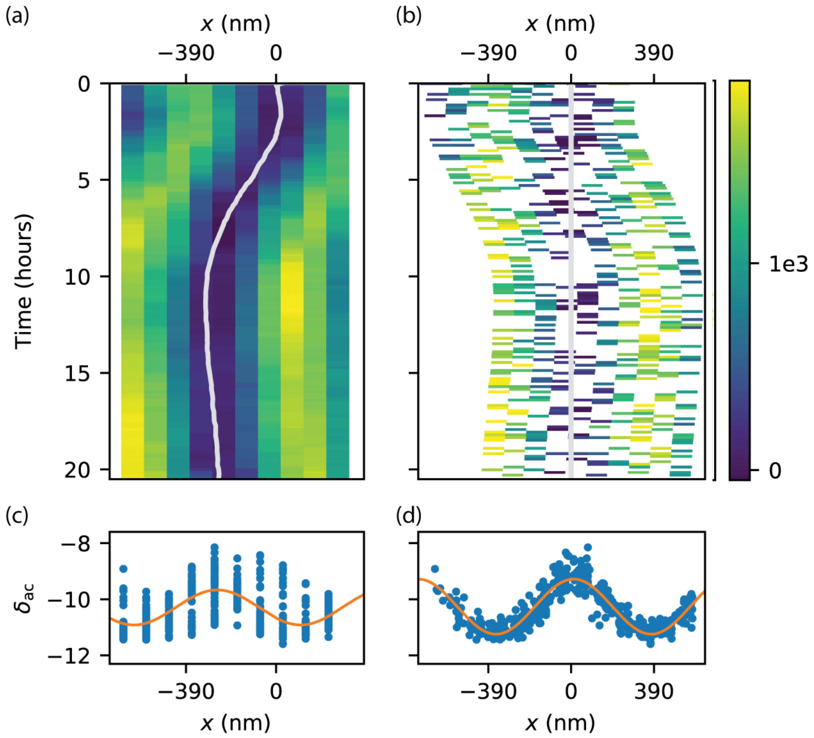

Figure 5.3: Tweezer array and cavity thermal drift. (a) Rolling averages of detected photon counts vs axial position and time. The inferred drift $x(t)$ is overlayed in gray on the photon count colormap. (b) Raw photon counts after correcting the axial drift. (c,d) ac Stark shift determined from photon counts, before and after drift correction.

the mirror piezo, into overlapping subsets of 30 measurements at each position. In the subset averages of the detected photon counts, shown in Fig. 5.3(a), we can clearly see a drift in the axial cavity field oscillation. Fits for the local oscillation phase yield the inferred relative axial drift $x(t)$ between the cavity and tweezer array, shown overlayed in gray on the photon count color map. This is then added as a correction to the position axis for each repetition of the axial scan, yielding the corrected raw data shown in Fig. 5.3(b). Note that our tweezer loading is probabilistic; shots where an atom was not loaded or was lost during the measurement have been removed in data postselection. In Fig. 5.3(c-d), we see the contrast of the observed axial oscillation increase with the drift correction, bringing us to the resolution limit discussed in Ref. [53] and in the next section.

We attribute this drift to thermal drift between the tweezer array and the optical cavity. The system was designed with passive stability in mind, with the objective that generates the tweezer array mounted directly to the vacuum chamber that holds the cavity, rather than to a separate breadboard, to minimize drift; see Fig. 3.10. But the full tweezer optics path and the optical cavity are necessarily quite far apart, and some amount of relative drift is not surprising. Furthermore, both paths contain piezos, on the cavity mirrors and on the piezo-controlled steering mirror that is used to scan the axial tweezer position, which are known to be large sources of drift and nonrepeatability.

The fastest drift that we observe is on the order of roughly 100 nm per hour. Unlike many experimental drifts, it does not settle when the experiment is run in a steady duty cycle,[1] but continues to vary nonmonotonically during experimental runs exceeding 24 hours, with total drifts sometimes exceeding the cavity probe wavelength of 780 nm. This is similar to drift observed in comparable systems: Ref. [128] measures a drift between an optical lattice and addressing beam in a quantum gas microscope exceeding 1.5 μm/hr, and corrects it with feedback on the addressing beam position.

In the work described in this chapter, the drift affects our measurement resolution; in future projects, the relative location of the tweezer array and cavity will affect the cQED coupling strength. The drift must therefore be accounted for in data analysis, investigated further and eliminated, or corrected with feedback, as in Ref. [128], for projects that require controlled cavity coupling with a well-localized tweezer-trapped atom.

5.3.2 Resolution limit

After correcting the thermal phase drift, one of the important quantities that we extract from our axial cavity mode measurements, and assess repeatedly at different experimental conditions, is the contrast $\mathcal{C}$.[2] $\mathcal{C}$ quantifies the measured axial oscillation of the cavity mode, which physically oscillates between zero and some maximum, but is measured to vary between a smaller range, δ_{min} to δ_{max}, due to finite spatial measurement resolution. It is defined as

$$\mathcal{C} = \frac{\delta_{\text{max}} - \delta_{\text{min}}}{\delta_{\text{max}} + \delta_{\text{min}}} \tag{5.5}$$

In our case, $\mathcal{C}$ provides information about the physical state of the scanning probe microscope: specifically, the thermal extent of the tweezer-trapped single-atom "probe," which determines the measurement resolution limit. We assume that over the long imaging exposure time, the fluorescing atom wanders in position within the standing-wave cavity intensity pattern that is being imaged. We model the atom's spatial distribution as a Gaussian with rms width σ and calculate its convolution with the perfect-contrast cavity standing wave with periodicity $d = \pi/k_{\text{lock}}$, yielding the expected measurement contrast

$$\mathcal{C} = e^{-2k_{\text{lock}}^2\sigma^2} \tag{5.6}$$

Note that here I use a one-dimensional treatment, considering only position fluctuation along the cavity axis, where the short length scale of the cavity mode's spatial features is comparable to the length scale of atomic motion within the tweezer trap. Orthogonal to

---

[1] It appears to in Fig. 5.3, but this is not consistent over other datasets.

[2] Not to be confused with the cavity cooperativity C, which has no bearing on this work.

the cavity axis, the cavity mode varies over the much longer length scale of the mode waist, on the order of 20 μm, and atomic motion in these dimensions, i.e. both along the optical tweezer axis and also along one of the tightly focused directions of the tweezer, negligibly affects the measurement.

The best axial measurement contrast that we observe, $\mathcal{C} = 0.47$, corresponds to an atomic spatial distribution with $\sigma = 150$ nm. Based on our estimated tweezer waist of 750(50) nm and trap depth of $h \times 30(2)$ MHz for these data, this spatial distribution corresponds to an atomic temperature of roughly 200 μK [143]. Such a comparison is limited in its use, however, as the atom under measurement, continually absorbing and emitting photons in optical molasses, is not well-described by an equilibrium state at some temperature. An independent "release and recapture" single-atom temperature measure [144] might provide an interesting comparison.

We obtain the best measurement contrast for the tweezer farthest from the center of the cavity, where the cavity lock light is the least intense. The difference in estimated atom width cannot be explained by differences in the tweezers, which are uniform to within 10% across the array. Instead, we believe that where the cavity lock light is more intense, the atomic temperature is higher, due to state-dependent (tensor) shifts in the excited state manifold that interfere with polarization-gradient cooling. For even higher cavity trap intensities, we see increased atom loss and systematically low photon counts at the cavity lock antinodes, further corroborating this theory.

5.4 Cavity probe measurement

The final result presented in Ref. [53] is the characterization of cavity probe mode through a "force sensing" measurement, whereby the cavity probe is detected through its distortion of the cavity lock light measurement. Note that for our cQED work, the probe is tuned to be near the D_2 $F = 2 \rightarrow F' = 3$ transition, at a wavelength of 780 nm. Here, the probe light is detuned by $2\pi \times 400$ GHz from the transition frequency, at a wavelength of 781 nm, but it is generated by the same probe laser, described in Section 3.1.3.

In the paper, we describe three qualitative changes to the measured cavity lock ac Stark shift in the presence of cavity probe light: an average ac Stark shift up, an increase in contrast due to the probe's additional confining potential, and a phase shift of the axial oscillation due to an axial offset between the two modes. We also fit the data to a numerical model that includes all of these effects, which allows us to quantitatively determine the axial displacement between the two modes. I describe the model below.

5.4.1 The model

The one-dimensional numerical model begins with the intensity distributions along the cavity axis of cavity lock and probe standing waves, with axial displacement δx as depicted in Fig. 5.4(a), and the tweezer trap with waist w, centered at position x_{twz}:

$$\begin{aligned} I_{\mathrm{lock}}(x) &\propto \cos^2\left(k_{\mathrm{lock}}x\right) \\ I_{\mathrm{probe}}(x) &\propto \cos^2\left(k_{\mathrm{probe}}(x-\delta x)\right) \\ I_{\mathrm{twz}}(x) &\propto \exp\left(-2(x-x_{\mathrm{twz}})^2/w^2\right) \end{aligned} \tag{5.7}$$

Each of these effects an ac Stark shift on the D_2 $F=2 \rightarrow F'=3$ imaging transition, given by

$$\delta(x) = -(2\hbar c\epsilon_0)^{-1}[\alpha_{\mathrm{e}}(\lambda)-\alpha_{\mathrm{g}}(\lambda)]I(x) \tag{5.8}$$

where $\alpha_{\mathrm{g,e}}$ are the scalar dynamical electric polarizabilities of the $5S_{1/2}$ $F=2$ ground and $5P_{3/2}$ $F'=3$ excited states.

With $I_{\mathrm{probe}}=0$, $I_{\mathrm{lock}}(x)$ is obtained simply by measuring δ_{ac} at different tweezer positions x_{twz} and subtracting δ_{twz} measured in the absence of cavity locking light. As discussed in Section 5.3.2, the expected measurement result $\tilde{\delta}$ is the convolution of that atomic distribution at each x_{twz} with δ_{lock}. Since $\alpha_g(\lambda_{\mathrm{lock}}) \ll \alpha_e(\lambda_{\mathrm{lock}})$, the cavity locking light at the intensity used for this measurement only negligibly modifies the tweezer potential, and the atomic distribution basically does not change with tweezer position; see Fig. 5.4(b). $\tilde{\delta}(x)$ is thus just a lower contrast version of the true $\delta(x)$ sinusoid; Fig. 5.4(c).

During the I_{probe} measurement, however, the atom cannot be thought of as sitting in the bottom of the tweezer trap as it samples different positions along the probe test pattern; the atomic distribution is distorted differently at different x_{twz} along the cavity probe standing wave. We calculate the trapping potential of each beam, given by the ground state shift

$$V(x) = -(2\hbar c\epsilon_0)^{-1}\alpha_{\mathrm{g}}(\lambda)I(x) \tag{5.9}$$

and at each x_{twz}, model the atomic spatial distribution using the Boltzmann factor at equilibrium temperature T [145]:

$$n(x) \propto \exp(V_{\mathrm{tot}}(x)/k_B T) \tag{5.10}$$

as shown in Fig. 5.4(d). Accounting for nonequilibrium effects in the atomic spatial distribution is beyond the scope of this work.

The convolution of the atomic distribution calculated at each tweezer position with the total ac Stark shift yields our expected measurement result

$$\tilde{\delta}(x_{\mathrm{twz}}) = \int \delta_{\mathrm{tot}}(x)n(x)dx \tag{5.11}$$

The numerical model of $\tilde{\delta}(x_{\mathrm{twz}})$, shown with $\delta_{\mathrm{tot}}(x)$ for comparison in Fig. 5.4(e), is the fit function used in Ref. [53], Fig. 4(b); see Appendix A.

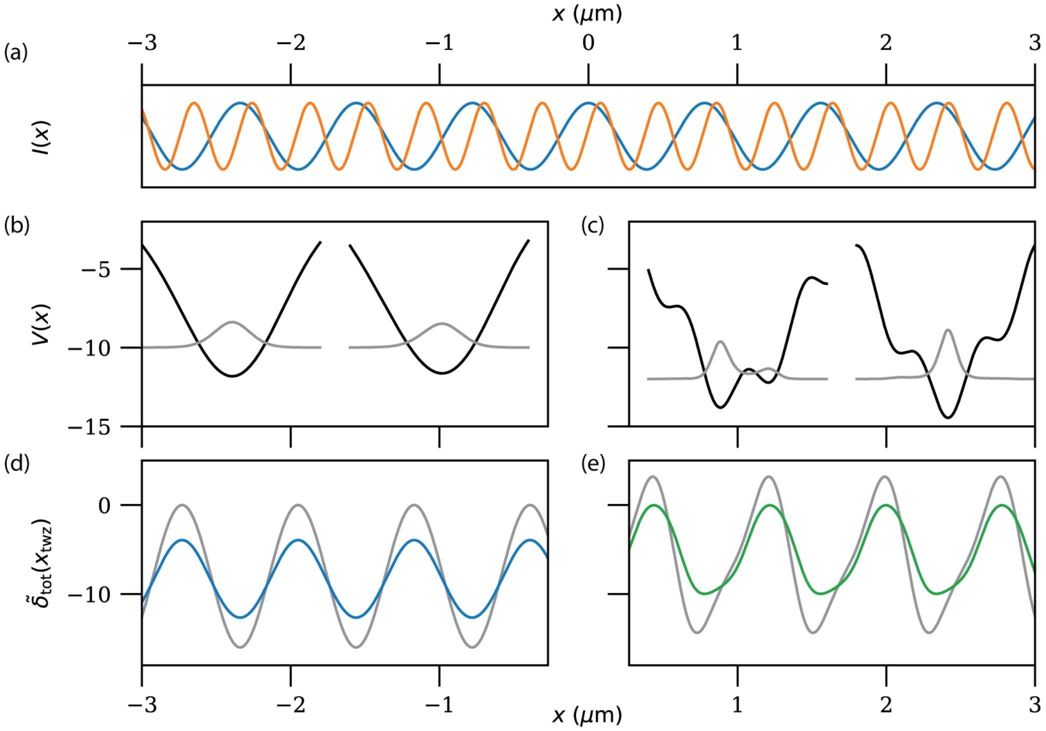

Figure 5.4: Force sensing fit function. (a) Cavity lock (blue) and probe (orange) intensity (arbitrary units) with an axial displacement between the two standing waves. (b,c) Total trapping potential (black) and corresponding atomic thermal distribution (gray) at different tweezer locations in the absence (b) and presence (c) of cavity probe light. Cavity probe light corrugates the tweezer trap potential, and narrows and shifts the atomic distribution. (d,e) Actual (gray) and measured $\delta_{\rm ac}$ (prediction) for the cavity lock light only (blue) and cavity lock and probe light (green), accounting for the probe's distortion of the atom's thermal spatial distribution. This model is used to fit the data in Ref. [53], Fig. 4(b).

5.4.2 Fitting the data

The numerical model of $\tilde{\delta}$ described above is parametrized by the atomic temperature, tweezer intensity, cavity lock intensity, cavity probe intensity, and axial displacement between the cavity probe and lock modes. The first three are determined from data taken in the absence of cavity probe light and assumed to be the same in the data taken with the probe. That leaves the cavity probe intensity and axial displacement as the free parameters of the fit, yielding an axially averaged probe ac Stark shift of $2\pi \times 2.3(1)$ MHz, in agreement with the average value reported in Ref. [53], Fig. 4(c), and relative displacement between the cavity probe and lock light of 50(5) nm; see Appendix A.

5.5 Experimentally relevant takeaways

The work described above and in Ref. [53], the first significant project undertaken on our new apparatus, reveals a lot about our system that will be relevant for all future work on E6. First, from the measurement of the cavity probe mode waist and Eq. (2.11), we determine the maximum cavity coupling strength $2\pi \times 2.7(4)$ MHz for an atom in the stretched $|F = 2, m_F = \pm 2\rangle$ state located at the antinode of a cavity probe mode with the corresponding circular polarization. On the other hand, we learn from the finite measurement contrast that the tweezer-trapped atoms axially average the probe mode almost completely, resulting in reduced effective cavity cooperativity; this is discussed more in Chapter 6. Stronger axial confinement or improved cooling is required to achieve our theoretical maximum cavity coupling with atoms well-localized at the cavity probe antinodes.

The large ac Stark shift of the ^{87}Rb D_2 excited state due to the 1560 nm cavity lock light is ideal for the measurement described here, but it is somewhat inconvenient for cQED applications, where the cavity-atom detuning must be carefully controlled. Going forward, since we are not using the cavity lock light for trapping, we lock to a TEM_{01} mode of the 1560 nm light, placing the atoms in the dark node where the cavity lock ac Stark shift can be ignored; see Section 6.2.1.

The observation of drift between the tweezer array and cavity provides an important benchmark of the stability of our system; this will likely be highly relevant to future work requiring controlled atom-cavity coupling, and may require feedback to correct. Of course, this will only be necessary after improved atom localization is achieved, as the axial position of an atom that averages a full half-wavelength of the cavity probe mode need not be stable.

Finally, the axial measurement of the cavity lock light provides a nice calibration of the fluorescence imaging magnification, using the standing wave periodicity of 780 nm as a very accurate ruler. Repeating the ac Stark shift measurement with a standing wave transverse to the cavity would enable separate characterizations of the imaging system along two axes. A more complete *in situ* characterization of the single atom imaging system done in this way might enable the measurement and correction of imaging aberrations, which could be useful for more demanding imaging and addressing applications down the line.

Chapter 6

Cavity measurement

This chapter discusses our published experimental work on performing a mid-circuit cavity measurement within a coherent neutral atom array, published in Ref. [54] and provided in Appendix B. The text below presents additional material and does not reproduce the content of that published work.

In this chapter, I will discuss our first cQED result: using the cavity to facilitate state detection of one atom in a two-tweezer array, while preserving the second atom's coherence. This work, published in Ref. [54], represents our first demonstration of the scientific potential of an integrated tweezer array cQED system, with the novel realization of a mid-circuit measurement. Ref. [54] is included in Appendix B.

In the context of the rapid development of tweezer array systems, this result highlights what cQED can add to their already impressive capabilities. Rydberg-state-mediated interactions in defect-free arrays of arbitrary geometry [29, 30] enable large-scale quantum simulation of ground states [146, 147] and dynamics [148], as well as entanglement generation for quantum gates [33, 93] and for metrology [149, 150]. However, these systems rely on global free-space imaging for state readout, which defines the end of the experiment. Quantum error-correcting schemes for computation and metrology, as well as measurement-based quantum computing, require mid-circuit measurement of a single atom at a time [98–102].

Our mid-circuit measurement draws on the rich literature of single-atom cavity measurement [79, 89, 96, 97], with a particular focus on the speed, fidelity, and locality required of a mid-circuit measurement. We specifically consider a system that chooses to store the quantum state in long-lived internal states of the atom. For ^{87}Rb, these are the ground-state $F = 1$ and $F = 2$ hyperfine states, with the $F = 2$ selected as the "bright" cavity-coupled state by the cavity probe frequency, near the $F = 2 \rightarrow F' = 3$ transition. We introduce a probe-repump-probe sequence to remove the ambiguity of measuring "not $F = 2$" in a single probe interval, distinguishing an initially dark $F = 1$ atom from no atom. In a Rydberg system, this would allow one to detect the loss of an atom that was mistakenly left in a Rydberg state during a gate operation, or that underwent a transition to another state in an atom with many metastable states.

Ref. [54] presents the highest single-atom measurement fidelities we achieve for atoms in the $F = 1$ and $F = 2$ manifolds, at optimized measurement conditions for fluorescence and transmission detection. We look at the trade-off between fidelity and speed for single atom measurements, pushing for fidelity above that required for error-correcting schemes [151–153] and total measurement duration within the coherence lifetime of the rest of the array. Our two-atom Ramsey experiment, presented as a very simple quantum circuit, demonstrates that the quantum coherence of one atom persists after the measurement of another: a mid-circuit measurement.

Here, I provide information not included in Ref. [54] about the single-probe detection of an atom in the $F = 2$ manifold versus not. I describe the theoretical treatment of our measurements, including the low-saturation regime and beyond; discuss the optimization of our measurement conditions; and present some interesting physics that we observed along the way. I conclude with a brief consideration of some extensions to this work.

6.1 Cavity measurement theory

I follow the treatments described in Refs. [89, 96, 154] for this discussion of the theory describing cavity measurement. Note that there are some differences in our notation and definitions of quantities like κ and C.

In a simplified approximation, our system can be described by the Jaynes-Cummings Hamiltonian, introduced in Chapter 2, with additional atomic and cavity driving terms:

$$\begin{aligned}\mathcal{H}/\hbar =&\omega_a\sigma^+\sigma^- + \omega_c a^\dagger a + g(a\sigma^+ + a^\dagger\sigma^-)\\ &+ \frac{1}{2}\left(\Omega_a e^{-i\omega_L t}\sigma^+ + \Omega_a^* e^{i\omega_L t}\sigma^-\right)\\ &+ \frac{1}{2}\left(\Omega_c e^{-i\omega_L t}a^\dagger + \Omega_c^* e^{i\omega_L t}a\right)\end{aligned} \tag{6.1}$$

Here, the two atomic levels included in our simplified model are the cavity-coupled $5S_{1/2}$ $F = 2$ and $5P_{3/2}$ $F' = 3$ states.

The drive terms, with strength Ω_a and Ω_c, describe the fluorescence and transmission probe light, with laser frequency ω_L, which are coherent laser beams impinging on the atom directly (Ω_a) and on the cavity input mirror (Ω_c). Here I am working in the rotating wave approximation and have separated out the rotating terms from the counter-rotating terms. For near-resonant driving of an atom with an electric field that is not of the scale of the internal electric field within an atom, the counter-rotating terms can typically be set aside.

In a fully general treatment, one might want to include a detuning between the fluorescence and transmission drive frequencies. However, we only use one drive at a time, so we describe both with ω_L. In a frame rotating at this drive frequency, the Hamiltonian becomes

$$\begin{aligned}\mathcal{H}/\hbar =&-\Delta_{\mathrm{pa}}\sigma^+\sigma^- - \Delta_{\mathrm{pc}}a^\dagger a + g(a\sigma^+ + a^\dagger\sigma^-)\\ &+ \frac{1}{2}\left(\Omega_a\sigma^+ + \Omega_a^*\sigma^-\right) + \frac{1}{2}\left(\Omega_c a^\dagger + \Omega_c^* a\right)\end{aligned} \tag{6.2}$$

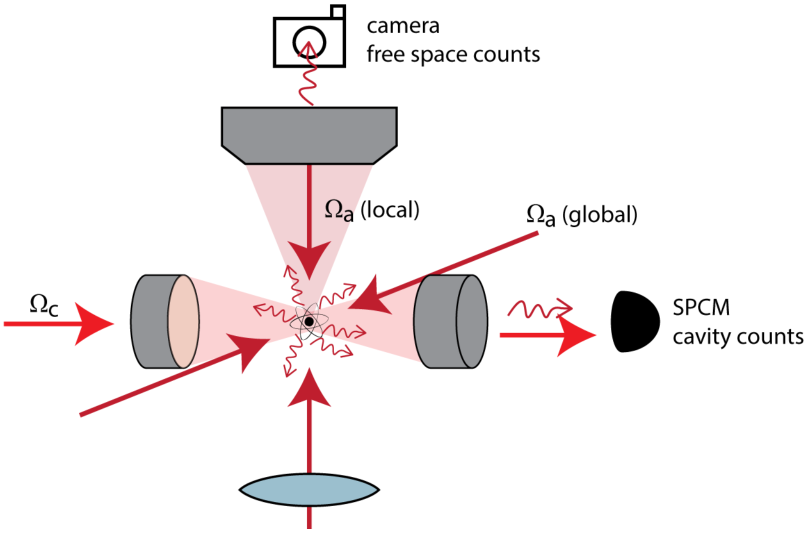

Figure 6.1: Cavity measurement schematic. An atom trapped in a cavity is probed with fluorescence probe light (Ω_a) or transmission probe light (Ω_c). Photons leaking out of the cavity, from atomic fluorescence or cavity transmission, are detected on a single photon counting module. Atomic emission into free space can be detected through an objective when the atom is illuminated with global fluorescence probe light from the side; for local cavity detection, the objective and a lens below the cavity with moderate NA are used instead to illuminate the atom in the center of the cavity with tightly focused fluorescence probe light.

where $\Delta_{\rm pa} = \omega_L - \omega_a$ is the detuning of the probe laser from the atomic transition frequency, and $\Delta_{\rm pc} = \omega_L - \omega_c$ is the detuning of the probe from cavity resonance. In the lab, we prefer to parameterize the relative detunings between the atomic transition, cavity resonance, and probe laser in terms of the cavity-atom detuning $\Delta_{\rm ca} = \omega_c - \omega_a = \Delta_{\rm pa} - \Delta_{\rm pc}$, and the probe-cavity detuning $\Delta_{\rm pc}$, but in this theory section I'll use $\Delta_{\rm pa}$ and $\Delta_{\rm pc}$.

Finally, we consider two decay channels: cavity photon leakage, described by the cavity photon annihilation operator a and rate κ, and atomic excited state decay, described by the atomic operator σ_- and rate Γ.

6.1.1 Low-saturation limit: analytic solution

Using the master equation or Heisenberg-Langevin equation, we obtain equations of motion for the system. We consider dissipation arising from coupling between the system and environment of the form $SR^\dagger + h.c.$, in terms of some system operator S and reservoir operator R, with associated decay rate γ. The time evolution of the expectation value of an operator A is then given by

$$\frac{d}{dt}\langle \hat{A}\rangle = \frac{i}{\hbar}\langle[\hat{H},\hat{A}]\rangle + \frac{\gamma}{2}\big(2\langle \hat{S}^\dagger \hat{A}\hat{S}\rangle - \langle \hat{A}\hat{S}^\dagger \hat{S}\rangle - \langle \hat{S}^\dagger \hat{S}\hat{A}\rangle\big) \tag{6.3}$$

We plug in a and σ^- for S, with associated rates κ and Γ, and obtain these equations of motion for the expectation values of the cavity and atomic operators:

$$\langle \dot{a}\rangle = i(\Delta_{\mathrm{pc}}\langle a\rangle - g\langle\sigma^-\rangle + \Omega_c) - \kappa/2\langle a\rangle \tag{6.4a}$$

$$\langle \dot{\sigma}^-\rangle = i(\Delta_{\mathrm{pa}}\langle\sigma^-\rangle + g\langle a\sigma_z\rangle + \Omega_a) - \Gamma/2\langle\sigma^-\rangle \tag{6.4b}$$

$$\langle \dot{\sigma}_z\rangle = i\left(2g\langle a^\dagger\sigma^- - a\sigma^+\rangle - 2\Omega_a^*\langle\sigma^-\rangle + 2\Omega_a\langle\sigma^+\rangle\right) - \Gamma\langle\sigma^+\sigma^-\rangle \tag{6.4c}$$

In general, this system of nonlinear differential equations is not solvable. However, the system can be linearized to analyze the weak saturation limit by treating the two-level atom as the lowest states of a harmonic oscillator. In particular, we replace the pseudospin operators $\sigma^\pm$ and associated algebra $[\sigma^+,\sigma^-] = \sigma_z$ with the harmonic oscillator operators and commutation relation $[\sigma^\dagger,\sigma] = -1$. Eq. (6.4) now becomes

$$\langle \dot{a}\rangle = i(\Delta_{\mathrm{pc}}\langle a\rangle - g\langle\sigma\rangle + \Omega_c) - \kappa/2\langle a\rangle \tag{6.5a}$$

$$\langle \dot{\sigma}\rangle = i(\Delta_{\mathrm{pa}}\langle\sigma\rangle - g\langle a\rangle + \Omega_a) - \Gamma/2\langle\sigma\rangle \tag{6.5b}$$

For convenience in notation, we introduce complex detunings $\tilde{\Delta}_{\mathrm{c}} = \Delta_{\mathrm{pc}} + i\kappa/2$ and $\tilde{\Delta}_{\mathrm{a}} = \Delta_{\mathrm{pa}} + i\Gamma/2$, and our equations of motion become:

$$\langle \dot{a}\rangle = i\tilde{\Delta}_c\left(\langle a\rangle - \frac{g}{\tilde{\Delta}_c}\langle\sigma\rangle + \frac{\Omega_c}{\tilde{\Delta}_c}\right) \tag{6.6a}$$

$$\langle \dot{\sigma}\rangle = i\tilde{\Delta}_a\left(\langle\sigma\rangle - \frac{g}{\tilde{\Delta}_a}\langle a\rangle + \frac{\Omega_a}{\tilde{\Delta}_a}\right) \tag{6.6b}$$

We introduce one more helpful parameter: a generalized single-atom cavity cooperativity factor $\tilde{C}$, defined as [89]

$$\tilde{C} = \frac{g^2}{(\kappa/2 - i\Delta_{\mathrm{pc}})(\Gamma/2 - i\Delta_{\mathrm{pa}})} = \frac{g^2}{\tilde{\Delta}_c\tilde{\Delta}_a} \tag{6.7}$$

which for zero-detuning is just $C = 4g^2/\kappa\Gamma$. Now we solve for the steady-state solutions of Eq. (6.6) by setting $\langle\dot{a}\rangle = \langle\dot{\sigma}\rangle = 0$ and obtain

$$\langle a\rangle = -\frac{1}{\tilde{C}+1}\left(\frac{\Omega_c}{\tilde{\Delta}_c} + \frac{g\Omega_a}{\tilde{\Delta}_a\tilde{\Delta}_c}\right) \tag{6.8a}$$

$$\langle\sigma\rangle = -\frac{1}{\tilde{C}+1}\left(\frac{\Omega_a}{\tilde{\Delta}_a} + \frac{g\Omega_c}{\tilde{\Delta}_a\tilde{\Delta}_c}\right) \tag{6.8b}$$

From these, we immediately write steady-state atomic excited state population $P_e = |\langle\sigma\rangle|^2$ and cavity photon number $N_{\text{cav}} = |\langle a\rangle|^2$:

$$P_e = \frac{1}{|1+\tilde{C}|^2}\left|\frac{\Omega_a}{\tilde{\Delta}_a} + \frac{g\Omega_c}{\tilde{\Delta}_a\tilde{\Delta}_c}\right|^2 \tag{6.9a}$$

$$N_{\text{cav}} = \frac{1}{|1+\tilde{C}|^2}\left|\frac{\Omega_c}{\tilde{\Delta}_c} + \frac{g\Omega_a}{\tilde{\Delta}_a\tilde{\Delta}_c}\right|^2 \tag{6.9b}$$

6.1.2 Beyond low-saturation: mean-field and numerics

Eq. (6.9) holds for weak drive strength and low atomic saturation, the primary regime that has been explored experimentally in other work [89, 96]. In this regime, where equations of motion are exactly solvable, we can see the cavity scattering (for fluorescence) and transmission reduction (for transmission) that enable cavity detection. However, the low-saturation regime falls short of describing *fast* cavity measurement. To collect photons faster, we must drive the system harder. This is clear from Eq. (6.9)(b), where N_{cav} increases with both Ω_a and Ω_c. But eventually, increasing the drive strength violates our low-saturation assumption, and we must change the model.

The intermediate-drive-strength regime can be treated by returning to Eq. (6.4) and making a mean-field approximation. Terms like $\langle a^\dagger\sigma^-\rangle$ are replaced with $\langle a^\dagger\rangle\langle\sigma^-\rangle$, neglecting correlations between the atomic and cavity states. The equations of motion can then be solved exactly for the separate cases of the fluorescence measurement ($\Omega_c = 0$) and the transmission measurement ($\Omega_t = 0$). This treatment, worked out for us by Leon Lu, extends the range of drive strengths for which the cavity measurement can be solved analytically and indicates a maximum cavity scattering rate of g^2/κ for fluorescence detection and a similar saturation of the transmission reduction and optimal drive strength for transmission detection at intermediate drive strengths.

The system can be studied for arbitrary drive strengths by simulating the dynamics numerically instead. I did this using QuTiP [155], a Python package that provides functions for solving the master equation, performing stochastic wavefunction analysis, and much more. I defined the system as the tensor product of a two-level atom and cavity Fock states up to some $|n_{max}\rangle$. Then I provided the Hamiltonian in Eq. (6.2) and collapse operators $\sqrt{\kappa}a$ and $\sqrt{\Gamma}\sigma^-$, and QuTiP handled the rest.[1] The results of these simulations for the cavity fluorescence measurement ($\Omega_c = 0$) are shown in Fig. 6.6 and discussed in Section 6.3.5. The basic simulation code is included in Appendix C.

---

[1] Though it took a bit of time to learn how to use QuTiP, I highly recommend it. I only scratched the surface of what it can do, and did so after wasting a lot of time simulating quantum systems with my own very clunky and vastly inferior code. Give it a try!

6.2 Experimental configuration

In the lab, as we transitioned from the ac Stark shift microscopy project described in Chapter 5 to this work, we needed to make a few experimental changes. First, we changed our fluorescence imaging parameters from those used in the ac Stark shift microscopy project, to operate at a closer detuning of the imaging light and shorter exposure times of $50 - 100$ ms, more similar to the imaging parameters used in other tweezer array experiments [29, 30]. We also built the cavity detection system, described in detail in Section 3.3. This involved deconstructing the heterodyne detection system described in Justin Gerber's thesis [127] to replace it with a single photon counting module. Future work on this apparatus might benefit from returning to heterodyne detection. To facilitate local cavity measurement, we built the upper and lower probe paths for local detection, described in Section 6.3.4 and Chapter 3. Finally, we changed the cavity lock and cavity resonance conditions, as described below.

6.2.1 Locking to a TEM_{01} cavity mode

After the ac Stark shift measurement project described in Chapter 5, we decided not to burden ourselves with tracking and controlling the position of single atoms within the 1560-nm cavity lattice. Instead, we locked the cavity to a TEM_{01} mode of the 1560-nm light, with the atoms trapped in its horizontal dark plane. To facilitate this change, a knife edge, oriented horizontally, was added to the cavity input path; see Fig. 6.2. This improves mode matching of the input cavity lock light to the TEM_{01} mode over the TEM_{10} and TEM_{00} modes, and spatially filters the light again on its reflection from the cavity back to the PDH photodiode, generating a clean lock signal.

The atoms were aligned to the dark plane of the cavity locking light using techniques we developed in the scanning probe project: we performed fluorescence imaging of the tweezer array while adjusting the z position of the objective's vertical translation stage—see Fig. 3.10 for a schematic of this setup. Above and below the dark plane, the cavity lock light shifts the fluorescence imaging light closer to resonance, resulting in atom loss. The loss probability as a function of z position indicates a clear minimum when the atoms are best localized to the dark TEM_{01} node, pictured in Fig. 6.2. The width of the node of a Hermite-Gauss TEM_{01} mode is comparable to half the beam waist of the TEM_{00} mode, as shown in Fig. 6.2(b) for the cavity lock TEM_{00} mode waist of about 26 μm measured in Ref. [53]. The data in Fig. 6.2(c), taken with six tweezers spanning a horizontal distance of about 25 μm, indicate that the imaging survival rate exceeds 90% within a vertical range of two micrometers of the mode center, for the large cavity lock power used for this measurement. Under normal experimental operation, the cavity lock power is lower by a factor of more than 10, and the ac Stark shift from the cavity lock light can safely be ignored.

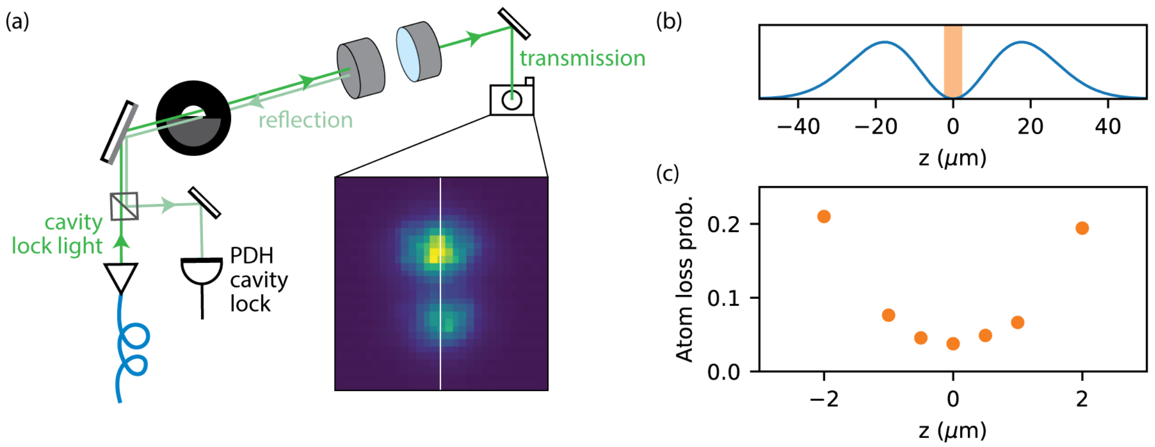

Figure 6.2: Locking to a TEM_{01} mode. (a) For our cavity measurement work, the cavity is locked to a TEM_{01} mode of the cavity lock light; see also Fig. 3.11. (b) Calculated intensity (arbitrary units) vs vertical position along the center of the cavity lock mode, indicated by the gray line in (a). The orange region indicates the range of the measurement in (c), which shows the atom loss probability vs the tweezer focal plane, tuned using the z position of the objective. The minimum of the atom loss probability indicates the node of the cavity lock mode, where we place the atoms for this work.

6.2.2 Tuning cavity and probe to atomic resonance

In Chapter 5, the cavity was tuned to be resonant with the probe light at a detuning of roughly $2\pi \times 400$ GHz from atomic resonance. For the cavity measurement work described here, we operate much closer to atomic resonance, with the cavity frequency tuned to be $2\pi \times (10 - 35)$ MHz below atomic resonance for the fluorescence measurement and roughly on atomic resonance for the transmission measurement. The probe is set to be within a few κ of the cavity resonance.

To find a cavity resonance near atomic resonance, we first coupled our imaging molasses light, derived from the 3D MOT cooling laser, into the cavity probe path, using a fiber-to-fiber coupler. The cavity length was adjusted, using the frequency of the EOM in the ULE lock of the cavity locking light, to find a simultaneous resonance of the locking light (now a TEM_{01} mode, as discussed above) with the molasses light, at a detuning of $2\pi \times 35$ MHz from atomic resonance.

Then the cavity probe light, derived from the narrow cavity probe ECDL, was returned to its usual path and tuned using the wavemeter to be within a few gigahertz of atomic resonance. The frequency of the EOM in the probe's ULE lock was used to bring the probe light to the nearest cavity resonance and $2\pi \times 35$ MHz detuning from atomic resonance. Transferring the molasses light frequency to the probe laser frequency using the science cavity lock was an easy way to bring the probe light to atomic resonance without building a setup to beat the molasses and probe light directly or using another vapor cell; all we did was plug and unplug fibers to take light to the science cavity.

From this known starting point of $2\pi \times 35$ MHz detuned from the $F = 2 \rightarrow F' = 3$ transition—including the ac Stark shift effected by the tweezer trapping light, measured according to the method described in Chapter 5—we could adjust Δ_{ca} by any amount δ by adding $\delta/2$ to the cavity lock EOM, [2] and bring the probe to the new cavity resonance by adding δ to its EOM. We used this method to go back and forth easily between different fluorescence probe detunings around $-2\pi \times (10 - 35)$ MHz and the transmission probe detuning of 0.

6.3 Cavity fluorescence

In the lab, we started our attempt at the cavity fluorescence measurement by just trying the simplest thing: doing regular fluorescence imaging, illuminating the atoms with global molasses light from the side, but now with the cavity tuned to the molasses frequency. As the atom scattered photons into free space—some small fraction of which were detected on the camera—the atom would also scatter into the resonant cavity, and those photons would come pouring out of the cavity onto our detector.

On our first attempt, we didn't change our experimental sequence at all, except to add a trigger for the SPCM at the beginning of the fluorescence imaging exposure. We loaded ten tweezers probabilistically and just compared cavity counts with and without atoms, toggled by turning the MOT on and off, without any data postselection. We detected about 3 photons in 5 ms on average when there were no atoms, and 7 when there were atoms. This was of course a much smaller signal than we expected, but it was a signal! It turned out that the SPCM was aligned improperly, detecting a back-reflection of the cavity light. After realignment of the detection optics, including the addition of an iris—see Section 3.3.3—the true signal appeared, and we began our study of cavity fluorescence detection.

6.3.1 Cavity photon time traces

In Fig. 6.3, I present data from our initial investigation of cavity fluorescence detection and free-space fluorescence imaging. The experimental sequence is schematically indicated in Fig. 6.3(a). After atom preparation and transport to the science chamber (see Chapter 4), a fluorescence image is taken to determine tweezer occupation. During this first image, the cavity is tuned to be a few megahertz blue-detuned of the fluorescence probe light, which is about $2\pi \times 35$ MHz red-detuned of atomic resonance. This ensures that cavity effects—in particular, cavity heating, discussed in Section 6.3.3, which would result in atom loss—do not interfere with the image, used for data postselection.

After state preparation in the $F = 2$ manifold (see Section 4.5.1), the cavity frequency is ramped over 1.5 ms to a variable detuning Δ_{pc} from the probe frequency for near-resonant

---

[2] The factor of 1/2 is due to the twice-wavelength condition of the cavity locking light relative to the probe; see Sections 3.3.1 and 5.1.

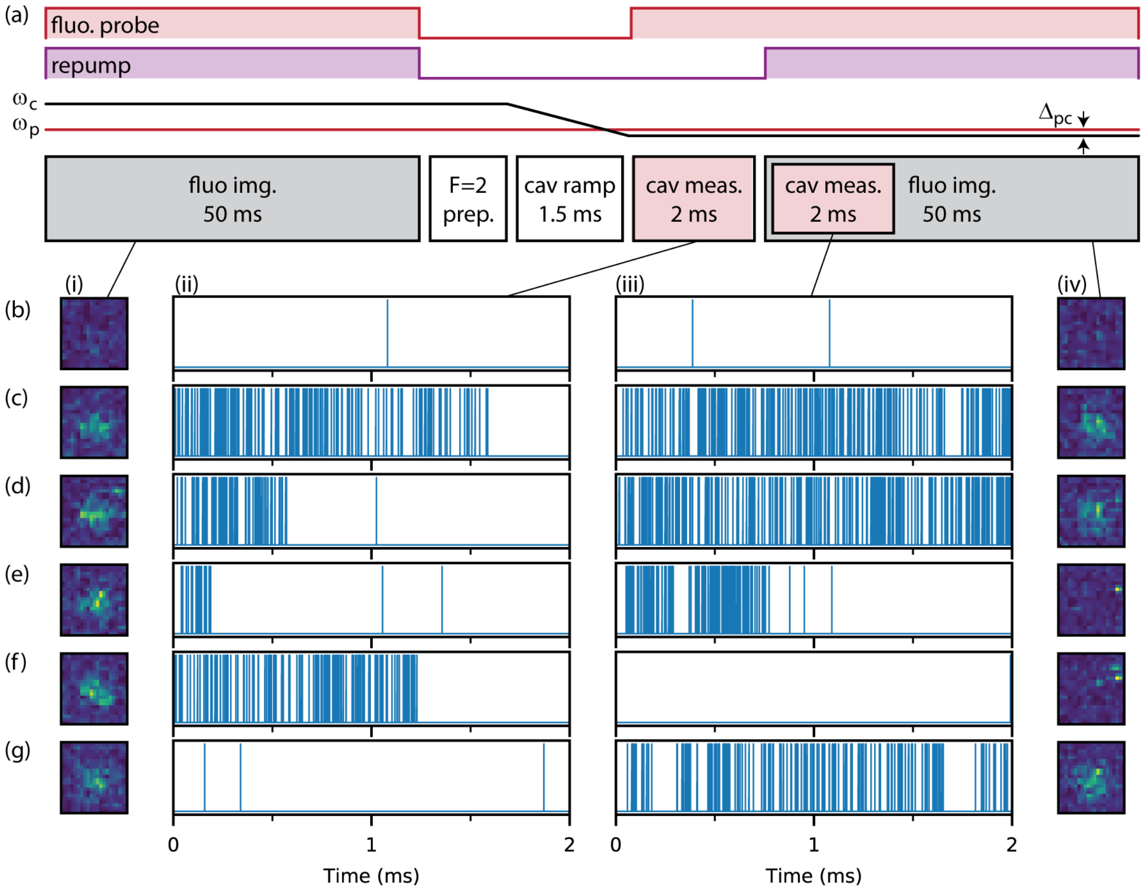

Figure 6.3: Cavity fluorescence detection and imaging. (a) Schematic of the imaging and cavity detection sequence. (b-g) Single-shot data from the first fluorescence image (i), cavity probe without repump (ii), and overlapping cavity probe with repump and second fluorescence imaging exposure (iii,iv). (b) No atom. (c-d) Atom is present and survives the full sequence, with different τ_{depump} during the first cavity probe interval. (e) Atom is lost during the second cavity probe interval. (f) Atom is lost during the first cavity probe interval. (g) State preparation error: atom is present at the beginning and end of the sequence but does not fluoresce in the first cavity probe interval.

cavity detection. This is achieved by ramping the frequency of the cavity lock light using the AOM shown in Fig. 3.3; the science cavity follows the ramp in-lock.[3] The first cavity probe interval, with a duration of 2 ms, is done with just fluorescence probe light. Then the global repump light is turned back on, and a second cavity probe interval and fluorescence imaging exposure are triggered simultaneously. Cavity photon arrivals are recorded just during the first 2 ms of the 50 ms imaging exposure.

Characteristic data taken at at $\Delta_{\mathrm{pc}} \sim 0$ are shown in Fig. 6.3(b-g), each comprising real data from a distinct experimental shot. The fluorescence images, (i) and (iv), are cropped to the ROI used for single-atom detection. The cavity photon detection traces, (ii) and (iii), are shown as a string of pulses, representing each TTL pulse produced by the SPCM upon detection of a photon. The SPCM detection system is described in more detail in Section 3.3.3.

In Fig. 6.3(b-d), the difference between "no atom" (b) and "with atom" (c,d) data are clear, both in the fluorescence images and in the cavity photon counts. But the cavity photon traces provide more information than just the binary tweezer occupation; from these data, we can also observe internal state dynamics and atom loss. During the first cavity probe interval, we see atoms (c-e) stop fluorescing after about 1.5, 0.5, and 0.25 ms respectively. Because fluorescence begins again in the second cavity probe interval when the repump light is turned on, we understand that these atoms were depumped to the dark $F = 1$ ground state. Data such as these reveal the depumping timescale, discussed below.

In contrast, when atom (f) stops fluorescing, it is considered lost, not depumped, as it does not reappear in the second cavity probe interval. Atom (e) is also lost about one millisecond into the second cavity probe interval. The loss of atoms (e) and (f) is confirmed by their final fluorescence images.

Atom (g) represents a somewhat rare event: it appears in the first image, but not in the first cavity detection interval. Without more information, this would suggest loss near the end of or after the imaging exposure. However, it reappears in the second cavity detection interval and final image. We thus conclude that atom (g) spent the entire first cavity detection interval in the dark $F = 1$ state, representing a state preparation error.

This handful of examples already illustrates some of the benefits of the higher efficiency and time-resolved nature of cavity photon detection, as compared to fluorescence imaging. Below, we process such data to observe the depumping timescale and the signature of atomic motion in the second-order correlation function.

Depumping timescale

We observe the depumping timescale in the histogram of photon arrival times in the first cavity probe interval, shown in Fig. 6.4(a). For this, we postselect data based on the second cavity probe result, selecting shots such as those shown in Fig. 6.3(c-e), but not (f), to

---

[3] There might be some lag in how the cavity follows the frequency sweep of the cavity lock light. However, the detected cavity fluorescence in Fig. 6.3(ii) and (iii) indicate that the timescale of the lag is within far less than the measurement duration.

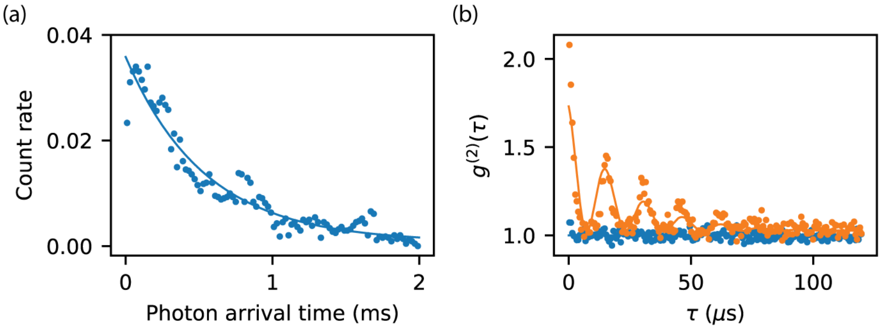

Figure 6.4: Depumping and atomic motion observed in cavity fluorescence. (a) Photon count rate vs time during the first cavity probe interval, obtained from 4415 experimental shots postselected for atom survival. The solid line is an exponential fit, which yields a characteristic depumping time of 0.54(4) ms. (b) The second-order correlation function $g^{(2)}(\tau)$ is calculated for empty cavity transmission (blue) and postselected "with atom" cavity fluorescence (orange). The empty cavity transmission shows the expected $g^{(2)}(\tau) = 1$ of coherent light. The oscillations in the "with atom" data indicate atomic motion. The solid line is a fit to a decaying sinusoid with a frequency of $2\pi \times 63(1)$ kHz and decay time of 21(2) μs.

distinguish between depumping and atom loss. An exponential fit indicates a characteristic depumping time of about 0.5 ms for the $\Delta_{\text{pa}} = -2\pi \times 30$ MHz setting used in this dataset. This timescale should increase as we bring the probe laser frequency closer to the cQED transition ($\Delta_{\text{pa}} \to 0$) and farther from the $F = 2 \to F' = 2$ depumping transition that causes these errors, and should also scale inversely with probe strength.

Second-order correlation function $g^{(2)}(\tau)$ measurement

We can also extract more information from the cavity photon time traces by calculating the second-order correlation function $g^{(2)}(\tau)$. $g^{(2)}(\tau)$ quantifies the likelihood of detecting two photons separated by the time τ and can be written as

$$g^{(2)}(\tau) = \frac{\langle n_1(t) n_2(t+\tau)\rangle}{\langle n_1(t)\rangle\langle n_2(t+\tau)\rangle} \tag{6.10}$$

Here, $n(t)$ is the number of counts detected at time t, and the subscripts indicate which detector; a $g^{(2)}(\tau)$ measurement is typically performed with two detectors detecting the two output ports of a beam splitter. Of particular interest to the quantum optician is of course $g^{(2)}(0)$, which is used to classify coherent ($g^{(2)}(0) = 1$), bunched ($g^{(2)}(0) > 1$), and antibunched ($g^{(2)}(0) < 1$) light [156]. Since our cavity fluorescence measurement detects photons fluoresced by a single atom, a $g^{(2)}(0)$ measurement should indicate antibunching [157–161]. However, we do not have a second SPCM in our detection path, so we can only measure

$g^{(2)}(\tau)$ for τ larger than the SPCM dead time of 50 ns, long enough that we cannot observe antibunching.

With our single detector, we measure $g^{(2)}(\tau)$ for $\tau > 50$ ns as follows. For each cavity photon trace, we calculate the difference in arrival times between each pair of detected photons. These are counted in bins centered around different τ and normalized according to the total number of photon pairs, bin size, detection time, and delay time τ, yielding $g^{(2)}(\tau)$. $g^{(2)}(\tau)$ is shown in Fig. 6.4(b) for coherent empty cavity transmission, for which $g^{(2)}(\tau) = 1$, and for cavity fluorescence measured in the second cavity probe interval, postselecting data where the atom survives the final fluorescence image. For these data, the repump light is on and the average photodetection rate thus constant through the interval, simplifying the correlation normalization.

Here, we see oscillations in $g^{(2)}(\tau)$ at a frequency of $2\pi \times 63(1)$ kHz. We believe this is a signature of atomic motion, as observed previously in many settings [158, 161–166]; increased atom-cavity coupling, and thus correlated photon emission events, occur as the atom passes through the antinodes of the cavity mode. Such motion, along the cavity axis, occurs at the radial frequency of the tweezer trap, which we independently estimate to be about $2\pi \times 80$ kHz, based on the estimated tweezer waist and measured tweezer ac Stark shift. The discrepancy between the expected and measured frequencies might indicate a larger tweezer waist, perhaps due to optical aberration.

6.3.2 Cavity backaction on free-space fluorescence

With data such as those shown in Fig. 6.3, we now look at the cavity and free-space scattering rates as a function of Δ_{pc}. Fig. 6.5(a) and (b) shows the cavity counts and free space fluorescence counts detected within the appropriate single atom ROI detected during the overlapping second cavity probe interval and fluorescence image. The results qualitatively agree with the theoretical prediction for the low-saturation regime given in Eq. (6.9).

In the cavity counts, we see the cavity resonance with linewidth slightly broader than the expected κ, likely due to cavity drift during the experiment. In the free-space imaging counts, we see not a constant scattering rate proportional to $1/\Delta_{\mathrm{pa}}^2$, as for a two-level system driven with near-resonant light—recall Eq. (5.1)—but a scattering rate that changes with the cavity frequency. When the probe is red-detuned of cavity resonance ($\omega_p < \omega_c$), the atom scatters faster into free space, and the opposite on the other side of resonance. This is a well-studied effect dubbed "cavity backaction" [76, 89, 167–169], referring to the cavity field, building up as a result of atomic emission, acting back on the atomic emission rate as an additional drive term. The free space scattering rate increases when the cavity field is in phase with the drive, which occurs when $\Delta_{\mathrm{pc}} < 0$; the opposite is also true. Refs. [89, 169] present single-atom cavity backaction data very similar to those shown in Fig. 6.5(b), but taken much closer to atomic resonance. Related phenomena have also been studied in free space [170–172].

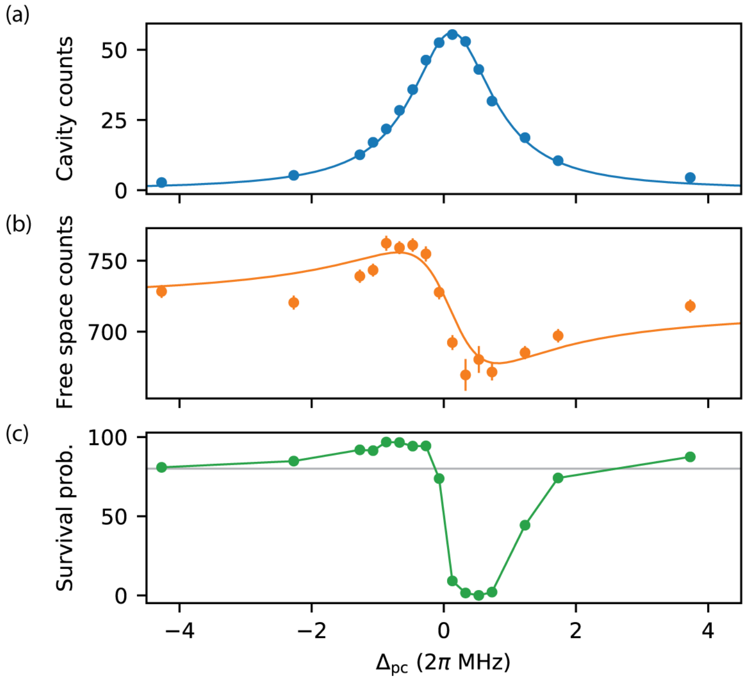

Figure 6.5: Cavity backaction, heating and cooling in fluorescence. Cavity counts (a) and free space fluorescence counts (b) vs detuning during a 2 ms cavity detection interval and 50 ms imaging exposure. Solid lines are the theoretical prediction in the low-saturation regime, plotted according to Eq. (6.9) with $\{\kappa, \Gamma, g, \Delta_{\mathrm{pa}}\} = 2\pi \times \{1.5, 6.07, -34, 1.2\}$ MHz and scaled to show qualitative agreement with the data. This is not a fit and should not be taken as a measurement of κ or g. The broadened linewidth of the cavity counts is likely due to experimental drift. (c) The imaging survival probability provides a proxy for atom temperature following cavity detection at different Δ_{pc}. Variation above and below the background level (gray line, approximate) suggests cavity cooling and heating effects. These data are taken with the atoms trapped at a radial distance of about 10 μm from the center of the cavity and with a 600 ms between the first cavity probe interval and second fluorescence image.

6.3.3 Cavity cooling and heating in fluorescence

In Fig. 6.5(c), I show the atomic survival probability as a function of Δ_{pc}. The survival probability is defined as the probability that a single atom, observed in the initial fluorescence image, is still present in the second fluorescence image, taken after an added hold time with a duration of 600 ms.

The data at $\Delta_{\text{pc}} = \pm 2\pi \times 4$ MHz show the background imaging survival probability, due to the heating of just free space scattering without significant cavity coupling. Closer to cavity resonance, we see evidence of cavity cooling and heating in the increase and decrease of the survival probability relative to this background level. This can be understood simply in terms of energy conservation: When $\omega_p < \omega_c$, each photon scattered from the probe into the cavity by the atom takes a bit of energy out of the system, resulting in a lower atomic temperature and improved imaging survival probability. When $\omega_p > \omega_c$, each cavity photon puts energy into the system, resulting in greater atom loss. Note especially that the heating and cooling are not attributed to the different free space scattering rates observed on either side of cavity resonance: the trend goes in the wrong direction. Where the free space scattering rate is *increased* by cavity backaction, the atom loss rate goes down. Without cavity cooling, we would expect more scattering to result in more loss.

We do not attempt a detailed study of cavity cooling, which has been thoroughly investigated elsewhere [173–179]. We simply notice that we can benefit from operating in the cavity cooling regime to reduce the loss associated with our measurement, and select a probe-cavity detuning of $\Delta_{\text{pc}} \sim -\kappa/4$, where the cavity photodetection rate is only slightly reduced, for our fluorescence measurement.

6.3.4 Local fluorescence probing

For the above discussion and corresponding data, the atom array was illuminated with global fluorescence probe light, generated by the cavity probe laser and coupled into the molasses 1 beam path, for simultaneous cavity detection and free space imaging. After this preliminary study of cavity fluorescence detection, we changed our experimental configuration to realize local detection; this is a key requirement for our mid-circuit measurement, demonstrated in Ref. [54].

To do this, we built the upper and lower probe paths, described in Section 3.2, and returned to using molasses light derived from the MOT laser for free space fluorescence imaging. It was necessary to use the z (up-down) axis for local fluorescence probing, where the NA is sufficient to create tightly focused beams that illuminate just the atom held in the center of the cavity. As a result, we cannot do simultaneous free space detection during local probing, as the lower probe path propagates onto the fluorescence camera. A system with high-NA optical access along multiple axes would be able to study the free space analog of our local cavity fluorescence measurement. The high- and moderate-NA lenses above and below the cavity focus the upper and lower probe beams to $1/e^2$ intensity radii of 3.3 and 13 μm, respectively.

Given the dramatic difference in these waist sizes, the many optical elements between the fiber outputs on the science table and the atoms (see Fig. 3.9), and the low power required in such tightly focused spots, setting the upper and lower probe powers to achieve equal intensity at the location of the atom in the two counter-propagating beams would have been difficult using power meter measurements. Instead, we balanced the drive strengths based on the atomic response to each beam on its own. With a power-splitting half-wave plate dividing the local probe fiber output roughly equally between the upper and lower probe paths, the overall and relative power were then adjusted manually, by adding absorptive ND filters, as shown in Fig. 3.4, to give comparable cavity scattering rates under illumination each beam alone. Fine-tuning of the survival rate was then done using the power-balancing $L/2$. The atom loss rate is much improved under balanced counterpropagating illumination compared to single-beam illumination. The beams are configured in a lin$\perp$lin molasses configuration, with the upper probe north-south polarized and the lower probe east-west polarized, which realizes simultaneous one-dimensional PGC and further reduces atom loss.

The fluorescence data in Ref. [54], as well as the data in Fig. 6.7, use the local fluorescence probe beams.

6.3.5 Cavity scattering rate versus drive strength

In Ref. [54], Fig. 2(c), we show the cavity scattering rate as a function of drive strength, indicating a maximum R_{cav} at intermediate drive strength. This surprised us when it first showed up in numeric simulations; our naive expectation, based on the low-saturation result $R_{\text{cav}} = CR_{\text{fs}}$, was for the cavity scattering rate to increase monotonically with drive strength, plateauing at $C\Gamma/2$ with atomic saturation. Instead, simulations showed the cavity scattering rate peaking at an intermediate value and decreasing to a lower plateau in the strong drive limit. At first, we wondered if it was an error in the simulation code—but when we observed the effect in the data as well, we gave it some more thought and came to the understanding described here. The mean-field treatment developed by Leon Lu supports this more intuitive understanding.

We first revisit the simpler “textbook” problem: a two-level system driven by resonant light with decay. Solving the optical Bloch equations, one obtains the steady-state solution for the atomic excited state population:

$$\rho_{ee} = \frac{1}{2}\frac{|\Omega|^2}{\Delta^2 + (\Gamma/2)^2 + |\Omega|^2/2} \tag{6.11}$$

The total atomic scattering rate, given by $R = \Gamma\rho_{ee}$, is plotted in blue for a resonant (solid) and near-resonant (dashed) drive field in Fig. 6.6(a). This result is quite familiar to all students of atomic physics.

Before we add the cavity to this simple system, we consider the spectrum of the atomic emission, famously studied by Mollow [180], and treated and observed by many others [168,

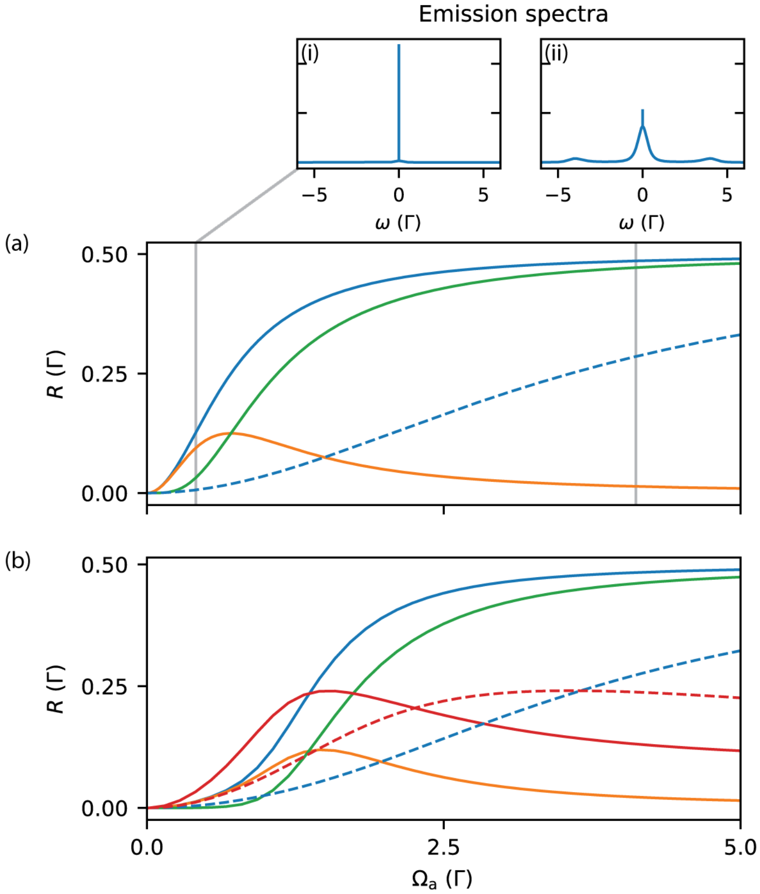

Figure 6.6: Resonance fluorescence in free space and in a cavity. Resonance fluorescence of a resonantly driven two-level system (a) in free space and (b) in a cavity, shown for $\kappa = \Gamma/6$ and $g = \Gamma/3$ ($C = 2.6$). R_{fs} (blue), R_{coh} (orange), R_{incoh} (green), R_{cav} (red) vs drive strength Ω_a, in units of Γ. Dashed line indicates the results for a detuned drive ($\Delta_{\mathrm{pa}} = -2.5\Gamma$). Insets (i) and (ii) show the power spectra of free space atomic emission at low and high drive strengths. Simulated with QuTiP [155]; sample code is included in Appendix C.

181–183].[4] In the low-saturation regime, the fluorescence is dominated by elastic scattering, represented by a delta function at the drive frequency, with total power

$$R_{\text{coh}} = \frac{s}{2(1+s)^2} \tag{6.12}$$

expressed in terms of the saturation parameter $s = 2(\Omega/\Gamma)^2/(1+4(\Delta/\Gamma)^2)$. The fact that the coherent peak dies off with increasing s can also be seen by examining the transverse dipole moment of the atom. This transverse moment precesses at the drive frequency, and produces an emission that is phase-locked to the driving field, i.e., it represents the coherent emission.

Under a strong driving field, however, the spectrum evolves into the "Mollow triplet," exhibiting a central peak at the drive frequency and symmetric sidebands separated by the Rabi frequency. The integrated power of this so-called "incoherent" or "inelastic" scattering is given by

$$R_{\text{incoh}} = \frac{s^2}{2(1+s)^2} \tag{6.13}$$

with half of the total power lying in the central peak and a quarter in each of the sidebands in the strong drive limit [183]. The coherent (orange) and incoherent (green) contributions to the total scattering rate (blue) are shown in Fig. 6.6(a). The calculated power spectra at weak and strong drive strengths are shown in insets (i) and (ii). These spectra provide clear intuition for an optimal cavity scattering rate at intermediate drive strength: the broad Mollow triplet spectrum of saturated atomic emission will certainly not couple into our narrow cavity. Instead, we should operate in a regime where there is still significant power in the coherent delta function scattering.

Armed with the intuition of this atomic physics review, we now re-consider the cavity-coupled two-level system. The numeric results are plotted in Fig. 6.6(b) for $C \sim 2.4$ and $\Delta_{\text{pa}} = \Delta_{\text{ca}} = 0$ (solid lines), with total, coherent, and incoherent free space emission shown in blue, orange, and green. The cavity scattering rate $R_{\text{cav}} = \kappa\langle a^\dagger a\rangle$ is shown in red. At weak drive strength, we see the expected low-saturation behavior: $R_{\text{cav}} = CR_{\text{fs}}$. At intermediate drive strengths, the atomic emission transitions from dominantly coherent to dominantly incoherent, and, as these couple into the cavity with different efficiency, the cavity scattering rate peaks and then rolls over. At large drive strength, the cavity scattering rate levels off at some saturation value defined by the cavity's filtering of the Mollow triplet spectrum.

In our experiment, we operate at finite probe-atom detuning Δ_{pa}. The dashed lines indicate the simulation results for free space and cavity scattering under a near-resonant drive field $\Delta_{\text{pa}} = -2.5\Gamma$.[5] We see that the maximum cavity scattering rate is only weakly dependent on the probe-atom detuning, but occurs at a larger drive strength for $\Delta_{\text{pa}} \neq 0$. This is consistent with our experimental observation and affects our optimization of Δ_{pa} for cavity measurement, discussed below.

---

[4] I find the treatment presented in Ref. [183] to be the most readable, and also benefited from reading about Mollow triplet studies in quantum dots [184].

[5] The probe and cavity are still taken to be resonant: $\Delta_{\text{pc}} = 0$.

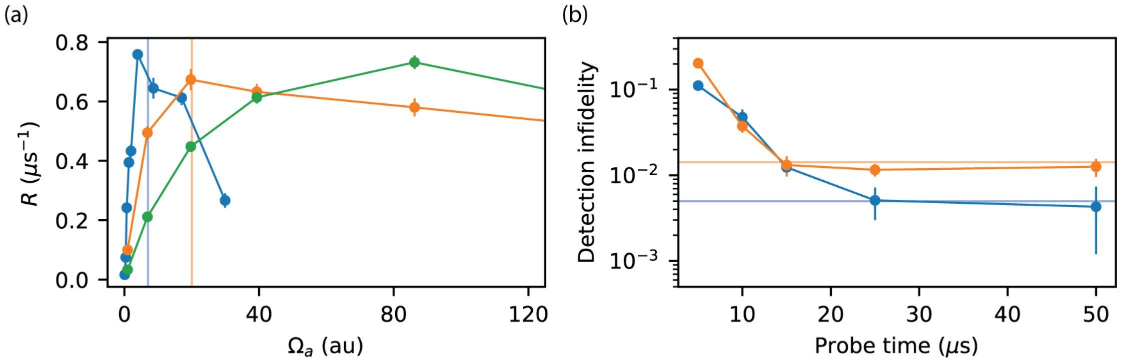

Figure 6.7: Probe-atom detuning and fluorescence measurement fidelity: optimizing Δ_{pa}. (a) Cavity scattering rate vs drive strength at $\Delta_{\text{pa}} = -2\pi \times 10$ MHz (blue), $-2\pi \times 20$ MHz (orange), and $-2\pi \times 30$ MHz (green). $R_{\text{cav}}^{\text{max}}$ is roughly constant, but occurs at different Ω_{opt} for different Δ_{pa}. (b) $F = 2$ detection infidelity vs cavity probe time for $\Delta_{\text{pa}} = -2\pi \times 10$ MHz (blue) and $-2\pi \times 20$ MHz (orange), at the approximate Ω_{opt} settings indicated by the blue and orange vertical lines in (a).

6.3.6 Measurement error and probe-atom detuning

Above, we have seen that the optimal fluorescence probe frequency lies slightly below the cavity frequency, to cause cavity cooling, and the optimal probe strength occurs where the cavity scattering rate is maximized. Here we investigate the relationship between the probe-atom detuning Δ_{pa} and measurement fidelity.

In the simplest two-level model, the measurement fidelity for a single probe interval is just a function of the separation between the "bright" ($F = 2$ atom) and "dark" (no $F = 2$ atom) photon distributions. The integration of these distributions below and above an optimized threshold yields the statistical measurement error. The separation between the average photon counts, determined by the dark counts rate, maximum cavity scattering rate, and measurement time, can theoretically be reduced indefinitely with a longer measurement. In a real system, though, other sources of error preclude an arbitrarily high-fidelity measurement. In particular, our measurement fidelity is limited by state-change errors at long measurement time.

By state-change errors, I mean $F = 2$ atoms being depumped into the dark $F = 1$ ground state, as observed in Figs. 6.3 and 6.4(a). Depumping errors occur as a result of off-resonant coupling between the probe light and the $F = 2 \to F' = 2$ transition, and the error rate scales with the drive strength and squared inverse of the detuning:

$$P_{\text{depump}} \propto \frac{\Omega_{2\to 2}}{(\Delta_{2\to 2})^2} = \frac{\Omega_{2\to 2}}{(\omega_{F'=3} - \omega_{F'=2} + \Delta_{\text{pa}})^2} \tag{6.14}$$

The $P_{\text{depump}} \propto \Delta_{2\to 2}^{-2}$ scaling is dominated by $\omega_{F'=3} - \omega_{F'=2} = 2\pi \times 267$ MHz, so changes to

$\Delta_{\rm pa}$ within our PGC range of $\Delta_{\rm pa} = -2\pi \times (10 - 35)$ MHz cannot significantly reduce the depump rate.

Instead, $\Delta_{\rm pa}$ more strongly modifies the depump rate through its effect on the optimal drive strength $\Omega_{\rm opt}$ that gives the maximum cavity scattering rate. Fig. 6.7(a) shows the cavity scattering rate versus drive strength for three settings of $\Delta_{\rm pa}$. As in the theory prediction given in Fig. 6.6(b), the observed maximum cavity scattering rate $R_{\rm cav}^{\rm max}$ is very weakly dependent on $\Delta_{\rm pa}$. However, $\Omega_{\rm opt}$ dramatically increases with $\Delta_{\rm pa}$, thus increasing the depumping rate and corresponding measurement infidelity limit at long measurement time.

Fig. 6.7(b) shows $F = 2$ detection infidelity versus measurement time data taken at $\Delta_{\rm pa} = -2\pi \times 10$ MHz and $-2\pi \times 20$ MHz, each approximately at its setting of $\Omega_{\rm opt}$. The difference in the detection infidelity limit at long measurement time is clear, due to the increased depump rate caused by larger $\Omega_{\rm opt}$ at larger $|\Delta_{\rm pa}|$. For this reason, we select $\Delta_{\rm pa} = -2\pi \times 10$ MHz for our optimized cavity fluorescence measurement.

Notably absent from my brief discussion here was any mention of the drive polarization and $\Omega_{2\to 2}$. If we could prepare the atoms in the $|F = 2, m_F = 2\rangle$ stretched state and probe them with σ^+–polarized light, $\Omega_{2\to 2}$, and our depumping error rate, would be very nearly 0. However, our fluorescence measurement requires simultaneous PGC, realized with lin$\perp$lin molasses light, so σ^+ and σ^+ probe polarizations are present.

6.4 Transmission measurement

The cavity transmission measurement is based on the hybrid modes of the Jaynes-Cummings Hamiltonian discussed in Chapter 2. Rather than driving the atom with fluorescence probe light from the side, described by the Ω_a terms in Eq. (6.2), we drive the cavity mode with transmission probe light, represented by the Ω_c terms. When the probe is resonant with the cavity frequency, the probe light is transmitted by the empty cavity and detected on the SPCM. However, when an atom in the $F = 2$ cavity-coupled state is present, and the cavity and atomic frequencies are resonant, the eigenspectrum is split into the hybrid atom-cavity excitations separated by the vacuum Rabi splitting. Probe light at the empty cavity frequency is no longer resonant with the hybridized excitations, and the amount of transmitted light is reduced. The difference between the high empty cavity transmission level and low coupled atom-cavity transmission level, which is optimal when $\omega_a \sim \omega_c \sim \omega_p$, provides the signal for cavity transmission detection.

The measurement sequence for transmission detection is very similar to the one used for fluorescence detection: after an initial fluorescence image and state preparation, the transmission probe light is turned on for the measurement duration, and a final fluorescence image is taken to check whether the atom survived the measurement. However, because both the high and low detection levels consist of a finite cavity transmission level, unlike the fluorescence detection which distinguishes the dark counts level from finite atomic fluorescence, the transmission measurement duration must be longer to achieve comparable measurement

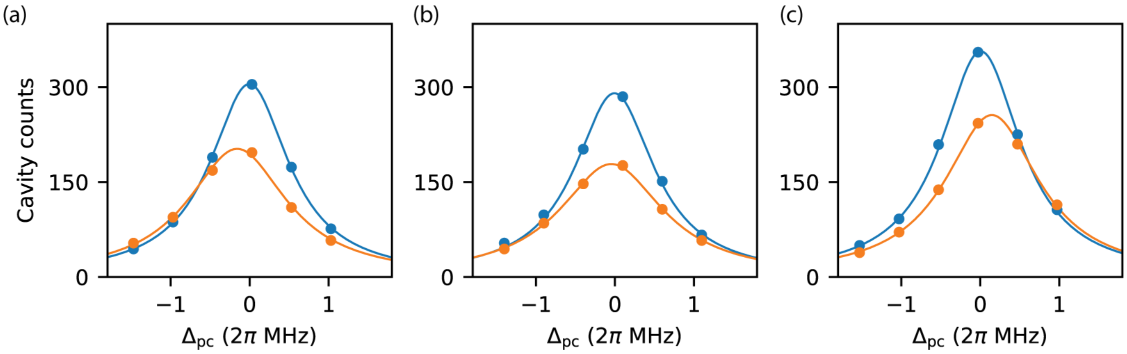

Figure 6.8: Finding atom-cavity resonance in transmission: setting $\Delta_{ca} = 0$. Empty cavity (blue) and coupled atom-cavity (orange) transmission for $\Delta_{ca} = -4$ MHz (a), $\Delta_{ca} = 0$ (b), and $\Delta_{ca} = 4$ MHz (c).

fidelity. The resonance conditions are also different: Δ_{ca} is set to a fixed value near zero, and we measure the transmission level versus Δ_{pc} by tuning the frequency of the transmission probe AOM (see Fig. 3.3).

6.4.1 Finding atom-cavity resonance

Because the cavity transmission measurement is based on the difference between the uncoupled and coupled atom-cavity eigenspectra, the measurement fidelity is very sensitive to the setting of Δ_{ca}. Only when the cavity and atom are nearly resonant do we see a large change in the cavity transmission level. Operating away from the atom-cavity resonance, one could consider single-atom detection in the dispersive cQED regime, using the phase of the transmission light rather than its amplitude [185–187].

To find $\Delta_{ca} = 0$, we first bring the cavity frequency to within a few megahertz of atomic resonance by adjusting the fEOM sideband frequencies of the cavity probe and lock laser systems, as described in Section 6.2.2. Then, to tune Δ_{ca} more precisely, we use the transmission detection signal versus Δ_{pc}: For $\Delta_{ca} \neq 0$, the dressed states have unequal components of the cavity $|g,1\rangle$ and atomic $|e,0\rangle$ excitation states. The one that is "more cavity"—i.e. the dressed state $\alpha|g,1\rangle + \beta|e,0\rangle$ with $|\alpha|^2 > |\beta|^2$—appears more strongly in the transmission spectrum, and is shifted in the direction of Δ_{ca} from the empty cavity resonance. For our parameters, the presence of an atom broadens rather than fully splits the empty cavity resonance, but the broadened peak is similarly shifted in the direction of Δ_{ca}. We thus adjust the cavity frequency until the "with-atom" transmission curve is symmetric and centered at the empty cavity frequency, indicating that $\Delta_{ca} = 0$.

Fig. 6.8 shows the empty cavity (blue) and "with-atom" (orange) cavity transmission counts versus Δ_{pc} for three settings of Δ_{ca}. The transmission probe duration is 100 μs. Each datapoint averages the results of roughly $30 - 60$ experimental shots, postselected as "empty cavity" or "with-atom" data based on the initial fluorescence image, and error bars represent the standard error of the mean obtained from repeated measurements. The asymmetry in the transmission data is obvious for $\Delta_{\rm ca} \neq 0$; in this way, we set $\Delta_{\rm ca} = 0$ to within the cavity linewidth κ. This scan is repeated before taking any important transmission data to accommodate various frequency drifts in the lab.

The difference in the maximum empty cavity transmission level in (a-c) is likely due to drift in the cavity input mode matching efficiency, as the transmission probe light intensity is stabilized at its fiber output on the science table. Note that these data were not taken at the optimal transmission probe drive strength: the maximum transmission level here of roughly 3 photons per microsecond exceeds the SPCM's self-heating threshold of 1 Mc/s (see Section 3.3.3) and corresponds to an intracavity photon number of about 1.7, outside the low saturation regime. The transmission reduction on resonance in Fig. 6.8(b) is worse than that observed under improved measurement conditions.

6.4.2 Transmission probe polarization

After finding $\Delta_{\rm ca} = 0$, we improve the measurement fidelity by using the atomic $|F = 2, m_F = 2\rangle$ stretched state for maximum cavity-atom coupling g. Such Zeeman state selectivity was not possible for the cavity fluorescence measurement due to the need for simultaneous PGC. The counter-propagating lin$\perp$lin fluorescence probe beams randomize the Zeeman state of the atom under measurement.

In the transmission measurement, however, we set the transmission probe polarization without the constraint of PGC. The strongest cavity-atom coupling is achieved for a circularly polarized cavity mode, σ^+– or σ^-–polarized with respect to the cavity axis, and its corresponding stretched state, with a Clebsch-Gordon coefficient of $1/\sqrt{2}$. Zeeman-specific state preparation is not necessary to benefit from this coupling enhancement: circularly polarized transmission probe light pumps any $F = 2$ atom into the correct maximally coupled state, quickly improving the transmission measurement contrast. Transmission measurements done with circularly and linearly polarized transmission probe light, set using the cavity input $L/4$ (see Fig. 3.11), are shown in Fig. 6.9. For all of these measurements, the atoms are prepared in the $F = 2$ manifold according to the state preparation protocol described in Section 4.5. We assume that the atoms are in a statistical mixture of all the Zeeman states at the beginning of the cavity probe interval. But the difference in the transmission level is clear. The circularly polarized probe light pumps the atom into the stretched state, while with linearly polarized probe light, the atoms remain in a mixture of the Zeeman states and experience reduced cavity coupling. These measurements are all done under zero magnetic field;[6] the light polarization defines the quantization axis of the Zeeman pumping.

The data in Fig. 6.9 appear to be taken at different $\Delta_{\rm ca}$, based on the larger asymmetry of the linear polarization data shown in (b). This might be a sign of cavity birefringence,

---

[6] We cancel earth's magnetic field using bias coils around the science chamber along the up-down, northeast-southwest, and northwest-southeast axes. I estimate that the residual magnetic field in our "zero-field configuration" is at the tens of milligauss level.

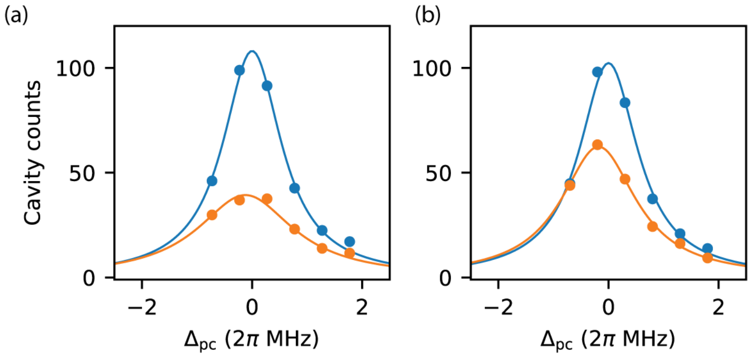

Figure 6.9: Probe polarization for transmission measurement. Cavity transmission vs $\Delta_{\rm pc}$, probing with circularly polarized light (a) and linearly polarized light (b). Greater transmission contrast is observed for circularly polarized probe light, as the atoms are pumped into the maximally coupled stretched state. The asymmetry of the coupled atom-cavity transmission in (b) may indicate cavity birefringence causing different settings of $\Delta_{\rm ca} = 0$ for linearly and circularly polarized cavity modes.

as data taken with circularly polarized probe light of the opposite handedness (not shown) resembles Fig. 6.9(a). The shift could also be due to uncontrolled frequency drifts in the lab; it was not investigated further.

6.4.3 A direct measurement of cooperativity?

Using the cavity transmission measurement, we hoped to quantitatively measure C, for comparison with our estimate of $C = 4.5$ derived from our measurement of κ and the cavity mode waist; see Table 2.2. The low-saturation theory [Eq. (6.9)] gives a resonant transmission reduction factor of $1/(1+C)^2$. This prediction does not depend on any other system parameters, including detection efficiency, and our system should be well-described by the two-level theory, since the atom is pumped by the circularly polarized probe light into the stretched state, as shown above. This initially sounded like a nice way to directly measure C.

The measurement is complicated, however, by the fact that our atoms are not well-localized at a single location along the cavity axis with well-defined g, but sample the full axial oscillation $g(x) = g_{\rm max}\sin(x)$. Where an atom localized at our theoretical $g_{\rm max} = 2.7$ MHz would yield a transmission reduction factor of $1/(1+C)^2 = 0.03$, averaging $1/(1+C\sin^2(x))^2$ over x yields the much worse reduction of 0.25.

Our observed resonant transmission reduction is shown in Fig. 6.10. Based on the empty cavity transmission data and fit (blue), we calculate the theoretical transmission of the atom-cavity coupled system for our theoretical $g_{\rm max}$ (gray line) and for an atom averaging $g(x)$ (orange line). The "with-atom" data (orange) only achieve a reduction of the empty

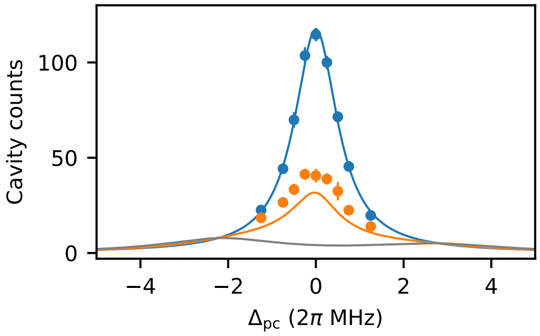

Figure 6.10: Cavity transmission comparison with theory. Shown in blue and orange are the cavity counts detected in a transmission probe duration of 50 μs without and with an atom. Solid lines indicate a Lorentzian fit to the empty cavity transmission (blue), and our theoretical expectation for the "with-atom" signal in the low-saturation regime, using $g_{\max} = 2\pi \times 2.7$ (gray) and axially averaged $g(x)$ (orange). The remaining discrepancy between the orange data and axially averaged theoretical result may be due to inhomogeneous broadening of the atomic resonance.

cavity level of 0.35, which would be consistent with the axially averaged $g(x)$ result for $g_{\max} \sim 2\pi \times 2$ MHz. Perhaps this indicates that our previous determination of $g_{\max} = 2\pi \times 2.7(4)$ MHz is wrong. But I think in reality, this is not the straightforward measurement of C that we had hoped. Other groups have similarly observed worse transmission reduction than they expected [96], which they attribute to broadening of Δ_{ca} due to ac Stark shifts to the cavity probe transition effected by trapping light [188]. This could certainly be true for our system as well, so we are not prepared to throw out our previous estimate of C based on this transmission measurement. Instead, we say that the data in Fig. 6.10 are not very far off from our axially averaged expectation (orange line), with the remaining difference possibly attributable to spectral broadening of the atomic line.

6.4.4 Cavity cooling and heating in transmission

As we explored the atom loss associated with transmission measurement, we encountered cavity cooling and heating for certain values of Δ_{pc} and Δ_{ca}. In the fluorescence measurement case, described in Section 6.3.3 above, the cavity heating and cooling that we observed can be explained quite simply in terms of the energy of each drive laser photon versus each cavity photon. Here, however, the cavity transmission cooling and heating regimes depend on both Δ_{pc} and Δ_{ca}, and require a more sophisticated explanation of cavity cooling as a type of Sisyphus cooling. Here, I follow the theoretical description given in Ref. [174].

The cavity cooling Sisyphus mechanism is schematically depicted in Fig. 6.11(a). The uncoupled cavity and atomic resonance frequencies are indicated by solid gray lines; here

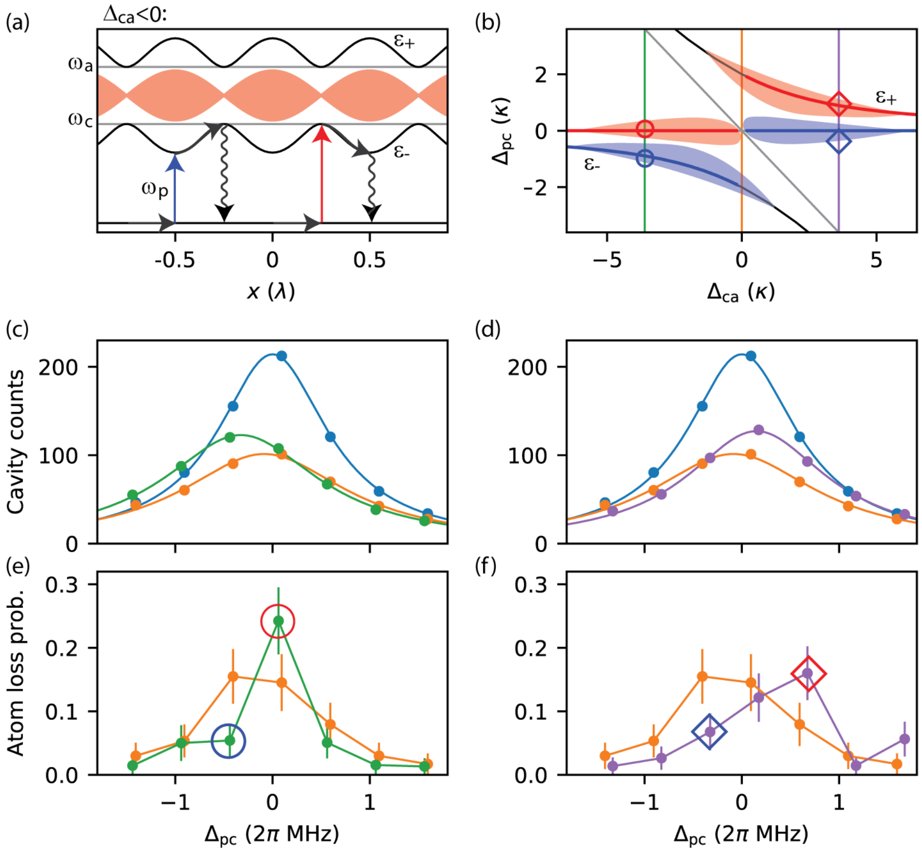

Figure 6.11: Cavity heating and cooling in transmission. (a) Sisyphus mechanisms for cavity cooling and heating, for $\Delta_{\text{ca}} < 0$. (b) Cavity heating and cooling regions vs Δ_{ca} and Δ_{pc}; the data in (c-f) are taken at the Δ_{ca} settings indicated by the vertical lines. (a-b) are based on Fig. 6 in Ref. [174]. (c-d) Empty cavity transmission (blue), and coupled atom-cavity transmission at different values of Δ_{ca}. (e-f) show the atom loss probability following cavity probing at these different settings, with evidence of cavity cooling and heating indicated in blue and red.

I take $\Delta_{\rm ca} < 0$. Cavity coupling splits the uncoupled atom and cavity excitations into the dressed states $|\pm\rangle$, with energies $\epsilon_\pm$ (black) that oscillate along the standing wave of the cavity mode (red). The lower $|-\rangle$ mode is the "more cavity" mode, and therefore the one that is most easily driven with the transmission probe light.

When $\Delta_{\rm pc} = 0$, the $|-\rangle$ mode is preferentially excited when the atom is at the node of the probe mode, indicated by the red arrow. As the atom moves along the axis, ϵ_- decreases, so that when the atom decays back to the zero-excitation $|g, 0\rangle$ state, it has lost some kinetic energy: cavity heating. On the other hand, when the probe is red-detuned from the cavity resonance, and in particular when $\Delta_{\rm pc}$ is nearly equal to the energy shift $-\sqrt{(\Delta_{\rm ca}/2)^2 + g^2}$, the $|-\rangle$ mode is preferentially excited when the atom is at the probe nodes, at the minimum of ϵ_-. This is indicated by the blue arrow. The atom will then climb the hill before decaying back to the ground state, giving up kinetic energy: cavity cooling. Analogous processes occur for $\Delta_{\rm ca} > 0$ with excitation of the higher-energy $|+\rangle$ mode: cooling near $\Delta_{\rm pc} = 0$, when the $|+\rangle$ state is preferentially excited at the probe nodes, and cooling for ω_p closer to the increased dressed state energy ϵ_+ found at the probe antinodes.

The cooling and heating regions as a function of $\Delta_{\rm ca}$ and $\Delta_{\rm pc}$ are summarized in Fig. 6.11(b). The horizontal $\Delta_{\rm pc} = 0$ axis and $\Delta_{\rm pc} = -\Delta_{\rm ca}$ gray line represent the uncoupled cavity and atomic frequencies, respectively, which the dressed state energies $\epsilon_\pm$ shown in black. Resonance between the probe and uncoupled cavity or "more cavity" dressed state ($|-\rangle$ for $\Delta_{\rm ca} < 0$ and $|+\rangle$ for $\Delta_{\rm ca} > 0$) yields cavity heating or cooling in the red and blue regions. The vertical lines indicate the $\Delta_{\rm ca}$ settings used for the data presented in Fig. 6.11(c-f), where we observe evidence of cavity cooling and heating at the highlighted points.

Fig. 6.11(c) and (d) show cavity transmission data for the empty cavity (blue) and "with-atom" cavity at $\Delta_{\rm ca} = 0$ (orange) and $\Delta_{\rm ca} \sim \pm 2\pi \times 4$ MHz (green and purple). These data were taken with a transmission probe duration of 50 μs and are similar to those shown in Fig. 6.8. We see the expected shifts of the $\Delta_{\rm ca} < 0$ green data to the left and $\Delta_{\rm ca} > 0$ purple data to the right of cavity resonance, as discussed in Section 6.2.2.

In the atom loss probability, however, we see more: a clear difference in the atom loss versus $\Delta_{\rm pc}$ for $\Delta_{\rm ca} = 0$ and $\Delta_{\rm ca} \neq 0$. This is shown in Fig. 6.11(e) and (f). For $\Delta_{\rm ca} = 0$ (orange), the atom loss trend is unsurprising: the loss probability is highest near cavity resonance, where the atom is subjected to the largest intensity of resonant light. This data is taken as our "background" loss rate, without cavity cooling or heating effects. For $\Delta_{\rm ca} \neq 0$ (green and purple), where the atom loss probability is below the background level, we credit cavity cooling; and above, cavity heating. These points are indicated with blue and red circles and diamonds, and agree generally with the cavity cooling and heating regimes shown in Fig. 6.11(b). These results represent preliminary signals of cavity cooling and heating that have been demonstrated previously and in much more detail with single atoms [176–178] and atomic ensembles [179].

Our cavity transmission measurement necessarily operates near $\Delta_{\rm pc} = 0$, where we obtain the maximum contrast between the uncoupled and coupled cavity transmission curves. Per this discussion, we must therefore be sure to operate with the cavity at or slightly above atomic resonance, avoiding excessive atom loss caused by cavity heating like that shown in the data point circled in red in Fig. 6.11(e), and even benefiting from reduced atom loss due to cavity cooling at the data point indicated with a blue diamond in Fig. 6.11(f).

6.5 Summary

The investigations discussed above led us to these optimized measurement conditions: For the fluorescence measurement, we operate at a probe-cavity detuning of roughly $\Delta_{\mathrm{pc}} \sim -\kappa/4$, where we achieve a large cavity scattering rate and simultaneous cavity cooling, as discussed in Section 6.3.3. We select a probe-atom detuning of $\Delta_{\mathrm{pa}} = -2\pi \times 10$ MHz and tune the drive strength to achieve the maximum cavity scattering rate; see Sections 6.3.6 and 6.3.5. At these settings, we detect an atom in the $F = 2$ with a measurement infidelity of less than 1% in a single cavity probe interval with a duration of 25 μs.

For the transmission measurement, we set the cavity and probe to be resonant with the atomic transition ($\Delta_{\mathrm{pc}} = \Delta_{\mathrm{pa}} = 0$), taking care to note that the cavity does not drift below atomic resonance, which causes cavity heating, as seen in Section 6.4.4. We drive the cavity with circularly polarized light, which pumps the atom into the maximally coupled stretched-state (Section 6.4.2), and set the drive strength to be just on the edge of the low-saturation regime, increasing the photodetection rate until it would compromise the optimal weak-drive transmission reduction factor (Section 6.4.3). Here, due to the high empty cavity background photodetection level, a longer measurement duration of 50 μs is required to achieve a measurement infidelity at the subpercent level.

These are the optimized measurement conditions used in Ref. [54], included also in Appendix B. In the published work, we also add a short pulse of local repump light and second cavity probe interval to fully distinguish an atom in the $F = 2$ manifold, an atom in the $F = 1$ manifold, and no atom. These two-probe cavity measurements are then performed in a two-atom array, and a Ramsey experiment confirms that the cavity measurement of the atom trapped inside the cavity does not decohere the atom trapped outside the cavity, thus realizing the requirements for a mid-circuit measurement in a neutral atom array.

6.6 Improvements

I now offer a few ideas about how to improve the cavity measurements discussed here. Of course, a better cavity with greater cooperativity and detection efficiency would achieve measurement fidelity that outperforms ours; but even within our system, our measurement could be improved.

An obvious step would be to improve the axial confinement of our tweezer-trapped atoms. The tweezer waist is quite large compared to the cavity probe half-wavelength of 390 nm; stronger confinement could be achieved with a one-dimensional optical lattice using a cavity mode at a different wavelength. Our initial plan of a lattice formed by the cavity lock light, discussed in the introduction of Chapter 5, might work for this, but a shorter wavelength lattice would create a tighter trap and avoid the annoyance of the excited state ac Stark shift of the cavity lock light. The tweezers would be used to trap single atoms at trap minima that overlap with probe antinodes, as in Refs. [80, 87]. This technical upgrade would especially benefit the cavity transmission measurement, because the resonant low-saturation transmission reduction factor of $1/(1+C)^2$ is hard-hit by averaging over $g^2(x)$, as seen in the difference between the gray and orange lines in Fig. 6.10.

Atom loss associated with our fluorescence measurement could be reduced by using feedback to stop a probe interval as soon as the detection threshold is reached. For the optimized fluorescence measurement presented in Ref. [54], with probe durations of 20 μs, this threshold is 2 photons; however, the average above-threshold detection is nearly 15 photons. The heating associated with scattering all these photons would be reduced, and the average measurement time for atoms in the $F = 2$ would also go down.

The transmission measurement fidelity could be improved in two ways: by using a second SPCM for coincidence detection, or by implementing polarization-sensitive detection. With a second SPCM, we could measure $g^{(2)}(0)$, as discussed in Section 6.3.1. The difference between coherent light transmitted by the empty cavity, with $g^{(2)}(0) = 1$, and light that has probed the atom-cavity hybrid system, might provide a signal that could be used along with photon count threshold to reduce the time required for high-fidelity transmission measurement. Polarization-sensitive detection would benefit the transmission measurement by removing the high empty cavity transmission level: the detection of photons with the opposite polarization of the input cavity probe light would signal the presence of an atom, as implemented in Ref. [189]. Part of the signal arises from spontaneous emission, with the measurement functioning as a sort of hybrid between our transmission and fluorescence measurements. Transmission probe light of a certain polarization drives unpolarized atomic fluorescence, and those photons whose polarization is opposite the probe polarization is collected and detected through the cavity, as in the cavity fluorescence measurement. Additionally, atom-induced birefringence between circularly-polarized cavity modes causes Faraday rotation of linearly-polarized probe light, adding a coherent contribution to the signal in the opposite polarization mode. Both opposite-polarization signals benefit from the fact that the empty cavity background level is now low.

Chapter 7

Outlook

The work presented in this thesis points to future directions in quantum sensing and quantum information processing.

Chapter 5 presents a simple quantum sensing result in which single atoms are used to perform superresolution measurements of optical fields within our cavity [53]. Our sensor operates in two modes: directly detecting the cavity lock light through its ac Stark shift of the imaging resonance, and detecting the cavity probe light through its force, which pulls atoms away from the tweezer trap minima, distorting the measurement of the cavity lock "ruler." ac Stark shift measurement could be helpful in characterizing and optimizing optical fields used in increasingly complex quantum matter simulations [40, 190]. However, most optical fields do not have the advantage of the cavity lock light that we used to demonstrate this measurement: the large shift to the imaging transition but negligible effect on the ground state trapping potential. The force-sensing measurement of the cavity probe light may offer a more general method for detecting optical fields—and anything else that exerts a force—using a spatially varying auxiliary field that exerts a large excited-state shift. This auxiliary field need not be a standing wave, as in our experiment; better sensitivity would be achieved with linear variation of the auxiliary field at the tweezer trap minimum, achieved, for instance, with a second tightly focused auxiliary tweezer, slightly offset from the tweezer trap and moving with it in a scanning-probe atomic-force microscope.

Tweezer-trapped single atoms also offer prospects in quantum metrology outside of optical field and force detection, notably in the realization of "tweezer clocks" [36, 149]. Here, the advantage of using individually trapped atoms is not their superresolving capability, but the single-particle coherent control, high-fidelity readout, and possibilities for engineering entanglement offered by a tweezer array. Our cavity would provide additional advantages to tweezer clocks. Single-atom nondestructive cavity measurement, as discussed in Chapter 6, could enable a continuously running atomic tweezer clock. Alternatively, the cavity could be used to generate all-to-all entanglement for improved time-keeping with sensitivity beyond the standard quantum limit [191].

Chapter 6 discusses a quantum information processing result: the realization of a mid-circuit measurement enabled by local nondestructive cavity detection [54]. An atom in the cavity-coupled state is detected either by collecting Purcell-enhanced spontaneous emission through the cavity, in the cavity fluorescence measurement, or by observing a reduction in transmitted light at the empty cavity resonance frequency due to the hybridized atom-cavity excitations of the Jaynes-Cummings model, in the cavity transmission measurement. Both of these measurements, enabled by the enhanced light-matter interaction that cavity QED provides, exceed the performance of free-space state detection in fidelity and speed, and do so without losing the atom under measurement or destroying the hyperfine coherence of a nearby atom, standing in for a larger coherent array. The low error rate, rapid detection speed, and locality of our cavity measurements satisfy the requirements of a mid-circuit measurement, which is in turn a requirement for many quantum error correction protocols.

Realizing quantum error correction using cavity measurement would have dramatic implications in quantum metrology and information processing; however, our demonstration of a mid-circuit measurement represents just one small piece of the puzzle [54]. Performing a mid-circuit measurement in a fully capable Rydberg tweezer array would be a significant next step, and will require substantial technical upgrades to the apparatus described in this thesis. Preparation for these upgrades has already begun. Adding to our cavity system the capabilities of leading Rydberg atom quantum processors, rapidly improving in both academia and industry, promises exciting future directions.

Bibliography

[1] A. Celi, A. Sanpera, V. Ahufinger, and M. Lewenstein, "Quantum optics and frontiers of physics: the third quantum revolution", *Phys. Scr.*, **92**, 013003 (2016) (cit. on p. 1).

[2] D. Maslov, Y. Nam, and J. Kim, "An Outlook for Quantum Computing [Point of View]", *Proc. IEEE*, **107**, 5 (2019) (cit. on p. 1).

[3] Y. Alexeev, D. Bacon, K. R. Brown, R. Calderbank, L. D. Carr, F. T. Chong, B. DeMarco, D. Englund, E. Farhi, B. Fefferman, A. V. Gorshkov, A. Houck, J. Kim, S. Kimmel, M. Lange, S. Lloyd, M. D. Lukin, D. Maslov, P. Maunz, C. Monroe, J. Preskill, M. Roetteler, M. J. Savage, and J. Thompson, "Quantum Computer Systems for Scientific Discovery", *PRX Quantum*, **2**, 017001 (2021) (cit. on p. 1).

[4] I. M. Georgescu, S. Ashhab, and F. Nori, "Quantum simulation", *Rev. Mod. Phys.*, **86**, 153 (2014) (cit. on p. 1).

[5] E. Altman, K. R. Brown, G. Carleo, L. D. Carr, E. Demler, C. Chin, B. DeMarco, S. E. Economou, M. A. Eriksson, K.-M. C. Fu, M. Greiner, K. R. Hazzard, R. G. Hulet, A. J. Kollár, B. L. Lev, M. D. Lukin, R. Ma, X. Mi, S. Misra, C. Monroe, K. Murch, Z. Nazario, K.-K. Ni, A. C. Potter, P. Roushan, M. Saffman, M. Schleier-Smith, I. Siddiqi, R. Simmonds, M. Singh, I. Spielman, K. Temme, D. S. Weiss, J. Vučković, V. Vuletić, J. Ye, and M. Zwierlein, "Quantum Simulators: Architectures and Opportunities", *PRX Quantum*, **2**, 017003 (2021) (cit. on p. 1).

[6] C. L. Degen, F. Reinhard, and P. Cappellaro, "Quantum sensing", *Rev. Mod. Phys.*, **89**, 035002 (2017) (cit. on pp. 1, 63).

[7] L. Pezzè, A. Smerzi, M. K. Oberthaler, R. Schmied, and P. Treutlein, "Quantum metrology with nonclassical states of atomic ensembles", *Rev. Mod. Phys.*, **90**, 035005 (2018) (cit. on p. 1).

[8] N. Gisin and R. Thew, "Quantum communication", *Nat. Photon.*, **1**, 165 (2007) (cit. on p. 1).

[9] A. A. Houck, H. E. Tureci, and J. Koch, "On-chip quantum simulation with superconducting circuits", *Nat. Phys.*, **8**, 292 (2012) (cit. on p. 1).

[10] M. H. Devoret and R. J. Schoelkopf, "Superconducting Circuits for Quantum Information: An Outlook", *Science*, **339**, 1169 (2013) (cit. on p. 1).

[11] J. R. Weber, W. F. Koehl, J. B. Varley, A. Janotti, B. B. Buckley, C. G. V. D. Walle, and D. D. Awschalom, “Quantum computing with defects”, *Proc. Natl. Acad. Sci. U.S.A.*, **107**, 8513 (2010) (cit. on p. 1).

[12] L.-M. Duan and H. J. Kimble, “Scalable Photonic Quantum Computation through Cavity-Assisted Interactions”, *Phys. Rev. Lett.*, **92**, 127902 (2004) (cit. on p. 1).

[13] S. Slussarenko and G. J. Pryde, “Photonic quantum information processing: A concise review”, *Appl. Phys. Rev.*, **6**, 041303 (2019) (cit. on p. 1).

[14] R. Blatt and C. F. Roos, “Quantum simulations with trapped ions”, *Nat. Phys.*, **8**, 277 (2012) (cit. on p. 1).

[15] C. Monroe and J. Kim, “Scaling the Ion Trap Quantum Processor”, *Science*, **339**, 1164 (2013) (cit. on p. 1).

[16] M. Saffman, T. G. Walker, and K. Mølmer, “Quantum information with Rydberg atoms”, *Rev. Mod. Phys.*, **82**, 2313 (2010) (cit. on p. 1).

[17] M. Saffman, “Quantum computing with neutral atoms”, *Natl. Sci. Rev.*, **6**, 24 (2018) (cit. on p. 1).

[18] L. Henriet, L. Beguin, A. Signoles, T. Lahaye, A. Browaeys, G.-O. Reymond, and C. Jurczak, “Quantum computing with neutral atoms”, *Quantum*, **4**, 327 (2020) (cit. on p. 1).

[19] T. D. Ladd, F. Jelezko, R. Laflamme, Y. Nakamura, C. Monroe, and J. L. O’Brien, “Quantum computers”, *Nature*, **464**, 45 (2010) (cit. on p. 1).

[20] W. D. Phillips, “Nobel Lecture: Laser cooling and trapping of neutral atoms”, *Rev. Mod. Phys.*, **70**, 721 (1998) (cit. on p. 1).

[21] W. Ketterle, “Nobel lecture: When atoms behave as waves: Bose-Einstein condensation and the atom laser”, *Rev. Mod. Phys.*, **74**, 1131 (2002) (cit. on p. 1).

[22] E. A. Cornell and C. E. Wieman, “Nobel Lecture: Bose-Einstein condensation in a dilute gas, the first 70 years and some recent experiments”, *Rev. Mod. Phys.*, **74**, 875 (2002) (cit. on p. 1).

[23] I. Bloch, “Ultracold quantum gases in optical lattices”, *Nat. Phys.*, **1**, 23 (2005) (cit. on p. 1).

[24] I. Bloch, J. Dalibard, and S. Nascimbène, “Quantum simulations with ultracold quantum gases”, *Nat. Phys.*, **8**, 267 (2012) (cit. on p. 1).

[25] C. Gross and W. S. Bakr, “Quantum gas microscopy for single atom and spin detection”, *Nat. Phys.*, **17**, 1316 (2021) (cit. on pp. 1, 10).

[26] A. M. Kaufman and K.-K. Ni, “Quantum science with optical tweezer arrays of ultracold atoms and molecules”, *Nat. Phys.*, **17**, 1324 (2021) (cit. on p. 1).

[27] N. Schlosser, G. Reymond, I. Protsenko, and P. Grangier, “Sub-poissonian loading of single atoms in a microscopic dipole trap”, *Nature*, **411**, 1024 (2001) (cit. on pp. 1, 17, 51).

[28] A. M. Kaufman, B. J. Lester, and C. A. Regal, “Cooling a Single Atom in an Optical Tweezer to Its Quantum Ground State”, *Phys. Rev. X*, **2**, 041014 (2012) (cit. on p. 1).

[29] M. Endres, H. Bernien, A. Keesling, H. Levine, E. R. Anschuetz, A. Krajenbrink, C. Senko, V. Vuletić, M. Greiner, and M. D. Lukin, “Atom-by-atom assembly of defect-free one-dimensional cold atom arrays”, *Science*, **354**, 1024 (2016) (cit. on pp. 1, 17, 51, 71, 76).

[30] D. Barredo, S. D. Léséleuc, V. Lienhard, T. Lahaye, and A. Browaeys, “An atom-by-atom assembler of defect-free arbitrary two-dimensional atomic arrays”, *Science*, **354**, 1021 (2016) (cit. on pp. 1, 17, 51, 71, 76).

[31] H. Weimer, M. Müller, I. Lesanovsky, P. Zoller, and H. P. Büchler, “A Rydberg quantum simulator”, *Nat. Phys.*, **6**, 382 (2010) (cit. on p. 1).

[32] A. Browaeys and T. Lahaye, “Many-body physics with individually controlled Rydberg atoms”, *Nat. Phys.*, **16**, 132 (2020) (cit. on p. 1).

[33] H. Levine, A. Keesling, G. Semeghini, A. Omran, T. T. Wang, S. Ebadi, H. Bernien, M. Greiner, V. Vuletić, H. Pichler, and M. D. Lukin, “Parallel Implementation of High-Fidelity Multiqubit Gates with Neutral Atoms”, *Phys. Rev. Lett.*, **123**, 170503 (2019) (cit. on pp. 1, 9, 71).

[34] D. Bluvstein, H. Levine, G. Semeghini, T. T. Wang, S. Ebadi, M. Kalinowski, A. Keesling, N. Maskara, H. Pichler, M. Greiner, V. Vuletić, and M. D. Lukin, “A quantum processor based on coherent transport of entangled atom arrays”, *Nature*, **604**, 451 (2022) (cit. on pp. 1, 9, 10).

[35] A. Cooper, J. P. Covey, I. S. Madjarov, S. G. Porsev, M. S. Safronova, and M. Endres, “Alkaline-Earth Atoms in Optical Tweezers”, *Phys. Rev. X*, **8**, 041055 (2018) (cit. on p. 1).

[36] M. A. Norcia, A. W. Young, W. J. Eckner, E. Oelker, J. Ye, and A. M. Kaufman, “Seconds-scale coherence on an optical clock transition in a tweezer array”, *Science*, **366**, 93 (2019) (cit. on pp. 1, 98).

[37] Z. Z. Yan, B. M. Spar, M. L. Prichard, S. Chi, H.-T. Wei, E. Ibarra-García-Padilla, K. R. A. Hazzard, and W. S. Bakr, “Two-Dimensional Programmable Tweezer Arrays of Fermions”, *Phys. Rev. Lett.*, **129**, 123201 (2022) (cit. on p. 1).

[38] A. Jenkins, J. W. Lis, A. Senoo, W. F. McGrew, and A. M. Kaufman, “Ytterbium Nuclear-Spin Qubits in an Optical Tweezer Array”, *Phys. Rev. X*, **12**, 021027 (2022) (cit. on p. 1).

[39] L. Anderegg, L. W. Cheuk, Y. Bao, S. Burchesky, W. Ketterle, K.-K. Ni, and J. M. Doyle, “An optical tweezer array of ultracold molecules”, *Science*, **365**, 1156 (2019) (cit. on p. 1).

[40] J. Trisnadi, M. Zhang, L. Weiss, and C. Chin, “Design and construction of a quantum matter synthesizer”, *Rev. Sci. Instrum.*, **93**, 083203 (2022) (cit. on pp. 1, 98).

[41] H. Mabuchi and A. Doherty, “Cavity Quantum Electrodynamics: Coherence in Context”, *Science*, **298**, 1372 (2002) (cit. on p. 2).

[42] R. Miller, T. E. Northup, K. M. Birnbaum, A. Boca, A. D. Boozer, and H. J. Kimble, “Trapped atoms in cavity QED: coupling quantized light and matter”, *J. Phys. B: At. Mol. Opt. Phys.*, **38**, S551 (2005) (cit. on p. 2).

[43] H. Walther, B. T. Varcoe, B. G. Englert, and T. Becker, “Cavity quantum electrodynamics”, *Rep. Prog. Phys.*, **69**, 1325 (2006) (cit. on p. 2).

[44] S. Haroche, “Nobel Lecture: Controlling photons in a box and exploring the quantum to classical boundary”, *Rev. Mod. Phys.*, **85**, 1083 (2013) (cit. on p. 2).

[45] R. J. Thompson, G. Rempe, and H. J. Kimble, “Observation of normal-mode splitting for an atom in an optical cavity”, *Phys. Rev. Lett.*, **68**, 1132 (1992) (cit. on p. 2).

[46] A. Boca, R. Miller, K. M. Birnbaum, A. D. Boozer, J. McKeever, and H. J. Kimble, “Observation of the Vacuum Rabi Spectrum for One Trapped Atom”, *Phys. Rev. Lett.*, **93**, 233603 (2004) (cit. on p. 2).

[47] M. Brune, F. Schmidt-Kaler, A. Maali, J. Dreyer, E. Hagley, J. M. Raimond, and S. Haroche, “Quantum Rabi Oscillation: A Direct Test of Field Quantization in a Cavity”, *Phys. Rev. Lett.*, **76**, 1800 (1996) (cit. on pp. 2, 12).

[48] J. M. Raimond, M. Brune, and S. Haroche, “Manipulating quantum entanglement with atoms and photons in a cavity”, *Rev. Mod. Phys.*, **73**, 565 (2001) (cit. on p. 2).

[49] P. Goy, J. M. Raimond, M. Gross, and S. Haroche, “Observation of Cavity-Enhanced Single-Atom Spontaneous Emission”, *Phys. Rev. Lett.*, **50**, 1903 (1983) (cit. on p. 2).

[50] G. Gabrielse and H. Dehmelt, “Observation of inhibited spontaneous emission”, *Phys. Rev. Lett.*, **55**, 67 (1985) (cit. on p. 2).

[51] R. G. Hulet, E. S. Hilfer, and D. Kleppner, “Inhibited Spontaneous Emission by a Rydberg Atom”, *Phys. Rev. Lett.*, **55**, 2137 (1985) (cit. on p. 2).

[52] A. Reiserer and G. Rempe, “Cavity-based quantum networks with single atoms and optical photons”, *Rev. Mod. Phys.*, **87**, 1379 (2015) (cit. on pp. 2, 5, 8, 12, 15).

[53] E. Deist, J. A. Gerber, Y.-H. Lu, J. Zeiher, and D. M. Stamper-Kurn, “Superresolution Microscopy of Optical Fields Using Tweezer-Trapped Single Atoms”, *Phys. Rev. Lett.*, **128**, 083201 (2022) (cit. on pp. 2, 19, 36, 50, 52, 56, 57, 63–65, 67–70, 76, 98, 114).

[54] E. Deist, Y.-H. Lu, J. Ho, M. K. Pasha, J. Zeiher, Z. Yan, and D. M. Stamper-Kurn, “Mid-Circuit Cavity Measurement in a Neutral Atom Array”, *Phys. Rev. Lett.*, **129**, 203602 (2022) (cit. on pp. 2, 9, 26, 42, 51–53, 55, 56, 71, 72, 84, 85, 96–99, 121).

[55] T. Wilk, S. C. Webster, A. Kuhn, and G. Rempe, "Single-Atom Single-Photon Quantum Interface", *Science*, **317**, 488 (2007) (cit. on p. 5).

[56] A. D. Boozer, A. Boca, R. Miller, T. E. Northup, and H. J. Kimble, "Reversible State Transfer between Light and a Single Trapped Atom", *Phys. Rev. Lett.*, **98**, 193601 (2007) (cit. on p. 5).

[57] B. Weber, H. P. Specht, T. Müller, J. Bochmann, M. Mücke, D. L. Moehring, and G. Rempe, "Photon-Photon Entanglement with a Single Trapped Atom", *Phys. Rev. Lett.*, **102**, 030501 (2009) (cit. on p. 5).

[58] A. Stute, B. Casabone, P. Schindler, T. Monz, P. O. Schmidt, B. Brandstätter, T. E. Northup, and R. Blatt, "Tunable ion–photon entanglement in an optical cavity", *Nature*, **485**, 482 (2012) (cit. on p. 5).

[59] S. Ritter, C. Nölleke, C. Hahn, A. Reiserer, A. Neuzner, M. Uphoff, M. Mücke, E. Figueroa, J. Bochmann, and G. Rempe, "An elementary quantum network of single atoms in optical cavities", *Nature*, **484**, 195 (2012) (cit. on p. 5).

[60] H. J. Kimble, "The quantum internet", *Nature*, **453**, 1023 (2008) (cit. on p. 5).

[61] N. Spethmann, J. Kohler, S. Schreppler, L. Buchmann, and D. M. Stamper-Kurn, "Cavity-mediated coupling of mechanical oscillators limited by quantum back-action", *Nat. Phys.*, **12**, 27 (2015) (cit. on pp. 5, 38).

[62] J. Kohler, J. A. Gerber, E. Dowd, and D. M. Stamper-Kurn, "Negative-Mass Instability of the Spin and Motion of an Atomic Gas Driven by Optical Cavity Backaction", *Phys. Rev. Lett.*, **120**, 013601 (2018) (cit. on pp. 5, 38).

[63] I. D. Leroux, M. H. Schleier-Smith, and V. Vuletić, "Implementation of Cavity Squeezing of a Collective Atomic Spin", *Phys. Rev. Lett.*, **104**, 073602 (2010) (cit. on p. 5).

[64] E. Davis, G. Bentsen, and M. Schleier-Smith, "Approaching the Heisenberg Limit without Single-Particle Detection", *Phys. Rev. Lett.*, **116**, 053601 (2016) (cit. on p. 5).

[65] A. Sinatra, "Spin-squeezed states for metrology", *Appl. Phys. Lett.*, **120**, 120501 (2022) (cit. on p. 5).

[66] K. Baumann, C. Guerlin, F. Brennecke, and T. Esslinger, "Dicke quantum phase transition with a superfluid gas in an optical cavity", *Nature*, **464**, 1301 (2010) (cit. on p. 5).

[67] D. E. Chang, J. I. Cirac, and H. J. Kimble, "Self-Organization of Atoms along a Nanophotonic Waveguide", *Phys. Rev. Lett.*, **110**, 113606 (2013) (cit. on p. 5).

[68] J. Léonard, A. Morales, P. Zupancic, T. Esslinger, and T. Donner, "Supersolid formation in a quantum gas breaking a continuous translational symmetry", *Nature*, **543**, 87 (2017) (cit. on pp. 5, 9).

[69] A. J. Kollár, A. T. Papageorge, V. D. Vaidya, Y. Guo, J. Keeling, and B. L. Lev, "Supermode-density-wave-polariton condensation with a Bose–Einstein condensate in a multimode cavity", *Nat. Commun.*, **8**, 1 (2017) (cit. on p. 5).

[70] F. Mivehvar, F. Piazza, T. Donner, and H. Ritsch, "Cavity QED with quantum gases: new paradigms in many-body physics", *Adv. Phys.*, **70**, 1 (2021) (cit. on pp. 5, 8, 10).

[71] M. A. Nielsen and I. L. Chuang, *Quantum Computation and Quantum Information* (Cambridge University Press, 2000) (cit. on p. 6).

[72] E. J. Davis, G. Bentsen, L. Homeier, T. Li, and M. H. Schleier-Smith, "Photon-Mediated Spin-Exchange Dynamics of Spin-1 Atoms", *Phys. Rev. Lett.*, **122**, 010405 (2019) (cit. on pp. 8, 9, 17, 24, 58).

[73] S. J. Masson, M. D. Barrett, and S. Parkins, "Cavity QED Engineering of Spin Dynamics and Squeezing in a Spinor Gas", *Phys. Rev. Lett.*, **119**, 213601 (2017) (cit. on p. 8).

[74] C. Tabares, E. Zohar, and A. González-Tudela, "Tunable photon-mediated interactions between spin-1 systems", *Phys. Rev. A*, **106**, 033705 (2022) (cit. on p. 8).

[75] B. Casabone, A. Stute, K. Friebe, B. Brandstätter, K. Schüppert, R. Blatt, and T. E. Northup, "Heralded Entanglement of Two Ions in an Optical Cavity", *Phys. Rev. Lett.*, **111**, 100505 (2013) (cit. on p. 8).

[76] R. Reimann, W. Alt, T. Kampschulte, T. Macha, L. Ratschbacher, N. Thau, S. Yoon, and D. Meschede, "Cavity-Modified Collective Rayleigh Scattering of Two Atoms", *Phys. Rev. Lett.*, **114**, 023601 (2015) (cit. on pp. 8, 82).

[77] S. Welte, B. Hacker, S. Daiss, S. Ritter, and G. Rempe, "Cavity Carving of Atomic Bell States", *Phys. Rev. Lett.*, **118**, 210503 (2017) (cit. on pp. 8, 10).

[78] S. Langenfeld, O. Morin, M. Körber, and G. Rempe, "A network-ready random-access qubits memory", *NPJ Quantum Inf.*, **6**, 1 (2020) (cit. on p. 8).

[79] T. Dordevic, P. Samutpraphoot, P. L. Ocola, H. Bernien, B. Grinkemeyer, I. Dimitrova, V. Vuletić, and M. D. Lukin, "Entanglement transport and a nanophotonic interface for atoms in optical tweezers", *Science*, **373**, 1511 (2021) (cit. on pp. 8, 9, 71).

[80] Y. Liu, Z. Wang, P. Yang, Q. Wang, Q. Fan, G. Li, P. Zhang, and T. Zhang, "Realization of strong coupling between deterministic single-atom arrays and a high-finesse miniature optical cavity", *arXiv.2207.04371*, (2022) (cit. on pp. 8, 17, 97).

[81] V. D. Vaidya, Y. Guo, R. M. Kroeze, K. E. Ballantine, A. J. Kollár, J. Keeling, and B. L. Lev, "Tunable-Range, Photon-Mediated Atomic Interactions in Multimode Cavity QED", *Phys. Rev. X*, **8**, 011002 (2018) (cit. on p. 8).

[82] E. J. Davis, "Engineering and Imaging Nonlocal Spin Dynamics in an Optical Cavity", PhD thesis (Stanford University, 2020) (cit. on pp. 8, 18).

[83] A. Periwal, E. S. Cooper, P. Kunkel, J. F. Wienand, E. J. Davis, and M. Schleier-Smith, "Programmable interactions and emergent geometry in an array of atom clouds", *Nature*, **600**, 630 (2021) (cit. on p. 9).

[84] S. Gopalakrishnan, B. L. Lev, and P. M. Goldbart, “Frustration and Glassiness in Spin Models with Cavity-Mediated Interactions”, *Phys. Rev. Lett.*, **107**, 277201 (2011) (cit. on p. 9).

[85] G. Bentsen, T. Hashizume, A. S. Buyskikh, E. J. Davis, A. J. Daley, S. S. Gubser, and M. Schleier-Smith, “Treelike Interactions and Fast Scrambling with Cold Atoms”, *Phys. Rev. Lett.*, **123**, 130601 (2019) (cit. on p. 9).

[86] K. W. Murch, K. L. Moore, S. Gupta, and D. M. Stamper-Kurn, “Observation of quantum-measurement backaction with an ultracold atomic gas”, *Nat. Phys.*, **4**, 561 (2008) (cit. on p. 9).

[87] T. P. Purdy, D. W. C. Brooks, T. Botter, N. Brahms, Z.-Y. Ma, and D. M. Stamper-Kurn, “Tunable Cavity Optomechanics with Ultracold Atoms”, *Phys. Rev. Lett.*, **105**, 133602 (2010) (cit. on pp. 9, 15, 17, 18, 59, 97).

[88] S. Welte, B. Hacker, S. Daiss, S. Ritter, and G. Rempe, “Photon-Mediated Quantum Gate between Two Neutral Atoms in an Optical Cavity”, *Phys. Rev. X*, **8**, 011018 (2018) (cit. on p. 9).

[89] J. Gallego, W. Alt, T. Macha, M. Martinez-Dorantes, D. Pandey, and D. Meschede, “Strong Purcell Effect on a Neutral Atom Trapped in an Open Fiber Cavity”, *Phys. Rev. Lett.*, **121**, 173603 (2018) (cit. on pp. 9, 71, 72, 74, 75, 82).

[90] Y. Colombe, T. Steinmetz, G. Dubois, F. Linke, D. Hunger, and J. Reichel, “Strong atom–field coupling for Bose–Einstein condensates in an optical cavity on a chip”, *Nature*, **450**, 272 (2007) (cit. on p. 9).

[91] P. Samutpraphoot, T. Dordević, P. L. Ocola, H. Bernien, C. Senko, V. Vuletić, and M. D. Lukin, “Strong Coupling of Two Individually Controlled Atoms via a Nanophotonic Cavity”, *Phys. Rev. Lett.*, **124**, 063602 (2020) (cit. on p. 9).

[92] X. Luan, J.-B. Béguin, A. P. Burgers, Z. Qin, S.-P. Yu, and H. J. Kimble, “The Integration of Photonic Crystal Waveguides with Atom Arrays in Optical Tweezers”, *Adv. Quantum Technol.*, **3**, 2000008 (2020) (cit. on p. 9).

[93] I. S. Madjarov, J. P. Covey, A. L. Shaw, J. Choi, A. Kale, A. Cooper, H. Pichler, V. Schkolnik, J. R. Williams, and M. Endres, “High-fidelity entanglement and detection of alkaline-earth Rydberg atoms”, *Nat. Phys.*, **16**, 857 (2020) (cit. on pp. 9, 71).

[94] A. M. Kaufman, B. J. Lester, M. Foss-Feig, M. L. Wall, A. M. Rey, and C. A. Regal, “Entangling two transportable neutral atoms via local spin exchange”, *Nature*, **527**, 208 (2015) (cit. on p. 9).

[95] Y. Wang, A. Kumar, T.-Y. Wu, and D. S. Weiss, “Single-qubit gates based on targeted phase shifts in a 3D neutral atom array”, *Science*, **352**, 1562 (2016) (cit. on p. 9).

[96] J. Bochmann, M. Mücke, C. Guhl, S. Ritter, G. Rempe, and D. L. Moehring, “Lossless State Detection of Single Neutral Atoms”, *Phys. Rev. Lett.*, **104**, 203601 (2010) (cit. on pp. 9, 71, 72, 75, 93).

[97] R. Gehr, J. Volz, G. Dubois, T. Steinmetz, Y. Colombe, B. L. Lev, R. Long, J. Estève, and J. Reichel, "Cavity-Based Single Atom Preparation and High-Fidelity Hyperfine State Readout", *Phys. Rev. Lett.*, **104**, 203602 (2010) (cit. on pp. 9, 71).

[98] P. W. Shor, "Scheme for reducing decoherence in quantum computer memory", *Phys. Rev. A*, **52**, R2493 (1995) (cit. on pp. 10, 71).

[99] A. M. Steane, "Error Correcting Codes in Quantum Theory", *Phys. Rev. Lett.*, **77**, 793 (1996) (cit. on pp. 10, 71).

[100] E. M. Kessler, I. Lovchinsky, A. O. Sushkov, and M. D. Lukin, "Quantum error correction for metrology", *Phys. Rev. Lett.*, **112**, 150802 (2014) (cit. on pp. 10, 71).

[101] W. Dür, M. Skotiniotis, F. Fröwis, and B. Kraus, "Improved quantum metrology using quantum error correction", *Phys. Rev. Lett.*, **112**, 080801 (2014) (cit. on pp. 10, 71).

[102] S. Zhou and L. Jiang, "Optimal approximate quantum error correction for quantum metrology", *Phys. Rev. Res.*, **2**, 013235 (2020) (cit. on pp. 10, 71).

[103] R. Raussendorf and H. J. Briegel, "A One-Way Quantum Computer", *Phys. Rev. Lett.*, **86**, 5188 (2001) (cit. on p. 10).

[104] R. Raussendorf, D. Browne, and H. Briegel, "The one-way quantum computer–a non-network model of quantum computation", *J. Mod. Opt.*, **49**, 1299 (2002) (cit. on p. 10).

[105] M. A. Nielsen, "Cluster-state quantum computation", *Rep. Math. Phys.*, **57**, 147 (2006) (cit. on p. 10).

[106] F. Haas, J. Volz, R. Gehr, J. Reichel, and J. Estève, "Entangled States of More Than 40 Atoms in an Optical Fiber Cavity", *Science*, **344**, 180 (2014) (cit. on p. 10).

[107] R. McConnell, H. Zhang, J. Hu, S. Cuk, and V. Vuletić, "Entanglement with negative Wigner function of almost 3,000 atoms heralded by one photon", *Nature*, **519**, 439 (2015) (cit. on p. 10).

[108] E. J. Davis, Z. Wang, A. H. Safavi-Naeini, and M. H. Schleier-Smith, "Painting Nonclassical States of Spin or Motion with Shaped Single Photons", *Phys. Rev. Lett.*, **121**, 123602 (2018) (cit. on p. 10).

[109] S. J. Masson and S. Parkins, "Rapid Production of Many-Body Entanglement in Spin-1 Atoms via Cavity Output Photon Counting", *Phys. Rev. Lett.*, **122**, 103601 (2019) (cit. on p. 10).

[110] W. Chen, J. Hu, Y. Duan, B. Braverman, H. Zhang, and V. Vuletić, "Carving Complex Many-Atom Entangled States by Single-Photon Detection", *Phys. Rev. Lett.*, **115**, 250502 (2015) (cit. on p. 10).

[111] G. Barontini, L. Hohmann, F. Haas, J. Estève, and J. Reichel, "Deterministic generation of multiparticle entanglement by quantum Zeno dynamics", *Science*, **349**, 1317 (2015) (cit. on p. 10).

[112] G. Mazzucchi, S. F. Caballero-Benitez, and I. B. Mekhov, "Quantum measurement-induced antiferromagnetic order and density modulations in ultracold fermi gases in optical lattices", *Sci. Rep.*, **6**, 1 (2016) (cit. on p. 10).

[113] Y. Li, X. Chen, and M. P. A. Fisher, "Quantum Zeno effect and the many-body entanglement transition", *Phys. Rev. B*, **98**, 205136 (2018) (cit. on p. 10).

[114] B. Skinner, J. Ruhman, and A. Nahum, "Measurement-Induced Phase Transitions in the Dynamics of Entanglement", *Phys. Rev. X*, **9**, 031009 (2019) (cit. on p. 10).

[115] A. Nahum, S. Roy, B. Skinner, and J. Ruhman, "Measurement and Entanglement Phase Transitions in All-To-All Quantum Circuits, on Quantum Trees, and in Landau-Ginsburg Theory", *PRX Quantum*, **2**, 010352 (2021) (cit. on p. 10).

[116] I. B. Mekhov and H. Ritsch, "Quantum optics with ultracold quantum gases: towards the full quantum regime of the light–matter interaction", *J. Phys. B: At. Mol. Opt. Phys.*, **45**, 102001 (2012) (cit. on p. 10).

[117] J. S. Douglas, H. Habibian, C. L. Hung, A. V. Gorshkov, H. J. Kimble, and D. E. Chang, "Quantum many-body models with cold atoms coupled to photonic crystals", *Nat. Photon.*, **9**, 326 (2015) (cit. on p. 10).

[118] D. A. Steck, *Quantum and Atom Optics* (2007) (cit. on p. 11).

[119] R. Loudon, *The quantum theory of light* (Oxford University Press, 2000) (cit. on p. 11).

[120] D. Meschede, H. Walther, and G. Müller, "One-Atom Maser", *Phys. Rev. Lett.*, **54**, 551 (1985) (cit. on p. 12).

[121] G. Rempe, H. Walther, and N. Klein, "Observation of quantum collapse and revival in a one-atom maser", *Phys. Rev. Lett.*, **58**, 353 (1987) (cit. on p. 12).

[122] J. M. Raimond, M. Brune, and S. Haroche, "Manipulating quantum entanglement with atoms and photons in a cavity", *Rev. Mod. Phys.*, **73**, 565 (2001) (cit. on p. 12).

[123] D. Hunger, T. Steinmetz, Y. Colombe, C. Deutsch, T. W. Hänsch, and J. Reichel, "A fiber Fabry–Perot cavity with high finesse", *New J. Phys.*, **12**, 065038 (2010) (cit. on p. 14).

[124] D. Hunger, C. Deutsch, R. J. Barbour, R. J. Warburton, and J. Reichel, "Laser micro-fabrication of concave, low-roughness features in silica", *AIP Adv.*, **2**, 012119 (2012) (cit. on p. 14).

[125] K. Ott, S. Garcia, R. Kohlhaas, K. Schüppert, P. Rosenbusch, R. Long, and J. Reichel, "Millimeter-long fiber Fabry-Perot cavities", *Opt. Express*, **24**, 9839 (2016) (cit. on pp. 14, 17).

[126] H. Pfeifer, L. Ratschbacher, J. Gallego, C. Saavedra, A. Faßbender, A. von Haaren, W. Alt, S. Hofferberth, M. Köhl, S. Linden, and D. Meschede, "Achievements and perspectives of optical fiber Fabry–Perot cavities", *Appl. Phys. B*, **128**, 1 (2022) (cit. on pp. 14, 17).

[127] J. A. Gerber, "Cavity Quantum Electrodynamics with a Locally Addressable Quantum Gas", PhD thesis (University of California Berkeley, 2020) (cit. on pp. 15, 18–20, 24, 26, 32, 33, 38, 58, 76).

[128] C. Weitenberg, "Single-Atom Resolved Imaging and Manipulation in an Atomic Mott Insulator", PhD thesis (Ludwig-Maximilians-Universität München, 2011) (cit. on pp. 17, 66).

[129] J. Kohler, "Optodynamical Measurement and Coupling of Atomic Motion and Spin", PhD thesis (University of California Berkeley, 2018) (cit. on pp. 17, 18).

[130] H. Takahashi, J. Morphew, F. Oručević, A. Noguchi, E. Kassa, and M. Keller, "Novel laser machining of optical fibers for long cavities with low birefringence", *Opt. Express*, **22**, 31317 (2014) (cit. on p. 17).

[131] D. A. Steck, "Rubidium 87 D Line Data", (2021) (cit. on p. 19).

[132] C. H. Nguyen, A. N. Utama, N. Lewty, and C. Kurtsiefer, "Operating a near-concentric cavity at the last stable resonance", *Phys. Rev. A*, **98**, 063833 (2018) (cit. on p. 18).

[133] J. Lee, G. Vrijsen, I. Teper, O. Hosten, and M. A. Kasevich, "Many-atom-cavity QED system with homogeneous atom-cavity coupling", *Opt. Lett.*, **39**, 4005 (2014) (cit. on pp. 24, 58).

[134] J. Léonard, M. Lee, A. Morales, T. M. Karg, T. Esslinger, and T. Donner, "Optical transport and manipulation of an ultracold atomic cloud using focus-tunable lenses", *New J. Phys.*, **16**, 093028 (2014) (cit. on pp. 29, 30).

[135] J. Zeiher, "Realization of Rydberg-dressed quantum magnets", PhD thesis (Ludwig-Maximilians-Universität München, 2017) (cit. on p. 33).

[136] S. Schreppler, N. Spethmann, N. Brahms, T. Botter, M. Barrios, and D. M. Stamper-Kurn, "Optically measuring force near the standard quantum limit", *Science*, **344**, 1486 (2014) (cit. on p. 38).

[137] S. Kuhr, W. Alt, D. Schrader, I. Dotsenko, Y. Miroshnychenko, A. Rauschenbeutel, and D. Meschede, "Analysis of dephasing mechanisms in a standing-wave dipole trap", *Phys. Rev. A*, **72**, 023406 (2005) (cit. on p. 55).

[138] A. Lengwenus, J. Kruse, M. Volk, W. Ertmer, and G. Birkl, "Coherent manipulation of atomic qubits in optical micropotentials", *Appl. Phys. B*, **86**, 377 (2006) (cit. on p. 55).

[139] M. P. A. Jones, J. Beugnon, A. Gaëtan, J. Zhang, G. Messin, A. Browaeys, and P. Grangier, "Fast quantum state control of a single trapped neutral atom", *Phys. Rev. A*, **75**, 040301 (2007) (cit. on p. 55).

[140] U. Fano, "Ionization yield of radiations. ii. the fluctuations of the number of ions", *Phys. Rev.*, **72**, 26 (1947) (cit. on p. 62).

[141] A. van Houselt and H. J. W. Zandvliet, "Colloquium: Time-resolved scanning tunneling microscopy", *Rev. Mod. Phys.*, **82**, 1593 (2010) (cit. on p. 63).

[142] K. Bian, C. Gerber, A. J. Heinrich, D. J. Müller, S. Scheuring, and Y. Jiang, “Scanning probe microscopy”, *Nat. Rev. Methods Primers*, **1**, 1 (2021) (cit. on p. 63).

[143] I. Bloch, J. Dalibard, and W. Zwerger, “Many-body physics with ultracold gases”, *Rev. Mod. Phys.*, **80**, 885 (2008) (cit. on p. 67).

[144] C. Tuchendler, A. M. Lance, A. Browaeys, Y. R. P. Sortais, and P. Grangier, “Energy distribution and cooling of a single atom in an optical tweezer”, *Phys. Rev. A*, **78**, 033425 (2008) (cit. on p. 67).

[145] R. Grimm, M. Weidemüller, and Y. B. Ovchinnikov, “Optical Dipole Traps for Neutral Atoms”, *Adv. At. Mol. Opt. Phys.*, **42**, 95 (2000) (cit. on p. 68).

[146] S. Ebadi, T. T. Wang, H. Levine, A. Keesling, G. Semeghini, A. Omran, D. Bluvstein, R. Samajdar, H. Pichler, W. W. Ho, S. Choi, S. Sachdev, M. Greiner, V. Vuletić, and M. D. Lukin, “Quantum phases of matter on a 256-atom programmable quantum simulator”, *Nature*, **595**, 227 (2021) (cit. on p. 71).

[147] P. Scholl, M. Schuler, H. J. Williams, A. A. Eberharter, D. Barredo, K.-N. Schymik, V. Lienhard, L.-P. Henry, T. C. Lang, T. Lahaye, A. M. Läuchli, and A. Browaeys, “Quantum simulation of 2D antiferromagnets with hundreds of Rydberg atoms”, *Nature*, **595**, 233 (2021) (cit. on p. 71).

[148] D. Bluvstein, A. Omran, H. Levine, A. Keesling, G. Semeghini, S. Ebadi, T. T. Wang, A. A. Michailidis, N. Maskara, W. W. Ho, S. Choi, M. Serbyn, M. Greiner, V. Vuletić, and M. D. Lukin, “Controlling quantum many-body dynamics in driven Rydberg atom arrays”, *Science*, **371**, 1355 (2021) (cit. on p. 71).

[149] A. W. Young, W. J. Eckner, W. R. Milner, D. Kedar, M. A. Norcia, E. Oelker, N. Schine, J. Ye, and A. M. Kaufman, “Half-minute-scale atomic coherence and high relative stability in a tweezer clock”, *Nature*, **588**, 408 (2020) (cit. on pp. 71, 98).

[150] N. Schine, A. W. Young, W. J. Eckner, M. J. Martin, and A. M. Kaufman, “Long-lived Bell states in an array of optical clock qubits”, *Nat. Phys.*, **18**, 1067 (2022) (cit. on p. 71).

[151] E. Dennis, A. Kitaev, A. Landahl, and J. Preskill, “Topological quantum memory”, *J. Math. Phys.*, **43**, 4452 (2002) (cit. on p. 72).

[152] R. Raussendorf and J. Harrington, “Fault-Tolerant Quantum Computation with High Threshold in Two Dimensions”, *Phys. Rev. Lett.*, **98**, 190504 (2007) (cit. on p. 72).

[153] A. G. Fowler, M. Mariantoni, J. M. Martinis, and A. N. Cleland, “Surface codes: Towards practical large-scale quantum computation”, *Phys. Rev. A*, **86**, 032324 (2012) (cit. on p. 72).

[154] S. Nußmann, “Kühlen und positionieren eines atoms in einem optischen resonator”, Dissertation (Technische Universität München, 2006) (cit. on p. 72).

[155] J. Johansson, P. Nation, and F. Nori, "QuTiP 2: A Python framework for the dynamics of open quantum systems", *Comput. Phys. Commun.*, **184**, 1234 (2013) (cit. on pp. 75, 86, 129).

[156] M. Fox and D. Fox, *Quantum Optics: An Introduction*, Oxford Master Series in Physics (OUP Oxford, 2006) (cit. on p. 81).

[157] A. Kuhn, M. Hennrich, and G. Rempe, "Deterministic Single-Photon Source for Distributed Quantum Networking", *Phys. Rev. Lett.*, **89**, 067901 (2002) (cit. on p. 81).

[158] K. M. Birnbaum, A. Boca, R. Miller, A. D. Boozer, T. E. Northup, and H. J. Kimble, "Photon blockade in an optical cavity with one trapped atom", *Nature*, **436**, 87 (2005) (cit. on pp. 81, 82).

[159] M. Mücke, J. Bochmann, C. Hahn, A. Neuzner, C. Nölleke, A. Reiserer, G. Rempe, and S. Ritter, "Generation of single photons from an atom-cavity system", *Phys. Rev. A*, **87**, 063805 (2013) (cit. on p. 81).

[160] D. B. Higginbottom, L. Slodička, G. Araneda, L. Lachman, R. Filip, M. Hennrich, and R. Blatt, "Pure single photons from a trapped atom source", *New J. Phys.*, **18**, 093038 (2016) (cit. on p. 81).

[161] C. Hamsen, K. N. Tolazzi, T. Wilk, and G. Rempe, "Two-Photon Blockade in an Atom-Driven Cavity QED System", *Phys. Rev. Lett.*, **118**, 133604 (2017) (cit. on pp. 81, 82).

[162] F. Diedrich and H. Walther, "Nonclassical radiation of a single stored ion", *Phys. Rev. Lett.*, **58**, 203 (1987) (cit. on p. 82).

[163] V. Gomer, F. Strauch, B. Ueberholz, S. Knappe, and D. Meschede, "Single-atom dynamics revealed by photon correlations", *Phys. Rev. A*, **58**, R1657 (1998) (cit. on p. 82).

[164] P. Münstermann, T. Fischer, P. Maunz, P. W. H. Pinkse, and G. Rempe, "Dynamics of Single-Atom Motion Observed in a High-Finesse Cavity", *Phys. Rev. Lett.*, **82**, 3791 (1999) (cit. on p. 82).

[165] P. W. H. Pinkse, T. Fischer, P. Maunz, and G. Rempe, "Feedback Cooling of a Single Neutral Atom", *Nature*, **404**, 365 (2000) (cit. on p. 82).

[166] M. Koch, C. Sames, A. Kubanek, M. Apel, M. Balbach, A. Ourjoumtsev, P. W. H. Pinkse, and G. Rempe, "Feedback Cooling of a Single Neutral Atom", *Phys. Rev. Lett.*, **105**, 173003 (2010) (cit. on p. 82).

[167] P. M. Alsing, D. A. Cardimona, and H. J. Carmichael, "Suppression of fluorescence in a lossless cavity", *Phys. Rev. A*, **45**, 1793 (1992) (cit. on p. 82).

[168] H. Tanji-Suzuki, I. D. Leroux, M. H. Schleier-Smith, M. Cetina, A. T. Grier, J. Simon, and V. Vuletić, "Interaction between Atomic Ensembles and Optical Resonators: Classical Description", *Adv. At. Mol. Opt. Phys.*, **60**, 201 (2011) (cit. on pp. 82, 85).

[169] T. G. Ballance, H. M. Meyer, P. Kobel, K. Ott, J. Reichel, and M. Köhl, "Cavity-induced backaction in Purcell-enhanced photon emission of a single ion in an ultraviolet fiber cavity", *Phys. Rev. A*, **95**, 033812 (2017) (cit. on p. 82).

[170] J. Eschner, C. Raab, F. Schmidt-Kaler, and R. Blatt, "Light interference from single atoms and their mirror images", *Nature*, **413**, 495 (2001) (cit. on p. 82).

[171] U. Dorner and P. Zoller, "Laser-driven atoms in half-cavities", *Phys. Rev. A*, **66**, 023816 (2002) (cit. on p. 82).

[172] G. Hétet, L. Slodička, M. Hennrich, and R. Blatt, "Single Atom as a Mirror of an Optical Cavity", *Phys. Rev. Lett.*, **107**, 133002 (2011) (cit. on p. 82).

[173] P. Horak, G. Hechenblaikner, K. M. Gheri, H. Stecher, and H. Ritsch, "Cavity-Induced Atom Cooling in the Strong Coupling Regime", *Phys. Rev. Lett.*, **79**, 4974 (1997) (cit. on p. 84).

[174] G. Hechenblaikner, M. Gangl, P. Horak, and H. Ritsch, "Cooling an atom in a weakly driven high-Q cavity", *Phys. Rev. A*, **58**, 3030 (1998) (cit. on pp. 84, 93, 94).

[175] V. Vuletić and S. Chu, "Laser Cooling of Atoms, Ions, or Molecules by Coherent Scattering", *Phys. Rev. Lett.*, **84**, 3787 (2000) (cit. on p. 84).

[176] P. Maunz, T. Puppe, I. Schuster, N. Syassen, P. W. Pinkse, and G. Rempe, "Cavity cooling of a single atom", *Nature*, **428**, 50 (2004) (cit. on pp. 84, 95).

[177] S. Nuszmann, K. Murr, M. Hijlkema, B. Weber, A. Kuhn, and G. Rempe, "Vacuum-stimulated cooling of single atoms in three dimensions", *Nat. Phys.*, **1**, 122 (2005) (cit. on pp. 84, 95).

[178] K. Murr, S. Nußmann, T. Puppe, M. Hijlkema, B. Weber, S. C. Webster, A. Kuhn, and G. Rempe, "Three-dimensional cavity cooling and trapping in an optical lattice", *Phys. Rev. A*, **73**, 063415 (2006) (cit. on pp. 84, 95).

[179] M. Hosseini, Y. Duan, K. M. Beck, Y.-T. Chen, and V. Vuletić, "Cavity Cooling of Many Atoms", *Phys. Rev. Lett.*, **118**, 183601 (2017) (cit. on pp. 84, 95).

[180] B. R. Mollow, "Power spectrum of light scattered by two-level systems", *Phys. Rev.*, **188**, 1969 (1969) (cit. on p. 85).

[181] H. J. Kimble and L. Mandel, "Theory of resonance fluorescence", *Phys. Rev. A*, **13**, 2123 (1976) (cit. on p. 85).

[182] R. E. Grove, F. Y. Wu, and S. Ezekiel, "Measurement of the spectrum of resonance fluorescence from a two-level atom in an intense monochromatic field", *Phys. Rev. A*, **15**, 227 (1977) (cit. on p. 87).

[183] L. Ortiz-Gutiérrez, R. C. Teixeira, A. Eloy, D. F. da Silva, R. Kaiser, R. Bachelard, and M. Fouché, "Mollow triplet in cold atoms", *New J. Phys.*, **21**, 093019 (2019) (cit. on p. 87).

[184] S. Weiler, “Mollow triplet emission properties and dephasing effects in semiconductor quantum dots”, Dissertation (Universität Stuttgart, 2014) (cit. on p. 87).

[185] B. J. Sawyer, A. B. Deb, T. McKellar, and N. Kjærgaard, “Reducing number fluctuations of ultracold atomic gases via dispersive interrogation”, *Phys. Rev. A*, **86**, 065401 (2012) (cit. on p. 90).

[186] D. Yang, C. Laflamme, D. V. Vasilyev, M. A. Baranov, and P. Zoller, “Theory of a Quantum Scanning Microscope for Cold Atoms”, *Phys. Rev. Lett.*, **120**, 133601 (2018) (cit. on p. 90).

[187] J. Zeiher, J. Wolf, J. A. Isaacs, J. Kohler, and D. M. Stamper-Kurn, “Tracking Evaporative Cooling of a Mesoscopic Atomic Quantum Gas in Real Time”, *Phys. Rev. X*, **11**, 041017 (2021) (cit. on p. 90).

[188] J. Bochmann, “Coherent dynamics and state detection of single atoms in a cavity”, Dissertation (Technische Universität München, 2010) (cit. on p. 93).

[189] M. L. Terraciano, R. O. Knell, D. G. Norris, J. Jing, A. Fernández, and L. A. Orozco, “Photon burst detection of single atoms in an optical cavity”, *Nat. Phys.*, **5**, 480 (2009) (cit. on p. 97).

[190] P. Zupancic, P. M. Preiss, R. Ma, A. Lukin, M. E. Tai, M. Rispoli, R. Islam, and M. Greiner, “Ultra-precise holographic beam shaping for microscopic quantum control”, *Opt. Express*, **24**, 13881 (2016) (cit. on p. 98).

[191] E. Pedrozo-Peñafiel, S. Colombo, C. Shu, A. F. Adiyatullin, Z. Li, E. Mendez, B. Braverman, A. Kawasaki, D. Akamatsu, Y. Xiao, and V. Vuletić, “Entanglement on an optical atomic-clock transition ”, *Nature*, 414 (2020) (cit. on p. 98).

Appendix A

Superresolution Microscopy of Optical Fields Using Tweezer-Trapped Single Atoms

This appendix includes the following paper [53], discussed in Chapter 5:

- *E. Deist, J. A. Gerber, Y.-H. Lu, J. Zeiher, and D. M. Stamper-Kurn, "Superresolution Microscopy of Optical Fields Using Tweezer-Trapped Single Atoms", Phys. Rev. Lett.,* ***128****, 083201 (2022)*

PHYSICAL REVIEW LETTERS **128,** 083201 (2022)

Editors' Suggestion Featured in Physics

Superresolution Microscopy of Optical Fields Using Tweezer-Trapped Single Atoms

Emma Deist,[1,2] Justin A. Gerber,[1,2] Yue-Hui Lu,[1,2] Johannes Zeiher,[1,3,4] and Dan M. Stamper-Kurn[1,2,5,*]
[1]*Department of Physics, University of California, Berkeley, California 94720, USA*
[2]*Challenge Institute for Quantum Computation, University of California, Berkeley, California 94720, USA*
[3]*Max-Planck-Institut für Quantenoptik, 85748 Garching, Germany*
[4]*Munich Center for Quantum Science and Technology (MCQST), 80799 Munich, Germany*
[5]*Materials Sciences Division, Lawrence Berkeley National Laboratory, Berkeley, California 94720, USA*

(Received 21 September 2021; revised 11 December 2021; accepted 5 January 2022; published 22 February 2022)

We realize a scanning probe microscope using single trapped ^{87}Rb atoms to measure optical fields with subwavelength spatial resolution. Our microscope operates by detecting fluorescence from a single atom driven by near-resonant light and determining the ac Stark shift of an atomic transition from other local optical fields via the change in the fluorescence rate. We benchmark the microscope by measuring two standing-wave Gaussian modes of a Fabry-Pérot resonator with optical wavelengths of 1560 and 781 nm. We attain a spatial resolution of 300 nm, which is superresolving compared to the limit set by the 780 nm wavelength of the detected light. Sensitivity to short length scale features is enhanced by adapting the sensor to characterize an optical field via the force it exerts on the atom.

DOI: 10.1103/PhysRevLett.128.083201

Neutral atoms make excellent sensors, owing largely to the identical physical properties of all atoms of a given isotope [1]. Further, neutral atoms can be isolated from decoherence, enabling highly sensitive measurements of fields, forces, acceleration, rotation, and the passage of time [2–5]. While, to date, atomic sensors have mostly made use of gaseous atomic ensembles, new techniques allow exceptional control of single atoms [6,7] and of structured arrays of single atoms [8,9], motivated by the goals of quantum simulation [10], communication [11], metrology [12,13], and computation [14,15].

A number of techniques use cold atoms for spatial tomography of material properties and electromagnetic fields [16–21]. Complementary techniques use electromagnetic fields to perform superresolution microscopy of cold atom systems [22,23]. Here, we harness the ability to trap, position, and detect single neutral atoms to construct a scanning probe quantum sensor [24] that measures optical fields with high spatial resolution. The sensing medium is a single ^{87}Rb atom trapped within a tightly focused optical tweezer trap and driven with near-resonant light. By measuring the optical fluorescence rate, we determine the shift induced on the atomic resonance frequency by local optical fields and, thereby, the local background optical intensity. We apply our sensor to optical test patterns formed by long-wavelength (LW, 1560 nm) and short-wavelength (SW, 781 nm) TEM_{00} standing-wave modes of a Fabry-Pérot optical resonator. We measure a sensor spatial resolution of 300 nm, below the resolution limit set by the detected fluorescence light at a wavelength of 780 nm, thus achieving superresolution.

Operation of the sensor relies on basic properties of light-atom interactions. An atom in free space scatters light at a rate given by

$$\Gamma_{\mathrm{sc}} \propto \frac{1}{(\omega_L - \omega_0 - \delta_{\mathrm{ac}})^2}. \qquad (1)$$

Here, we consider the scattering of imaging light at a frequency ω_L that is near that of a single atomic transition, with the atomic resonance frequency being the sum of ω_0, the bare resonance frequency, and δ_{ac}, the transition ac Stark shift. We consider the ac Stark shift due to linearly polarized optical fields with detunings much larger than the atomic state hyperfine splittings, and thus treat the atom as a two-level system, ignoring degeneracies and optical polarization effects. We require the detuning of the imaging light to be large compared to the atomic resonance linewidth and neglect saturation by considering the weak scattering regime. The transition ac Stark shift is determined by the intensity I of a local optical field of frequency ω as $\delta_{\mathrm{ac}} = -(2\hbar c\epsilon_0)^{-1}[\alpha_e(\omega) - \alpha_g(\omega)]I$, where $\alpha_{g,e}(\omega)$ are the scalar dynamical electrical polarizabilities of the ground and excited states [25]. These polarizabilities are fixed for ^{87}Rb atoms; thus, the measurement of δ_{ac} realizes an absolutely calibrated light intensity meter.

Our sensor employs a one-dimensional array of as many as ten atoms trapped individually in optical tweezer traps. The tweezers, each formed by focusing light at a wavelength of 808 nm through a $\mathrm{NA} = 0.5$ objective to a Gaussian beam waist of around 750 nm, are located near the center of an in-vacuum, near-concentric Fabry-Pérot optical cavity, whose mirrors are coated to be highly

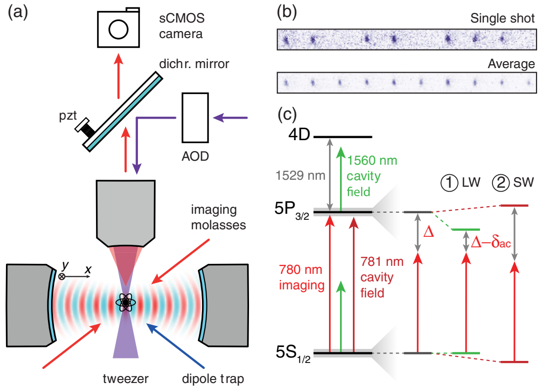

FIG. 1. Overview of the experiment. (a) Atoms are loaded from an optical dipole trap into an array of optical tweezers, centered within an optical cavity. The radial (y) position of tweezers along the array is controlled using an acousto-optical deflector (AOD), while the axial (x) position is controlled using a piezoactuated mirror. Atomic fluorescence is imaged through a $\mathrm{NA} = 0.5$ objective (used also to focus tweezer light) onto a scientific CMOS (sCMOS) camera. (b) Single-shot (top) and averaged (bottom) fluorescence images of ten-atom tweezer array. (c) ac Stark shifts are applied to the ^{87}Rb $5S_{1/2}$ to $5P_{3/2}$ imaging transition at 780 nm by light at wavelengths of 1560 nm (LW, green arrow) and 781 nm (SW, dark red arrow), both supported by the optical cavity. LW light reduces the imaging transition frequency, due to the dominant downward shift of the excited state caused by the proximity of the $5P_{3/2}$ to $4D$ transitions near 1529 nm. SW light increases the imaging transition frequency and exerts a strong potential on ground-state atoms.

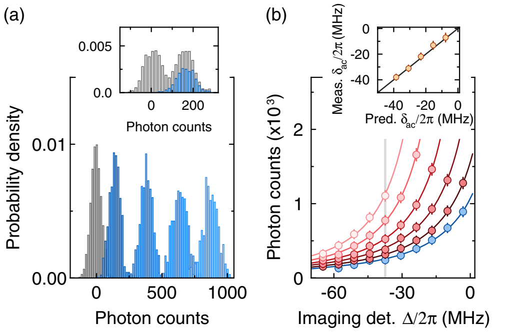

FIG. 2. Demonstration of sensor operation. (a) Background-subtracted integrated photon counts for fluorescence images (exposure 500 ms) of single atoms at imaging detunings $\Delta/2\pi = -64.8, -23.7, -10.0, -3.2$ MHz (lightening shades of blue). Near atomic resonance, single-atom fluorescence is easily distinguished from camera noise (gray), allowing us to detect an atom with 99.99% fidelity. For far-detuned probing, the photon-count distributions for zero- and one-atom images overlap ($\Delta/2\pi = -64.8$ MHz data shown together in inset, gray). However, postselection (inset, blue) based on a later near-resonant image frame identifies single-atom images. (b) Detected photon counts vs Δ for an atom held in an optical tweezer of depth $k_B \times 1.5(2)$ mK (blue) and subject to increasing intensities of LW cavity field (lightening shades of red). Error bars indicate estimated single-shot uncertainty based on photon detection noise. Solid lines are fits to Eq. (1). The inset compares δ_{ac} from LW light measured at $\Delta/2\pi = -37$ MHz [gray line in Fig. 2(b)] with a prediction that is based on the estimated cavity circulating intensity, with a correction factor of 0.7 applied to account for a reduction in the ac Stark shift measured at the LW antinode due to spatial averaging by the finite temperature atomic distribution.

reflective for LW and SW light. The array is oriented perpendicular to the cavity axis and translated along the cavity axis using a piezo-controlled mirror; see Figs. 1(a) and 1(b).

We load atoms into the tweezers by overlaying the tweezers on a large-volume optical trap containing a gas of ^{87}Rb atoms at a temperature of 30 μK. The atoms are then exposed both to counterpropagating fluorescence imaging beams, with a variable red detuning $\Delta = \omega_L - \omega_0 < 0$ from the D_2 $F = 2 \rightarrow F' = 3$ optical transition, and also to repump light resonant with the D_2 $F = 1 \rightarrow F' = 2$ transition. The dipole trap is extinguished after 10 ms. The imaging light reduces the atom number in each tweezer to either zero or one [6], cools the atoms to a thermal energy of roughly a tenth of the depth of the tweezer trap [set in the range $k_B \times (0.25\text{–}1.5)$ mK for different experiments], and generates atomic fluorescence.

The fluoresced light at a wavelength of 780 nm is imaged using the same high-resolution objective used to produce the tweezer array. In each experimental repetition, we image the same tweezer-trapped atoms in up to ten 500 ms exposures, maintaining constant imaging-light intensity while varying the detuning Δ stepwise toward atomic resonance between image frames. Single atoms fluoresce more brightly in subsequent frames, as shown in the histograms in Fig. 2(a). We postselect data in each image frame based on a photon-count threshold in a later frame to ensure the atom did not leave the trap during any earlier imaging exposure. This postselection also allows us to determine the scattering rate for atoms probed with far-detuned light for which the fluorescence level is not far above the photodetection noise floor; see Fig. 2(a) inset.

The detected photon counts provide a measure of δ_{ac}, as demonstrated in Fig. 2(b). We place a tweezer-trapped atom at the antinode of the LW cavity mode and detect atomic fluorescence at different imaging detunings Δ and linearly increasing LW cavity intensities. For each LW intensity, we fit the dataset of photon counts vs Δ to the prediction of Eq. (1) and observe good agreement with the model. As expected from the level structure of ^{87}Rb [see Fig. 1(c)], increasing LW light shifts the atomic resonance downward ($\delta_{ac} < 0$), bringing the effective imaging-light detuning $\Delta - \delta_{ac}$ closer to resonance and increasing the atomic fluorescence.

For normal sensor operation, we determine the LW-light-induced δ_{ac} from the photon counts detected at a single Δ. We convert the detected photons counts to δ_{ac} using Eq. (1) with parameters, such as the ac Stark shift due to the tweezer light, calibrated by a fit to reference data taken in absence of LW light [blue data in Fig. 2(b)]. As shown in the Fig. 2(b) inset, the measured values of δ_{ac} are consistent, to within systematic error, with our estimates of δ_{ac} based on measurements of the LW power at the cavity output, thus demonstrating the accuracy of the sensor. The uncertainty in the output power estimate of δ_{ac} is dominated by 20% uncertainty in the transmissivity of the cavity out-coupling mirror [26].

The sensitivity of a single δ_{ac} measurement is limited by photodetection noise, improving as $|\Delta - \delta_{\text{ac}}|$ decreases and the atomic scattering rate increases, until the atom is lost from the tweezer trap owing to ineffective laser cooling under imaging light that is too close to atomic resonance. The best sensor performance that we demonstrate occurs at a minimum imaging detuning of $|\Delta - \delta_{\text{ac}}| = 2\pi\times$ 30 MHz. At this setting, pure shot noise on the photon number detected from a single atom would yield an ac Stark shift measurement sensitivity of $2\pi \times 250\ \text{kHz}/\sqrt{\text{Hz}}$. In practice, read noise, background light, and additional noise due to atomic internal and motional dynamics increases the measured sensitivity to $2\pi \times 500\ \text{kHz}/\sqrt{\text{Hz}}$.

By scanning the positions of several tweezer-trapped atoms and performing a fluorescence measurement at each position, we obtain a scanning-probe image of the LW cavity mode, shown in Fig. 3. We resolve both the coarse radial variation and also the fine-scale axial variation of the standing-wave Gaussian mode. By averaging repeated axial scans of the cavity field, we identify and correct for a slow drift of the tweezer positions relative to the optical cavity of up to 800 nm.

The contrast of the observed axial variation in δ_{ac} provides a measure of the spatial resolution of our sensor. The convolution of a full-contrast sinusoidal intensity pattern of period d with a Gaussian point spread function of rms width σ yields an expected contrast of $C = e^{-\pi^2 r^2/2d^2}$, where $r = 2\sigma$ is the resolution limit according to the Sparrow criterion. The contrast achieved at various radial positions in Fig. 3(b) ranges between 0.30 and 0.47, which, with $d = 780$ nm, corresponds to r between 380 and 300 nm. For comparison, the diffraction-limited Sparrow resolution of our $\text{NA} = 0.5$ microscope is 657 nm, and the fundamental free-space far-field diffraction limit for our imaging wavelength is 328 nm. We achieve superresolution with respect to both limits. Decreasing contrast at higher cavity field intensity indicates that the temperature of the atomic sensor increases, perhaps owing to poorer laser cooling in the presence of large state- and position-dependent ac Stark shifts. Using the axially averaged values of the ac Stark shift $\bar{\delta}_{\text{ac}}$, we reproduce the radial Gaussian profile of the cavity intensity, observing a beam waist of $25.9(3)\ \mu$m, in agreement with our *a priori* estimate of 24.3 μm based on the cavity geometry [27].

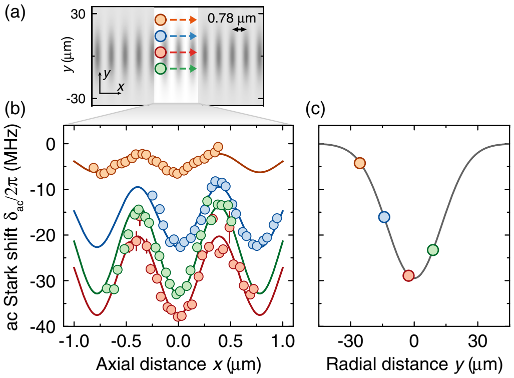

FIG. 3. Superresolution imaging of LW cavity field. (a) Several atoms trapped in tweezers of depth $k_B \times 1.5(2)$ mK are arrayed in a direction nearly perpendicular to the cavity axis, spaced to probe the cavity mode at several radial positions. The calculated intensity profile of the cavity mode is shown in gray scale. The array is translated in 100 nm steps along the cavity axis (trajectory shown). δ_{ac} is measured for each tweezer at every position along this trajectory. (b) Axial dependence of ac Stark shift measurements for four tweezers whose radial positions are indicated in (c). Modulation with a periodicity of the LW lattice ($d = 780$ nm) is clearly visible with contrasts between 0.30 and 0.47. Error bars indicate standard error on the mean of repeated measurements. (c) Radial profile of the LW TEM_{00} mode, determined from axial average $\bar{\delta}_{\text{ac}}$ of data in (b). Error bars are smaller than the data points. Solid line is a fit to a Gaussian with a waist of $25.9(3)\ \mu$m.

Next, we explore the limits of the single-atom sensor by applying it to map an optical field generated by shorter-wavelength light, the standing-wave Fabry-Pérot cavity mode at a wavelength of 781 nm, $2\pi \times 400$ GHz red-detuned from the atomic D_2 resonance. The shorter-wavelength light presents two coupled challenges to our sensing application. First, at fixed resolution, shorter-wavelength axial intensity variation with periodicity $d = 390.5$ nm is measured with lower contrast, estimated at just $C = 0.05$ for $r = 300$ nm. For our measurement times and sensitivities, this low contrast allows only relatively large ac Stark shifts to be measured. Second, large ac Stark shifts modulated at short length scales lead to strong optical forces that displace the trapped atom within the optical tweezer, complicating the interpretation of the measurement. Further, unlike the LW light, the SW light produces ac Stark shifts on the ground and excited atomic states that are comparable in magnitude, exacerbating the deflection of the ground-state atomic sensor.

We overcome these obstacles by driving the Fabry-Pérot cavity simultaneously at both its SW and LW resonances and measuring the total transition ac Stark shift provided by both optical fields. In a simplified interpretation, we use the

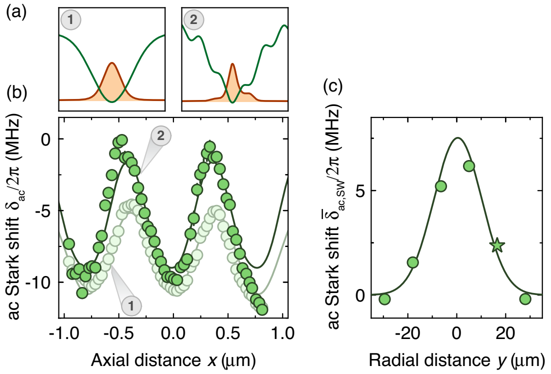

FIG. 4. Force sensing measurement of SW cavity lattice through distortion of LW measurement. (a) Optical trapping potential (green) and thermal atomic distribution (orange) due to the tweezer (left) and the sum of the tweezer and SW cavity field (right). The SW lattice narrows and displaces the atomic distribution. (b) Axial ac Stark shift due to the LW cavity field measured with a single atom trapped in a tweezer of depth $k_B \times 0.34(3)$ mK in the absence (presence) of SW light, shown in light (dark) green. The axial variation at the LW periodicity gains an overall offset, increases in amplitude, and is shifted axially upon imposition of the SW potential. Error bars indicate standard error on the mean of repeated measurements. (c) Axially-averaged offset of the LW ac Stark shift due to the SW cavity field measured at different radial positions. Solid line is a fit to a Gaussian with a waist of 20(3) μm. Starred point indicates the tweezer used for (b).

single atom now as a "force sensor": Forces and force gradients produced by the SW optical pattern displace and compress the space sampled by the trapped atom. These changes to the atomic position distribution alter the observed axial variation of δ_{ac} at the 780 nm spatial period of the LW pattern, indirectly revealing the spatial structure of the SW mode; see Fig. 4.

We note three distinct features that arise due to the SW light. First, the axial average of δ_{ac} is shifted in the positive direction by an amount $\bar{\delta}_{ac,SW}$ that is proportional to the circulating power of the SW light. The radial variation of this average shift maps out the radial profile of the SW cavity mode; see Fig. 4(c).

Second, the SW light enhances the amplitude of the LW signal. As shown in Fig. 4(a), for tweezers placed near antinodes of the SW cavity mode, the cavity-light potential adds to the tweezer confinement and reduces the size of the atomic distribution. If these antinodes overlap with the antinodes (nodes) of the LW standing wave, the narrowing of the atomic distribution increases (reduces) the magnitude of the ac Stark shift from the LW light. Altogether, the contrast of the axial variation in the ac Stark shift measurement is thereby increased, consistent with our observation.

Third, the axial modulation pattern shifts along the axis in the presence of SW light. This shift arises from an axial displacement of the SW cavity mode with respect to the LW mode, which is expected due to their noncommensurate wavelengths. We perform a fit to the data accounting for all of these effects and determine the relative displacement between the LW and SW standing waves in the sensing region to be 50(5) nm. By measuring the amplitude and spatial displacement relative to the LW field, we have fully characterized the SW optical field.

Directly mapping the spatial modes of our high-finesse optical cavity provides an excellent characterization of our system for future work in cavity QED. Complementing existing methods for measuring and controlling atom-cavity coupling [28–31], this technique demonstrates our ability to position single tweezer-trapped atoms with subwavelength accuracy for cavity-mediated readout [32–35], feedback [36,37], and entanglement [38–41]. High-resolution *in situ* measurements of ac Stark shifts could be similarly useful in free-space quantum simulators and information processors that demand ever-better control of optical potentials [42,43].

In the measurement demonstrated here, we use single-atom fluorescence on a strong allowed optical transition, measuring atomic energy shifts at the scale of the atomic linewidth (megahertz). The measurement sensitivity could be improved by reducing photon detection noise to the shot-noise limit. One could extend this technique to detect weaker signals utilizing longer-lived atomic coherences, measuring local fields through their influence on spin coherences, for example, as is done in scanning probe microscopy using nitrogen-vacancy defects in diamond [44]. The spatial resolution of this measurement could be further improved by using a more tightly localized atomic probe, achievable with a deeper tweezer trap or by implementing demonstrated single-atom cooling techniques [7,45,46]. Implementing this measurement in a state-insensitive or "magic wavelength" tweezer trap would, by eliminating the ac Stark shift due to the tweezer, enable a calibration-free measurement of the target optical field [47,48].

We thank A. Bohnett, S. Debnath, J. Ho, A. Lloyd, and R. Tsuchiyama for their assistance in the lab. We acknowledge support from the AFOSR (Grant No. FA9550-19-1-0328), from ARO through the MURI program (Grant No. W911NF-20-1-0136), and from DARPA (Grant No. W911NF2010090). E. D. and J. G. acknowledge support from the NSF Graduate Research Fellowship Program, and J. Z. acknowledges support from the Humboldt Foundation through a Feodor Lynen Fellowship.

---

[*] dmsk@berkeley.edu

[1] J. Kitching, S. Knappe, and E. A. Donley, Atomic sensors—a review, IEEE Sens. J. **11**, 1749 (2011).

[2] D. Budker and M. Romalis, Optical magnetometry, Nat. Phys. **3**, 227 (2007).

[3] S. Schreppler, N. Spethmann, N. Brahms, T. Botter, M. Barrios, and D. M. Stamper-Kurn, Optically measuring force near the standard quantum limit, Science **344**, 1486 (2014).

[4] K. Bongs, M. Holynski, J. Vovrosh, P. Bouyer, G. Condon, E. Rasel, C. Schubert, W. P. Schleich, and A. Roura, Taking atom interferometric quantum sensors from the laboratory to real-world applications, Nat. Rev. Phys. **1**, 731 (2019).

[5] A. D. Ludlow, M. M. Boyd, J. Ye, E. Peik, and P. O. Schmidt, Optical atomic clocks, Rev. Mod. Phys. **87**, 637 (2015).

[6] N. Schlosser, G. Reymond, I. Protsenko, and P. Grangier, Sub-poissonian loading of single atoms in a microscopic dipole trap, Nature (London) **411**, 1024 (2001).

[7] A. M. Kaufman, B. J. Lester, and C. A. Regal, Cooling a Single Atom in an Optical Tweezer to Its Quantum Ground State, Phys. Rev. X **2**, 041014 (2012).

[8] D. Barredo, S. D. Léséleuc, V. Lienhard, T. Lahaye, and A. Browaeys, An atom-by-atom assembler of defect-free arbitrary two-dimensional atomic arrays, Science **354**, 1021 (2016).

[9] M. Endres, H. Bernien, A. Keesling, H. Levine, E. R. Anschuetz, A. Krajenbrink, C. Senko, V. Vuletić, M. Greiner, and M. D. Lukin, Atom-by-atom assembly of defect-free one-dimensional cold atom arrays, Science **354**, 1024 (2016).

[10] A. Browaeys and T. Lahaye, Many-body physics with individually controlled Rydberg atoms, Nat. Phys. **16**, 132 (2020).

[11] A. Reiserer and G. Rempe, Cavity-based quantum networks with single atoms and optical photons, Rev. Mod. Phys. **87**, 1379 (2015).

[12] I. S. Madjarov, A. Cooper, A. L. Shaw, J. P. Covey, V. Schkolnik, T. H. Yoon, J. R. Williams, and M. Endres, An Atomic-Array Optical Clock with Single-Atom Readout, Phys. Rev. X **9**, 041052 (2019).

[13] A. W. Young, W. J. Eckner, W. R. Milner, D. Kedar, M. A. Norcia, E. Oelker, N. Schine, J. Ye, and A. M. Kaufman, Half-minute-scale atomic coherence and high relative stability in a tweezer clock, Nature (London) **588**, 408 (2020).

[14] C. Weitenberg, S. Kuhr, K. Mølmer, and J. F. Sherson, Quantum computation architecture using optical tweezers, Phys. Rev. A **84**, 032322 (2011).

[15] H. Levine, A. Keesling, G. Semeghini, A. Omran, T. T. Wang, S. Ebadi, H. Bernien, M. Greiner, V. Vuletić, H. Pichler, and M. D. Lukin, Parallel Implementation of High-Fidelity Multiqubit Gates with Neutral Atoms, Phys. Rev. Lett. **123**, 170503 (2019).

[16] G. R. Guthöhrlein, M. Keller, K. Hayasaka, W. Lange, and H. Walther, A single ion as a nanoscopic probe of an optical field, Nature (London) **414**, 49 (2001).

[17] M. Vengalattore, J. M. Higbie, S. R. Leslie, J. Guzman, L. E. Sadler, and D. M. Stamper-Kurn, High-Resolution Magnetometry with a Spinor Bose-Einstein Condensate, Phys. Rev. Lett. **98**, 200801 (2007).

[18] J. P. Brantut, J. F. Clément, M. Robert de Saint Vincent, G. Varoquaux, R. A. Nyman, A. Aspect, T. Bourdel, and P. Bouyer, Light-shift tomography in an optical-dipole trap for neutral atoms, Phys. Rev. A **78**, 031401(R) (2008).

[19] M. Gierling, P. Schneeweiss, G. Visanescu, P. Federsel, M. Häffner, D. P. Kern, T. E. Judd, A. Günther, and J. Fortágh, Cold-atom scanning probe microscopy, Nat. Nanotechnol. **6**, 446 (2011).

[20] M. Lee, J. Kim, W. Seo, H.-G. Hong, Y. Song, R. R. Dasari, and K. An, Three-dimensional imaging of cavity vacuum with single atoms localized by a nanohole array, Nat. Commun. **5**, 1 (2014).

[21] F. Yang, A. J. Kollár, S. F. Taylor, R. W. Turner, and B. L. Lev, Scanning Quantum Cryogenic Atom Microscope, Phys. Rev. Applied **7**, 034026 (2017).

[22] M. McDonald, J. Trisnadi, K.-X. Yao, and C. Chin, Superresolution Microscopy of Cold Atoms in an Optical Lattice, Phys. Rev. X **9**, 021001 (2019).

[23] S. Subhankar, Y. Wang, T.-C. Tsui, S. L. Rolston, and J. V. Porto, Nanoscale Atomic Density Microscopy, Phys. Rev. X **9**, 021002 (2019).

[24] K. Bian, C. Gerber, A. J. Heinrich, D. J. Müller, S. Scheuring, and Y. Jiang, Scanning probe microscopy, Nat. Rev. Methods Primers **1**, 1 (2021).

[25] R. Grimm, M. Weidemüller, and Y. B. Ovchinnikov, Optical dipole traps for neutral atoms, Adv. At. Mol. Opt. Phys. **42**, 95 (2000).

[26] To estimate the circulating power in the cavity, we account for 100 ppm transmissivity of the out-coupling mirror and 10% photodetection efficiency of transmitted light. The circulating power is converted to intensity via the measured mode waist [see Fig. 3(b)] and to δ_{ac} by the scalar dynamical electrical polarizability at 1560 nm.

[27] The cavity mirrors have a radius of curvature of 5 mm and the cavity length is 9.4 mm.

[28] T. P. Purdy, D. W. C. Brooks, T. Botter, N. Brahms, Z.-Y. Ma, and D. M. Stamper-Kurn, Tunable Cavity Optomechanics with Ultracold Atoms, Phys. Rev. Lett. **105**, 133602 (2010).

[29] J. Lee, G. Vrijsen, I. Teper, O. Hosten, and M. A. Kasevich, Many-atom-cavity QED system with homogeneous atom-cavity coupling, Opt. Lett. **39**, 4005 (2014).

[30] B. Wu, G. P. Greve, C. Luo, and J. K. Thompson, Site-dependent selection of atoms for homogeneous atom-cavity coupling, arXiv:2104.01201.

[31] F. Fogliano, B. Besga, A. Reigue, P. Heringlake, L. Mercier de Lépinay, C. Vaneph, J. Reichel, B. Pigeau, and O. Arcizet, Mapping the Cavity Optomechanical Interaction with Subwavelength-Sized Ultrasensitive Nanomechanical Force Sensors, Phys. Rev. X **11**, 021009 (2021).

[32] A. D. Boozer, A. Boca, R. Miller, T. E. Northup, and H. J. Kimble, Cooling to the Ground State of Axial Motion for One Atom Strongly Coupled to an Optical Cavity, Phys. Rev. Lett. **97**, 083602 (2006).

[33] M. Khudaverdyan, W. Alt, T. Kampschulte, S. Reick, A. Thobe, A. Widera, and D. Meschede, Quantum Jumps and Spin Dynamics of Interacting Atoms in a Strongly Coupled Atom-Cavity System, Phys. Rev. Lett. **103**, 123006 (2009).

[34] J. Bochmann, M. Mücke, C. Guhl, S. Ritter, G. Rempe, and D. L. Moehring, Lossless State Detection of Single Neutral Atoms, Phys. Rev. Lett. **104**, 203601 (2010).

[35] R. Gehr, J. Volz, G. Dubois, T. Steinmetz, Y. Colombe, B. L. Lev, R. Long, J. Estève, and J. Reichel, Cavity-Based Single Atom Preparation and High-Fidelity Hyperfine State Readout, Phys. Rev. Lett. **104**, 203602 (2010).

[36] W. P. Smith, J. E. Reiner, L. A. Orozco, S. Kuhr, and H. M. Wiseman, Capture and Release of a Conditional State of a Cavity QED System by Quantum Feedback, Phys. Rev. Lett. **89**, 133601 (2002).

[37] Z. K. Minev, S. O. Mundhada, S. Shankar, P. Reinhold, R. Gutiérrez-Jáuregui, R. J. Schoelkopf, M. Mirrahimi, H. J. Carmichael, and M. H. Devoret, To catch and reverse a quantum jump mid-flight, Nature (London) **570**, 200 (2019).

[38] S. Welte, B. Hacker, S. Daiss, S. Ritter, and G. Rempe, Photon-Mediated Quantum Gate between Two Neutral Atoms in an Optical Cavity, Phys. Rev. X **8**, 011018 (2018).

[39] V. D. Vaidya, Y. Guo, R. M. Kroeze, K. E. Ballantine, A. J. Kollár, J. Keeling, and B. L. Lev, Tunable-Range, Photon-Mediated Atomic Interactions in Multimode Cavity QED, Phys. Rev. X **8**, 011002 (2018).

[40] E. J. Davis, G. Bentsen, L. Homeier, T. Li, and M. H. Schleier-Smith, Photon-Mediated Spin-Exchange Dynamics of Spin-1 Atoms, Phys. Rev. Lett. **122**, 010405 (2019).

[41] P. Samutpraphoot, T. Đorđević, P. L. Ocola, H. Bernien, C. Senko, V. Vuletić, and M. D. Lukin, Strong Coupling of Two Individually Controlled Atoms via a Nanophotonic Cavity, Phys. Rev. Lett. **124**, 063602 (2020).

[42] P. Zupancic, P. M. Preiss, R. Ma, A. Lukin, M. E. Tai, M. Rispoli, R. Islam, and M. Greiner, Ultra-precise holographic beam shaping for microscopic quantum control, Opt. Express **24**, 13881 (2016).

[43] A. Heinz, J. Trautmann, N. Šantić, A. J. Park, I. Bloch, and S. Blatt, Crossed optical cavities with large mode diameters, Opt. Lett. **46**, 250 (2021).

[44] P. Maletinsky, S. Hong, M. S. Grinolds, B. Hausmann, M. D. Lukin, R. L. Walsworth, M. Loncar, and A. Yacoby, A robust scanning diamond sensor for nanoscale imaging with single nitrogen-vacancy centres, Nat. Nanotechnol. **7**, 320 (2012).

[45] J. D. Thompson, T. G. Tiecke, A. S. Zibrov, V. Vuletić, and M. D. Lukin, Coherence and Raman Sideband Cooling of a Single Atom in an Optical Tweezer, Phys. Rev. Lett. **110**, 133001 (2013).

[46] Y. Yu, N. R. Hutzler, J. T. Zhang, L. R. Liu, J. D. Hood, T. Rosenband, and K.-K. Ni, Motional-ground-state cooling outside the Lamb-Dicke regime, Phys. Rev. A **97**, 063423 (2018).

[47] B. Arora, M. S. Safronova, and C. W. Clark, State-insensitive bichromatic optical trapping, Phys. Rev. A **82**, 022509 (2010).

[48] M. M. Aliyu, L. Zhao, X. Q. Quek, K. C. Yellapragada, and H. Loh, D_1 magic wavelength tweezers for scaling atom arrays, Phys. Rev. Research **3**, 043059 (2021).

Appendix B

Mid-Circuit Cavity Measurement in a Neutral Atom Array

This appendix includes the following paper [54], discussed in Chapter 6:

- *E. Deist, Y.-H. Lu, J. Ho, M. K. Pasha, J. Zeiher, Z. Yan, and D. M. Stamper-Kurn, "Mid-Circuit Cavity Measurement in a Neutral Atom Array", Phys. Rev. Lett.,* ***129****, 203602 (2022)*

PHYSICAL REVIEW LETTERS **129,** 203602 (2022)

Mid-Circuit Cavity Measurement in a Neutral Atom Array

Emma Deist,[1,2,*] Yue-Hui Lu,[1,2,*] Jacquelyn Ho,[1,2] Mary Kate Pasha,[1,2] Johannes Zeiher,[1,3,4]
Zhenjie Yan,[1,2] and Dan M. Stamper-Kurn[1,2,5,†]
[1]*Department of Physics, University of California, Berkeley, California 94720, USA*
[2]*Challenge Institute for Quantum Computation, University of California, Berkeley, California 94720, USA*
[3]*Max-Planck-Institut für Quantenoptik, 85748 Garching, Germany*
[4]*Munich Center for Quantum Science and Technology (MCQST), 80799 Munich, Germany*
[5]*Materials Sciences Division, Lawrence Berkeley National Laboratory, Berkeley, California 94720, USA*

(Received 31 May 2022; revised 19 August 2022; accepted 5 October 2022; published 9 November 2022)

Subsystem readout during a quantum process, or mid-circuit measurement, is crucial for error correction in quantum computation, simulation, and metrology. Ideal mid-circuit measurement should be faster than the decoherence of the system, high-fidelity, and nondestructive to the unmeasured qubits. Here, we use a strongly coupled optical cavity to read out the state of a single tweezer-trapped ^{87}Rb atom within a small tweezer array. Measuring either atomic fluorescence or the transmission of light through the cavity, we detect both the presence and the state of an atom in the tweezer, within only tens of microseconds, with state preparation and measurement infidelities of roughly 0.5% and atom loss probabilities of around 1%. Using a two-tweezer system, we find measurement on one atom within the cavity causes no observable hyperfine-state decoherence on a second atom located tens of microns from the cavity volume. This high-fidelity mid-circuit readout method is a substantial step toward quantum error correction in neutral atom arrays.

DOI: 10.1103/PhysRevLett.129.203602

Numerous applications of controlled many-body quantum systems require measurements that read out and affect only a part of the system, i.e., mid-circuit measurements. Examples include quantum error correction [1,2], measurement-based quantum computation [3], quantum-error-corrected metrology [4–6], and an entanglement phase transition induced by mid-circuit measurements on a quantum circuit [7,8]. Effective mid-circuit measurements should satisfy three requirements: they must be faster than the decoherence rate of the system, have low error rates (e.g., below around 1% for implementing surface-code quantum error correction [9–11]), and be sufficiently local so as not to disturb unmeasured quantum bits.

In atom-based systems such as atom-tweezer arrays [12,13], lattice-trapped atoms [14,15], and trapped ion chains [16], the many-atom state is often read out through optical fluorescence imaging. Practical limitations on the numerical aperture (NA) of imaging systems require many photons to be scattered by an atom before it is detected. This requirement impairs the use of free-space imaging for mid-circuit measurement: Measurements tend to be slow (e.g., on the order of 10 [17–21] or 100 ms [22] in atomic tweezer arrays and quantum gas microscopes, respectively [23]), of limited state-detection fidelity owing to spontaneous Raman transitions during detection, and destructive to nearby atoms that can absorb scattered photons.

Here, we demonstrate mid-circuit optical detection of an atomic tweezer array wherein a single atom is measured with high fidelity while the remaining array retains quantum coherence. For this, we use a strongly coupled cavity to detect a single optical tweezer, allowing for rapid, state-sensitive, high-fidelity, low-atom-loss local measurement with minimal photon scattering of about 100 photons. We benchmark our measurement with a two-atom tweezer array, measuring single atoms sequentially by translating each tweezer trap into the cavity mode, and then detecting light emitted by the cavity that is either fluoresced by the driven atom or transmitted through the driven cavity [Fig. 1(a)]. We observe that an initially prepared hyperfine spin coherence of one atom persists even as the other atom is measured at high fidelity.

Our experimental setup is described in Ref. [26]. Briefly, a bulk optically trapped gas of ultracold ^{87}Rb atoms is prepared near the volume of a horizontal-axis, near-concentric in-vacuum Fabry-Pérot optical cavity with a mirror spacing of 9.4 mm. Atoms are loaded into optical tweezer traps formed by 808-nm-wavelength light that is projected vertically through a high-NA imaging system. An acousto-optical deflector allows us to generate multiple traps in a one-dimensional array and to translate them perpendicularly to the cavity axis. We illuminate the tweezers with counterpropagating light that is detuned about $2\pi \times 35$ MHz below the D_2 $F = 2 \rightarrow F' = 3$ laser-cooling transition, and also with repump light, resonant with the $F = 1 \rightarrow F' = 2$ transition, both at a wavelength of 780 nm. This illumination reduces the population in each tweezer to either zero (empty tweezer) or one atom,

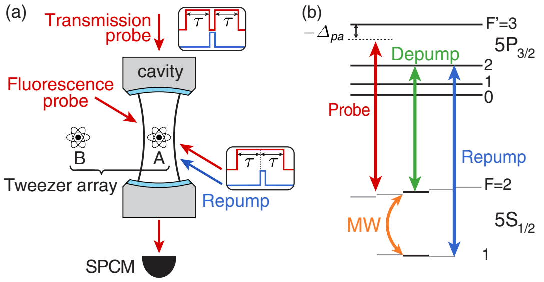

FIG. 1. Experiment schematic. (a) Single atoms are loaded into each of two tweezers that can be translated perpendicularly to the cavity axis for individual readout. Counterpropagating fluorescence probe beams, and also a unidirectional repump beam, are focused on the atom inside the cavity mode. The transmission probe beam couples directly into the cavity. (b) ^{87}Rb level structure. The probe beams (red) are detuned by Δ_{pa} from the $F = 2 \rightarrow F' = 3$ cycling transition. The repump and depump beams (blue and green) are on resonance with the $F = 1 \rightarrow F' = 2$ and $F = 2 \rightarrow F' = 2$ transitions. A resonant microwave (MW) pulse drives the Zeeman-insensitive $|F = 1, m_F = 0\rangle \rightarrow |F = 2, m_F = 0\rangle$ hyperfine transition.

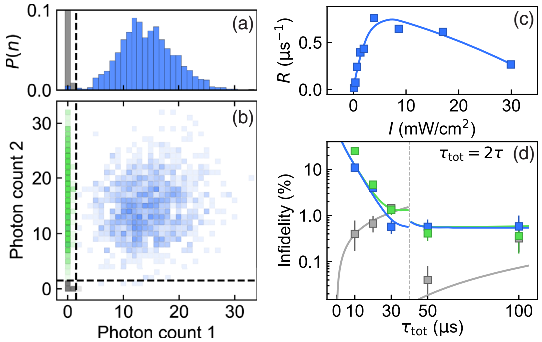

FIG. 2. Fluorescence measurement. A single-probe histogram (a) and two-probe scatter plot (b) show the detected photon counts for tweezers in the no-atom (gray), $F = 2$ atom (blue), or $F = 1$ atom (green) state, taken with $\tau = 25$ μs and $\Delta_{pc} = -2\pi\times$ 10 MHz. The threshold (dashed line) between high and low fluorescence is set between 1 and 2 detected photons. (c) The optimal probe intensity I yields a maximum high count rate of $R = 0.76$ μs^{-1}. Solid line is a guide to the eye. (d) SPAM infidelity is determined for total measurement times $\tau_{\text{tot}} = 2\tau$ from 10 to 100 μs. Solid lines are fits to a model described in Ref. [29]. For $\tau_{\text{tot}} \leq 40$ μs, indicated by the vertical gray line, both the data and model are calculated using a lower detection threshold between 0 and 1 photons.

which we distinguish by imaging the resulting fluorescence through the high-NA objective.

Single tweezer-trapped atoms can serve as long-lived qubits by encoding quantum information in the ground-state hyperfine spin [27,28]. Following this approach, we prepare our atoms into the $F = 1$ or $F = 2$ manifold by applying either depump ($F = 2 \rightarrow F' = 2$) or repump light, respectively [29] [Fig. 1(b)]. Combined with information from the aforementioned fluorescence image, the tweezers are thereby prepared in one of three tweezer states: empty, containing an atom in the $F = 1$ manifold, or containing an atom in the $F = 2$ manifold.

We use our cavity to measure a single tweezer, distinguishing each of these three tweezer states. The cavity reaches the single-atom strong coupling regime, with a cooperativity on the ^{87}Rb D_2 cycling transition of $C = g_0^2/(2\kappa\gamma) = 2.3$ with $\{g_0, \kappa, \gamma\} = 2\pi \times \{2.7, 0.53, 3.0\}$ MHz. Here, g_0 is the maximum atom-photon coupling strength between the $F = 2$ and $F' = 3$ stretched states at a field antinode in the center of the TEM$_{00}$ cavity mode with a beam waist of $w_0 = 20(3)$ μm. The half-linewidths of the cavity and atomic resonances are κ and γ, respectively.

Our high-cooperativity cavity supports two measurement methods. In the fluorescence method, we directly illuminate the atom and collect its fluorescence using the cavity. Strong atom-cavity coupling results in a large collection efficiency into a single optical mode that is detected with little background noise. In the transmission method, we drive the cavity near its resonance and measure the transmission of cavity probe light. Here, atom-cavity hybridization causes a single atom to broaden (at low C) or split (at high C) the cavity resonance line, reducing the transmitted intensity. Single-atom detection using strongly coupled cavities has been demonstrated previously, through both fluorescence [35,36] and cavity transmission or reflection [35,37]. For a two-atom array, collective detection and one-way transport from a cavity into free space has been demonstrated in Ref. [38], while probabilistic atom-photon conversions with single-atom addressability has been shown in Ref. [39]. The present Letter extends these results to high-fidelity single-atom state detection that does not decohere the rest of the array, demonstrating the necessary features of a mid-circuit measurement in a neutral atom quantum information processor.

In both measurement methods, our goal is to realize three-state sensitivity with measurement infidelity at the subpercent level, as required in certain protocols for quantum error correction [9–11]. We do this by probing the atom-cavity system in two consecutive probe intervals. In each interval of duration τ, using probe light near the $F = 2 \rightarrow F' = 3$ transition, we determine whether the cavity contains a single atom in the $F = 2$ manifold. This is done by counting photons emitted from the cavity using a single-photon counting module (SPCM) with a total quantum efficiency of $\eta = 0.25$ [29]. The detection path and SPCM are polarization-insensitive. A positive detection of an $F = 2$ atom is indicated by the observed photon number being either higher [fluorescence; see Fig. 2(a)] or lower [transmission; see Fig. 3(a)] than an optimized threshold. The second probe interval begins with (for fluorescence) or is preceded by (for transmission) a $\tau_{\text{rp}} = 5$ μs pulse of localized repump light

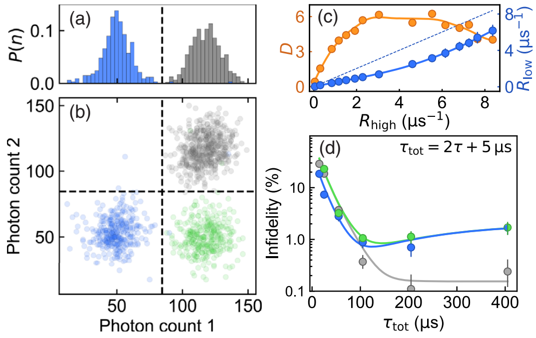

FIG. 3. Transmission measurement. A single-probe histogram (a) and two-probe scatter plot (b) show the detected photon counts for tweezers in the no-atom (gray), $F = 2$ atom (blue), or $F = 1$ atom (green) state, taken with $\tau = 50$ μs and $\Delta_{pc} = 0$. The threshold (dashed line) between high and low transmission is set above 77 detected photons. (c) The transmitted photon count rate with an $F = 2$ atom in the cavity (R_{low}, blue) is lower than the rate (R_{high}, x axis and dotted line) observed without. Ashman's D (orange), a measure of the separation between R_{low} and R_{high}, reaches a maximum owing to atomic saturation. Lines are guides to the eye. (d) SPAM infidelity is determined for each of the initial tweezer states, with total measurement times $\tau_{\mathrm{tot}} = 2\tau + 5$ μs ranging from 15 to 205 μs. The threshold between high and low is selected to minimize infidelity at each τ. Lines are fits to a model described in Ref. [29].

[Fig. 1(a) insets]. The negative detection of an $F = 2$ atom in the first interval followed by a positive detection in the second interval measures the tweezer as having contained an $F = 1$ atom, whereas a negative detection in both intervals measures the tweezer as being empty.

In the cavity fluorescence method, we set the cavity resonance frequency ω_c to be detuned by $\Delta_{ca} = \omega_c - \omega_a = -2\pi \times 10$ MHz below the laser-cooling transition frequency ω_a. We illuminate the atom with vertically counterpropagating probe beams in a lin-perp-lin configuration in order to provide polarization gradient cooling during measurements. The probe frequency ω_p is tuned slightly below the cavity resonance ($\Delta_{pc} = \omega_p - \omega_c \sim -\kappa/2$) to realize cavity cooling of the atomic motion [40]. The probe light intensity is set to maximize the photodetection rate $R = R_{\mathrm{max}}$ of an $F = 2$ tweezed atom in the cavity [Fig. 2(c)]; lower probe intensity drives the atom below saturation, whereas higher probe intensity shifts the incoherent fluorescence spectrum outside the bandwidth of the cavity [41,42]. Experimentally, we find $R_{\mathrm{max}} \simeq 0.76$ $\mu\mathrm{s}^{-1}$, which is below the theoretical maximum of $R_0 = \eta g_0^2/(4\kappa) = 5.4$ $\mu\mathrm{s}^{-1}$ predicted for a two-level atom [29]. This difference may be explained by two effects. First, the tweezer-trapped atom is poorly localized along the cavity axis, exhibiting rms position fluctuations of up to 200 nm with respect to the standing-wave pattern (periodicity of 390 nm) of the cavity mode; see Ref. [26]. The effective square of the atom-cavity coupling strength is thus averaged roughly to $g_{\mathrm{eff}}^2 \simeq g_0^2/2$ owing to spatial random sampling. Second, internal state dynamics induced by the probe light drives the atom between Zeeman sublevels of the ground and excited states, reducing the effective time-averaged coupling to the two polarization modes supported by the cavity. We estimate this effect reduces the maximum cavity emission rate by an additional factor of 0.28 [29].

Fluorescence measurement outcomes, obtained after preparing a single intracavity tweezer in each of the three tweezer states, are shown in Fig. 2. For a probe interval of $\tau = 25$ μs, we observe a large contrast between the photon number detected for a tweezer prepared in the $F = 2$ state and that detected for either the no-atom or $F = 1$ states [Fig. 2(a)]. Combining data from two consecutive 25 μs probe intervals (total measurement time of $\tau_{\mathrm{tot}} = 2\tau = 50$ μs), and setting the threshold for state detection between 1 and 2 photons, we achieve a state preparation and measurement (SPAM) error of several times 10^{-3} for each of the three initial tweezer states (Table I). For shorter τ [Fig. 2(d)], statistical fluctuations in the detected photon number lead us to misidentify bright states as dark states in either the first or second probe intervals, leading to infidelity in $F = 2$ and $F = 1$ state detection, respectively. For longer τ, state preparation error and false detection error caused by the depumping of an $F = 2$ atom before detecting an above-threshold number of photons set a limit on the achievable fidelity. We estimate that these two error sources contribute roughly equally to the overall SPAM error [29]. Table I also reports low atom loss probabilities on the order of 1%, with higher loss rates for atoms in the $F = 2$ manifold due to scattering-induced heating through both probe intervals.

TABLE I. Measurement infidelity and loss probability.

		No atom	$F = 1$	$F = 2$
Fluorescence $2 \times (\tau = 25$ μs$)$	Outcome	Low-low	Low-high	High-X
	Infidelity	0.04(3)%	0.4(2)%	0.6(2)%
	Loss probability		0.2(2)%	1.4(3)%
Transmission $2 \times (\tau = 50$ μs$) + 5$ μs	Outcome	High-high	High-low	Low-X
	Infidelity	0.4(1)%	1.1(2)%	0.9(2)%
	Loss probability		0.7(3)%	1.4(2)%

In the cavity transmission method, we drive the cavity with light that is resonant with both the cavity and the atom ($\Delta_{ca} = \Delta_{pc} = 0$). The circularly polarized probe light, together with a weak magnetic field applied along the cavity axis, pumps $F = 2$ atoms into the spin-stretched state, maximizing their coupling to the cavity. For weak probe light, we observe that an $F = 2$ atom in the cavity reduces the detected transmitted photon rate R_{low} to 0.4 times the rate R_{high} observed with either no atoms or an $F = 1$ atom in the cavity. For low saturation, one would expect $R_{\mathrm{low}}/R_{\mathrm{high}} = (1 + 2C)^{-2}$ for fixed atom-cavity coupling strength. Averaging this expression over a uniform atomic spatial distribution along the cavity axis yields $R_{\mathrm{low}}/R_{\mathrm{high}} = 0.27$ for our system. The difference between the observed and expected transmission reduction may be explained by an inhomogeneous broadening of the atomic resonance of roughly 4 MHz, caused by the ac Stark shift of the tweezer trap light [35]. At high probe intensity, atomic saturation leads to $R_{\mathrm{high}} - R_{\mathrm{low}}$ reaching a constant difference of roughly 2.4 $\mu\mathrm{s}^{-1}$. At an intermediate probe intensity setting of $R_{\mathrm{high}} \simeq 2.2\ \mu\mathrm{s}^{-1}$, the bimodal separation statistic D [43] between the high and low photon count distributions reaches its maximum [Fig. 3(c)].

Transmission measurements made at this optimal probe intensity, with two probe intervals of $\tau = 50\ \mu\mathrm{s}$ each ($\tau_{\mathrm{tot}} = 2\tau + 5\ \mu\mathrm{s} = 105\ \mu\mathrm{s}$), again show clear distinctions among tweezers prepared initially in each of the three tweezer states [Fig. 3(a)]. The detection infidelities and atom loss (Table I) are comparable to those obtained through fluorescence. However, the smaller contrast between high and low detection rates causes the transmission method to be generically slower than the fluorescence method of detection. Transmission measurements with a higher C would be interaction-free [45], thus suppressing depumping errors and mechanical effects from light scattering, which provides particular advantages for detecting trapped particles, such as single molecules [46,47], that lack a cycling optical transition.

Next, we demonstrate that our cavity-enhanced detection of one atom does not perturb the quantum evolution of other atoms in an array, an essential requirement for a mid-circuit measurement. We implement a simple quantum circuit consisting of single-qubit gates, realizing a Ramsey sequence on a two-atom tweezer system [Fig. 4(a)]. We form the array with atom A initially trapped within, and atom B at a variable radial distance d outside, the cavity. Both atoms are initialized in the $|F = 2, m_F = 0\rangle$ state and subject to a $\pi/2$ microwave-induced rotation to the $|F = 1, m_F = 0\rangle$ state [29]. A mid-circuit measurement is performed on atom A, using either detection method with the optimal probe times in Table I. We complete the circuit by applying a second $\pi/2$ pulse with a variable phase offset ϕ, translating atom B into and atom A out of the cavity simultaneously within 200 μs, and performing a cavity measurement of atom B.

Measurements on atom B show a characteristic Ramsey fringe as ϕ is varied [Fig. 4(b)]. We quantify the effect of mid-circuit measurement by considering a normalized contrast, taken as the ratio of the Ramsey-fringe contrasts with and without mid-circuit measurement [48]. We observe a normalized Ramsey contrast above 97% with 84% confidence level [29], when atom B is $d = 34.5\ \mu$m ($d = 46.0\ \mu$m) away from the cavity mode center for fluorescence (transmission) measurement. A mid-circuit fluorescence measurement begins to affect the coherence of atom B once atom B is within about 20 μm of the cavity center [49]. This length scale is consistent with the beam waists of the fluorescence probe beams [29]. A transmission measurement begins to affect atom B at a larger distance of roughly 35 μm from the cavity center, consistent with the beam waist of the cavity mode [26].

Our Letter demonstrates that the integration of cavity-enhanced measurement with a configurable tweezer array enables mid-circuit measurement within a neutral atom quantum information platform. We achieve measurement infidelities comparable to the best previous results in

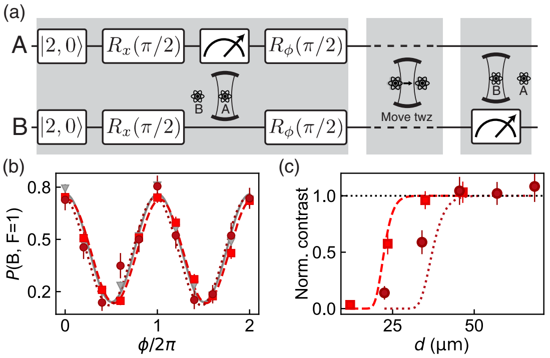

FIG. 4. Mid-circuit measurement. (a) Quantum circuit representing a Ramsey sequence with a mid-circuit measurement of atom A. Atom A (B) is initially located inside (outside) the cavity. Both atoms undergo two $\pi/2$ rotation pulses with variable relative phase ϕ, denoted as $R_x(\pi/2)$ and $R_\phi(\pi/2)$. Atom A is measured between the two pulses using either fluorescence or transmission measurement methods. Both tweezers are repositioned before atom B is measured using the same method. (b) The $F = 1$ state probability of atom B, $P(\mathrm{B}, F = 1)$, shows Ramsey fringes as the phase ϕ of the second pulse is varied. We observe no distinction between Ramsey fringes measured following fluorescence (light red squares, $\tau = 25\ \mu$s) and transmission (dark red circles, $\tau = 50\ \mu$s) detections of atom A, and no detection of atom A (gray). Normalized contrast is defined as the ratio of the Ramsey-fringe contrasts observed with and without a mid-circuit measurement on atom A. (c) Normalized contrast versus the initial distance of atom B from the cavity center, with τ settings as in (b). The dashed (dotted) line is a theoretical estimate based on the intensity and size of the fluorescence probe beam (cavity mode) [29].

atomic tweezer systems [20], in a manner that not only allows subsystem-selective measurement but is also fast, with the measurement time being shorter than not only the second-scale hyperfine-state coherence of tweezer-trapped atoms [51,52], but also the ~100 μs lifetime of the Rydberg states commonly used in Rydberg-tweezer systems [53]. Combined with the low probability of losing a trapped atom during detection, cavity-based measurement could also enable the deterministic preparation of atom arrays assembled atom by atom, without requiring free-space imaging and resorting [12,13,54–56].

The detection time, infidelity, and loss of our measurement could be reduced further by several experimental improvements. Increasing g_0 and κ simultaneously, up until the onset of hyperfine-state mixing [38], would allow for more efficient and faster detection of scattered photons. Better constraints on atomic motion, achieved by improved laser cooling [29] or by stronger confinement along the cavity axis, would mitigate the effective motional reduction of atom-cavity coupling that we presently observe. Speed limits imposed by the need to transport atoms into the cavity prior to measurement could be improved by employing optical-lattice-based conveyors [57]. Transport could be eliminated altogether by maintaining the tweezer array entirely within the cavity volume and using rapid ac Stark shifts realized with local illumination to bring atoms selectively into resonance with the cavity for detection [21]. The atom loss probability could be reduced by using real-time processing and an adaptive measurement that stops each probe interval when a measurement outcome is obtained [58], and also by applying laser cooling briefly after detection.

We thank C. Liu for assistance in the lab and J. Gerber for comments on the manuscript. We acknowledge support from the AFOSR (Grant No. FA9550-19-10328), from ARO through the MURI program (Grant No. W911NF-20-1-0136), from DARPA (Grant No. W911NF2010090), and from the NSF QLCI program through Grant No. OMA-2016245. E. D. acknowledges support from the NSF Graduate Research Fellowship Program. J. H. acknowledges support from the NIH Molecular Biophysics Training Grant (Grant No. 5T32GM008295-31). J. Z. acknowledges support from the BMBF through the program “Quantum technologies–from basic research to market” (Grant No. 13N16265).

---

[*] These authors contributed equally to this work.
[†] dmsk@berkeley.edu

[1] P. W. Shor, Scheme for reducing decoherence in quantum computer memory, Phys. Rev. A **52**, R2493 (1995).
[2] A. M. Steane, Error Correcting Codes in Quantum Theory, Phys. Rev. Lett. **77**, 793 (1996).
[3] R. Raussendorf and H. J. Briegel, A One-Way Quantum Computer, Phys. Rev. Lett. **86**, 5188 (2001).
[4] E. M. Kessler, I. Lovchinsky, A. O. Sushkov, and M. D. Lukin, Quantum Error Correction for Metrology, Phys. Rev. Lett. **112**, 150802 (2014).
[5] W. Dür, M. Skotiniotis, F. Fröwis, and B. Kraus, Improved Quantum Metrology Using Quantum Error Correction, Phys. Rev. Lett. **112**, 080801 (2014).
[6] S. Zhou and L. Jiang, Optimal approximate quantum error correction for quantum metrology, Phys. Rev. Res. **2**, 013235 (2020).
[7] Y. Li, X. Chen, and M. P. A. Fisher, Quantum Zeno effect and the many-body entanglement transition, Phys. Rev. B **98**, 205136 (2018).
[8] B. Skinner, J. Ruhman, and A. Nahum, Measurement-Induced Phase Transitions in the Dynamics of Entanglement, Phys. Rev. X **9**, 031009 (2019).
[9] E. Dennis, A. Kitaev, A. Landahl, and J. Preskill, Topological quantum memory, J. Math. Phys. (N.Y.) **43**, 4452 (2002).
[10] R. Raussendorf and J. Harrington, Fault-Tolerant Quantum Computation with High Threshold in Two Dimensions, Phys. Rev. Lett. **98**, 190504 (2007).
[11] A. G. Fowler, M. Mariantoni, J. M. Martinis, and A. N. Cleland, Surface codes: Towards practical large-scale quantum computation, Phys. Rev. A **86**, 032324 (2012).
[12] D. Barredo, S. D. Léséleuc, V. Lienhard, T. Lahaye, and A. Browaeys, An atom-by-atom assembler of defect-free arbitrary two-dimensional atomic arrays, Science **354**, 1021 (2016).
[13] M. Endres, H. Bernien, A. Keesling, H. Levine, E. R. Anschuetz, A. Krajenbrink, C. Senko, V. Vuletić, M. Greiner, and M. D. Lukin, Atom-by-atom assembly of defect-free one-dimensional cold atom arrays, Science **354**, 1024 (2016).
[14] Y. Wang, X. Zhang, T. A. Corcovilos, A. Kumar, and D. S. Weiss, Coherent Addressing of Individual Neutral Atoms in a 3D Optical Lattice, Phys. Rev. Lett. **115**, 043003 (2015).
[15] C. Gross and I. Bloch, Quantum simulations with ultracold atoms in optical lattices, Science **357**, 995 (2017).
[16] C. D. Bruzewicz, J. Chiaverini, R. McConnell, and J. M. Sage, Trapped-ion quantum computing: Progress and challenges, Appl. Phys. Rev. **6**, 021314 (2019).
[17] A. Fuhrmanek, R. Bourgain, Y. R. P. Sortais, and A. Browaeys, Free-Space Lossless State Detection of a Single Trapped Atom, Phys. Rev. Lett. **106**, 133003 (2011).
[18] M. Kwon, M. F. Ebert, T. G. Walker, and M. Saffman, Parallel Low-Loss Measurement of Multiple Atomic Qubits, Phys. Rev. Lett. **119**, 180504 (2017).
[19] M. Martinez-Dorantes, W. Alt, J. Gallego, S. Ghosh, L. Ratschbacher, Y. Völzke, and D. Meschede, Fast Nondestructive Parallel Readout of Neutral Atom Registers in Optical Potentials, Phys. Rev. Lett. **119**, 180503 (2017).
[20] J. P. Covey, I. S. Madjarov, A. Cooper, and M. Endres, 2000-Times Repeated Imaging of Strontium Atoms in Clock-Magic Tweezer Arrays, Phys. Rev. Lett. **122**, 173201 (2019).
[21] A. Urech, I. H. A. Knottnerus, R. J. C. Spreeuw, and F. Schreck, Narrow-line imaging of single strontium atoms in shallow optical tweezers, Phys. Rev. Res. **4**, 023245 (2022).

[22] C. Gross and W. S. Bakr, Quantum gas microscopy for single atom and spin detection, Nat. Phys. **17**, 1316 (2021).

[23] We note recent efforts that achieve fast free-space detection of tweezer-trapped neutral atoms through careful engineering of fluorescence detection [24] and Rydberg-ensemble-assisted imaging [25].

[24] A. Bergschneider, V. M. Klinkhamer, J. H. Becher, R. Klemt, G. Zürn, P. M. Preiss, and S. Jochim, Spin-resolved single-atom imaging of ^{6}Li in free space, Phys. Rev. A **97**, 063613 (2018).

[25] W. Xu, A. V. Venkatramani, S. H. Cantú, T. Šumarac, V. Klüsener, M. D. Lukin, and V. Vuletić, Fast Preparation and Detection of a Rydberg Qubit Using Atomic Ensembles, Phys. Rev. Lett. **127**, 050501 (2021).

[26] E. Deist, J. A. Gerber, Y.-H. Lu, J. Zeiher, and D. M. Stamper-Kurn, Superresolution Microscopy of Optical Fields Using Tweezer-Trapped Single Atoms, Phys. Rev. Lett. **128**, 083201 (2022).

[27] T. Xia, M. Lichtman, K. Maller, A. W. Carr, M. J. Piotrowicz, L. Isenhower, and M. Saffman, Randomized Benchmarking of Single-Qubit Gates in a 2D Array of Neutral-Atom Qubits, Phys. Rev. Lett. **114**, 100503 (2015).

[28] H. Levine, A. Keesling, G. Semeghini, A. Omran, T. T. Wang, S. Ebadi, H. Bernien, M. Greiner, V. Vuletić, H. Pichler, and M. D. Lukin, Parallel Implementation of High-Fidelity Multiqubit Gates with Neutral Atoms, Phys. Rev. Lett. **123**, 170503 (2019).

[29] See Supplemental Material at http://link.aps.org/supplemental/10.1103/PhysRevLett.129.203602 for details on experimental methods and data analysis, which includes Refs. [30–34].

[30] N. Schlosser, G. Reymond, I. Protsenko, and P. Grangier, Sub-poissonian loading of single atoms in a microscopic dipole trap, Nature (London) **411**, 1024 (2001).

[31] C. Tuchendler, A. M. Lance, A. Browaeys, Y. R. P. Sortais, and P. Grangier, Energy distribution and cooling of a single atom in an optical tweezer, Phys. Rev. A **78**, 033425 (2008).

[32] A. M. Kaufman, B. J. Lester, and C. A. Regal, Cooling a Single Atom in an Optical Tweezer to Its Quantum Ground State, Phys. Rev. X **2**, 041014 (2012).

[33] J. A. Gerber, Cavity quantum electrodynamics with a locally addressable quantum gas, Ph.D. thesis, University of California Berkeley, 2020.

[34] J. R. Johansson, P. D. Nation, and F. Nori, QuTiP2: A PYTHON framework for the dynamics of open quantum systems, Comput. Phys. Commun. **184**, 1234 (2013).

[35] J. Bochmann, M. Mücke, C. Guhl, S. Ritter, G. Rempe, and D. L. Moehring, Lossless State Detection of Single Neutral Atoms, Phys. Rev. Lett. **104**, 203601 (2010).

[36] J. Gallego, W. Alt, T. Macha, M. Martinez-Dorantes, D. Pandey, and D. Meschede, Strong Purcell Effect on a Neutral Atom Trapped in an Open Fiber Cavity, Phys. Rev. Lett. **121**, 173603 (2018).

[37] R. Gehr, J. Volz, G. Dubois, T. Steinmetz, Y. Colombe, B. L. Lev, R. Long, J. Estève, and J. Reichel, Cavity-Based Single Atom Preparation and High-Fidelity Hyperfine State Readout, Phys. Rev. Lett. **104**, 203602 (2010).

[38] T. Dordevic, P. Samutpraphoot, P. L. Ocola, H. Bernien, B. Grinkemeyer, I. Dimitrova, V. Vuletić, and M. D. Lukin, Entanglement transport and a nanophotonic interface for atoms in optical tweezers, Science **373**, 1511 (2021).

[39] S. Langenfeld, O. Morin, M. Körber, and G. Rempe, A network-ready random-access qubits memory, npj Quantum Inf. **6**, 86 (2020).

[40] S. Nuszmann, K. Murr, M. Hijlkema, B. Weber, A. Kuhn, and G. Rempe, Vacuum-stimulated cooling of single atoms in three dimensions, Nat. Phys. **1**, 122 (2005).

[41] B. R. Mollow, Power spectrum of light scattered by two-level systems, Phys. Rev. **188**, 1969 (1969).

[42] H. J. Kimble and L. Mandel, Theory of resonance fluorescence, Phys. Rev. A **13**, 2123 (1976).

[43] Given two distributions with means $\mu_{1,2}$ and standard deviations $\sigma_{1,2}$, Ashman's D statistic for bimodal separation is defined as $D = |\mu_1 - \mu_2|/\sqrt{(\sigma_1^2 + \sigma_2^2)/2}$; see Ref. [44].

[44] K. A. Ashman, C. M. Bird, and S. E. Zepf, Detecting bimodality in astronomical datasets, Astron. J. **108**, 2348 (1994).

[45] P. Kwiat, H. Weinfurter, T. Herzog, A. Zeilinger, and M. A. Kasevich, Interaction-Free Measurement, Phys. Rev. Lett. **74**, 4763 (1995).

[46] L. Anderegg, L. W. Cheuk, Y. Bao, S. Burchesky, W. Ketterle, K.-K. Ni, and J. M. Doyle, An optical tweezer array of ultracold molecules, Science **365**, 1156 (2019).

[47] J. T. Zhang, L. R. B. Picard, W. B. Cairncross, K. Wang, Y. Yu, F. Fang, and K.-K. Ni, An optical tweezer array of ground-state polar molecules, Quantum Sci. Technol. **7**, 035006 (2022).

[48] The limited fringe contrast of about 0.6 observed in our setup even without mid-circuit detection arises from imperfect preparation in the $m_F = 0$ magnetic sublevel and ac Stark shifts of the microwave frequency by tweezer light.

[49] Reference [50] demonstrates fast local detection in a trapped ion platform, with low measurement-induced decoherence for ions with separations of hundreds of micrometers.

[50] S. Crain, C. Cahall, G. Vrijsen, E. E. Wollman, M. D. Shaw, V. B. Verma, S. W. Nam, and J. Kim, High-speed low-crosstalk detection of a 171Yb+ qubit using superconducting nanowire single photon detectors, Commun. Phys. **2**, 97 (2019).

[51] D. Bluvstein, H. Levine, G. Semeghini, T. T. Wang, S. Ebadi, M. Kalinowski, A. Keesling, N. Maskara, H. Pichler, M. Greiner, V. Vuletić, and M. D. Lukin, A quantum processor based on coherent transport of entangled atom arrays, Nature (London) **604**, 451 (2022).

[52] M. A. Norcia, A. W. Young, W. J. Eckner, E. Oelker, J. Ye, and A. M. Kaufman, Seconds-scale coherence on an optical clock transition in a tweezer array, Science **366**, 93 (2019).

[53] I. I. Beterov, I. I. Ryabtsev, D. B. Tretyakov, and V. M. Entin, Quasiclassical calculations of blackbody-radiation-induced depopulation rates and effective lifetimes of Rydberg nS, nP, and nD alkali-metal atoms with $n \leq 80$, Phys. Rev. A **79**, 052504 (2009).

[54] Y. Miroshnychenko, W. Alt, I. Dotsenko, L. Förster, M. Khudaverdyan, D. Meschede, D. Schrader, and A. Rauschenbeutel, An atom-sorting machine, Nature (London) **442**, 151 (2006).

[55] K. M. Fortier, S. Y. Kim, M. J. Gibbons, P. Ahmadi, and M. S. Chapman, Deterministic Loading of Individual Atoms

to a High-Finesse Optical Cavity, Phys. Rev. Lett. **98**, 233601 (2007).

[56] H. Kim, W. Lee, H.-g. Lee, H. Jo, Y. Song, and J. Ahn, *In situ* single-atom array synthesis using dynamic holographic optical tweezers, Nat. Commun. **7**, 13317 (2016).

[57] S. Kuhr, W. Alt, D. Schrader, M. Müller, V. Gomer, and D. Meschede, Deterministic delivery of a single atom, Science **293**, 278 (2001).

[58] M. N. H. Chow, B. J. Little, and Y.-Y. Jau, High-fidelity, low-loss state detection of alkali-metal atoms in optical tweezer traps, arXiv:2206.00144.

Appendix C

QuTiP simulation code

This appendix includes the basic simulation code, written in a Jupyter notebook using the Python package QuTiP [155], that I used to simulate cavity measurement and resonance fluorescence outside of the low-saturation regime; see Sections 6.1.2 and 6.3.5. I hope these serve as a helpful launching point for a future student.

[1]:

```
import numpy as np
import matplotlib.pyplot as plt
import qutip as qt
```

[2]:

```
### Fluorescence measurement:
g = 1
kappa = 1.2
Gamma = 6.07
OmegaA = 1
OmegaC = 0
DeltaPA = -10 # fixed for fluorescence measurement

# vary DeltaPC (by tuning the cavity frequency)
DeltaPC_range = np.arange(-3*kappa,3*kappa,0.05)

# define max N for photon Fock basis
N = 5

sm = qt.tensor(qt.destroy(2),qt.identity(N)) # atomic lowering operator
a = qt.tensor(qt.identity(2),qt.destroy(N)) # cavity annihilation operator

Pe_list = []
nbar_list = []

for DeltaPC in DeltaPC_range:

    # define the Hamiltonian
    H = - DeltaPA*sm.dag()*sm \
        - DeltaPC*a.dag()*a \
        + np.conj(g)*sm*a.dag() + g*sm.dag()*a \
        + np.conj(OmegaA)*sm + OmegaA*sm.dag()

        # collapse operators:
    c_ops = [np.sqrt(Gamma)*sm,np.sqrt(kappa)*a]

    final_state = qt.steadystate(H, c_ops)

    nbar = qt.expect(a.dag() * a, final_state)
    nbar_list.append(nbar)
    Pe = qt.expect(sm.dag() * sm, final_state)
    Pe_list.append(Pe)

cav_scattering_rate = np.array(nbar_list)*kappa
fs_scattering_rate = np.array(Pe_list)*Gamma
```

```
plt.plot(DeltaPC_range,cav_scattering_rate,label='cavity')
plt.plot(DeltaPC_range,fs_scattering_rate,label='free space')
plt.legend()
plt.xlabel(r'$\Delta_{pc}$');
plt.ylabel('Scattering rate');
```

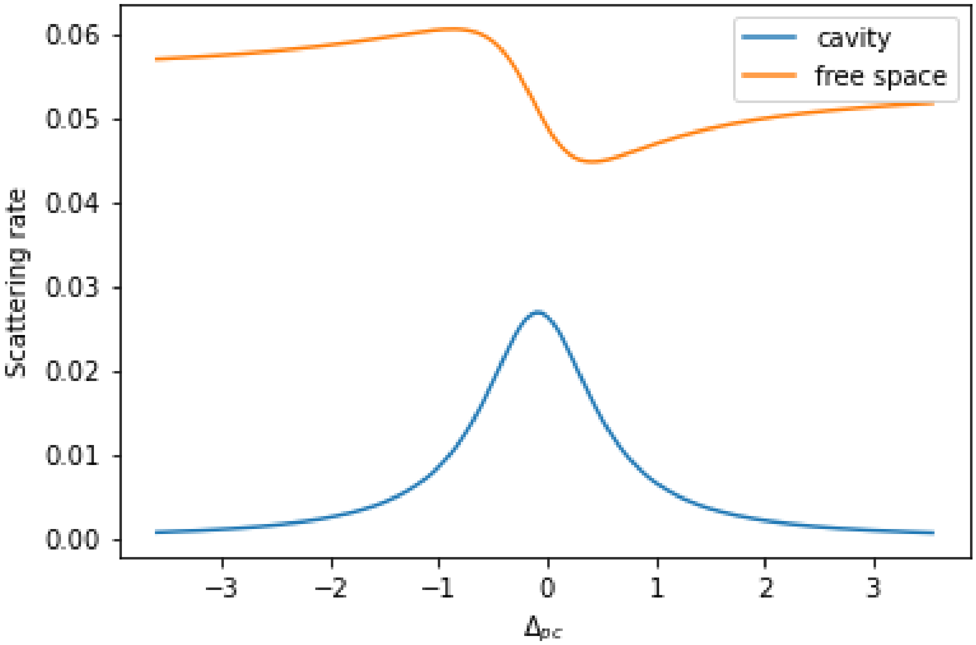

[3]:

```
### Transmission measurement:
OmegaA = 0
OmegaC = 0.1
DeltaCA = 0 # fixed for fluorescence measurement
# vary DeltaPC (by tuning the probe frequency)
DeltaPC_range = np.arange(-3*kappa,3*kappa,0.05)

# define max N for photon Fock basis - make sure this is large enough!
N = 5
sm = qt.tensor(qt.destroy(2),qt.identity(N)) # atomic lowering operator
a = qt.tensor(qt.identity(2),qt.destroy(N)) # cavity annihilation operator

nbar_list = []
nbar_empty_list = []
for DeltaPC in DeltaPC_range:
    DeltaPA = DeltaCA + DeltaPC
    # define the Hamiltonian
```

```
    H = - DeltaPA*sm.dag()*sm \
        - DeltaPC*a.dag()*a \
        + np.conj(g)*sm*a.dag() + g*sm.dag()*a \
        + np.conj(OmegaC)*a + OmegaC*a.dag()
    c_ops = [np.sqrt(Gamma)*sm,np.sqrt(kappa)*a]
    final_state = qt.steadystate(H, c_ops)
    nbar = qt.expect(a.dag() * a, final_state)
    nbar_list.append(nbar)

    # define the empty cavity Hamiltonian (g=0) for comparison
    H_empty = - DeltaPA*sm.dag()*sm \
        - DeltaPC*a.dag()*a \
        + np.conj(OmegaC)*a + OmegaC*a.dag()
    final_state = qt.steadystate(H_empty, c_ops)
    nbar_empty = qt.expect(a.dag() * a, final_state)
    nbar_empty_list.append(nbar_empty)

cav_scattering_rate = np.array(nbar_list)*kappa
emptycav_scattering_rate = np.array(nbar_empty_list)*kappa

plt.plot(DeltaPC_range,cav_scattering_rate,label='with atom')
plt.plot(DeltaPC_range,emptycav_scattering_rate,label='empty cavity')
plt.legend()
plt.xlabel(r'$\Delta_{pc}$');
plt.ylabel('Cavity transmission');
```

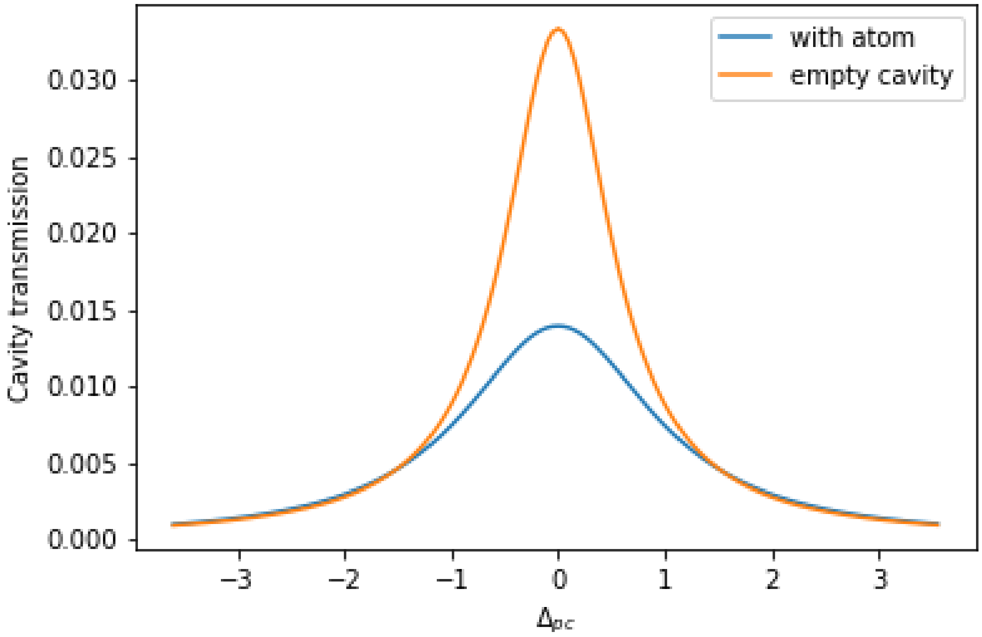

[4]:

```
### Resonance fluorescence spectrum (Mollow triplet; no cavity)

OmegaA = 7
DeltaPA = 0


sm = qt.tensor(qt.destroy(2)) # atomic lowering operator

# define the Hamiltonian
H = - DeltaPA*sm.dag()*sm \
    + np.conj(OmegaA)*sm + OmegaA*sm.dag()

c_ops = [np.sqrt(Gamma)*sm]

final_state = qt.steadystate(H, c_ops)

w_list = np.linspace(-3.*OmegaA, 3*OmegaA, 2000)
spec = qt.spectrum(H, w_list, c_ops, sm.dag(), sm)

plt.plot(w_list, np.abs(spec)**2)
plt.xlabel('Detuning')
plt.ylabel('Atomic fluorescence spectrum');
```